DISSERTATION

COHERENT VIBRATIONAL DYNAMICS IN ETHYLENE CARBONATE: INSIGHTS FROM 2D INFRARED SPECTROSCOPY

Submitted by

Luke Robert Guerrieri

Department of Chemistry

In partial fulfillment of the requirements

For the Degree of Doctor of Philosophy

Colorado State University

Fort Collins, Colorado

Spring 2025

Doctoral Committee:

Advisor: Amber T. Krummel

Nancy Levinger
Jesse Wilson
Chuck Henry

ABSTRACT

COHERENT VIBRATIONAL DYNAMICS IN ETHYLENE CARBONATE: INSIGHTS FROM 2D INFRARED SPECTROSCOPY

The research presented in this dissertation explores the mechanisms of coherent vibrational relaxation in the cyclic carbonate ester, ethylene carbonate (EC). Coherent relaxation processes describe the redistribution of quantum superposition states, but relatively little is known about the molecular properties governing these processes for vibrational superpositions in chemical systems. EC, a highly coupled vibrational system with applications in organic battery electrolyte mixtures, serves as a model compound for studying coherent vibrational dynamics. The fundamental carbonyl stretch of EC couples to doubly excited states via Fermi resonance. An investigation of the carbonyl fundamental stretch using linear Fourier transform infrared spectroscopy (FTIR) and two-dimensional infrared spectroscopy (2DIR) reveals coherent relaxation mechanisms involving multiple vibrational degrees of freedom. Pump selective 2DIR experiments compare the relative intensities of coherent relaxation processes to different features in the 2DIR spectrum, finding a correlation between the spectral amplitude of coherent relaxation processes and Fermi resonance coupling strength. A follow up investigation uses ^{13}C isotopic substitution to modify the Fermi resonance coupling strength in EC isotopologues. It is found that ^{13}C substitution strengthens the Fermi resonance coupling in EC isotopologues; however, isotopic substitution is found to suppress the redistribution of quantum superpositions involving Fermi coupled vibrations. Analysis of vibrational

lifetimes for the Fermi coupled states indicates that the relative strengths of coherent relaxation processes correlate with the strength of vibrational coupling to a manifold of experimental dark states. Those results suggest that coherent relaxation in EC is primarily driven by the delocalization of vibrational relaxation pathways, rather than the strength of direct coupling between Fermi coupled modes.

ACKNOWLEDGEMENTS

Here I would like to express my gratitude to the following people, whose support made my completion of this work possible. To my advisor, Dr. Amber Krummel, I could not have done this without your guidance, patience, trust, and support. I will forever be grateful to you for giving me the freedom and encouragement to pursue research that captivates me. Clara and Yusef, thank you for helping me find my footing during the turbulence of the early years. I couldn't have asked for better role models. To my best friend, Sarah, big thanks. To my father, John, a wiseman once said, "it's dangerous business going out your front door. You step onto the road, and if you don't keep your feet, there's no knowing where you might be swept off to." Those drives to Savanna were the dangerous business that brought me here. Thank you for fostering my curiosity towards the world. To my sister, Amy, when I followed you to Colorado, I didn't know what was ahead of me, only that you'd have my back. Thank you for the food, shelter, love, and support. Nonna Donna, thank you for praying for me. Like many aspects of this journey, I still can't believe it worked. Randy, thanks for teaching me that life doesn't have to suck. I plan to believe you again soon. To Dr. Mark Masthay, I owe this accomplishment to many fantastic educators who encouraged and guided me throughout my pre-graduate career, but none more than you. You reminded me, about a year ago, that there is a life after grad school. If mine benefits even a fraction of the people that yours has, it will have been well spent.

TABLE OF CONTENTS

Chapter 1
Introduction

1.1 Motivation

The motivation for the work presented in this dissertation lies in understanding the molecular properties that influence the dynamics of coherent vibrational relaxation in chemical systems. Vibrational relaxation describes how excess thermal energy stored in the motions of chemical bonds redistributes within molecular systems and dissipates into the environment, returning the molecule to thermal equilibrium. This process plays an important role in many chemical and biological processes, such as energy flow in photosynthetic pigments,[1–3] chemical reactivity,[4–6] and the thermal properties of nanoscale materials.[7,8] The efficiency of energy distribution within a system can dictate its function, making understanding the molecular physics that dictates vibrational relaxation a matter of practical importance for modifying function at the molecular level.

Broadly, mechanisms of vibrational relaxation can be split into incoherent and coherent relaxation pathways. Incoherent pathways describe the dissipation of energy localized in well-defined vibrational modes, also referred to as population states, due to random interactions with the environment. For chemical species in solution, these interactions reflect processes such as collisions between neighboring molecules. Incoherent relaxation can be thought of in the context of a Plinko game, where an initially excited vibrational state is “dropped” into an environment represented by the Plinko board. Random interactions with the environment cause the vibrational state to dissipate energy and change its course. The cumulative effects of environmental interactions

ultimately determine the final state of the molecule, reflecting a random dissipative process. Conversely, coherent pathways involve vibrational energy that is delocalized in quantum mechanical mixtures of molecular vibrations, also known as a superposition or coherence state. The wavelike nature of these processes enables efficient and directed relaxation. [6,9–11] In the Plinko analogy, a coherent pathway is akin to pouring a liquid into the board. The delocalized energy follows an efficient path to lower energy states, flowing smoothly around obstacles in a consistent pathway. A better understanding of how molecular structure and environmental interactions can promote either coherent or incoherent relaxation pathways potentially offers new methods to control thermal energy flow at the molecular level, opening new possibilities in applications ranging from tuning chemical reactivity to designing more efficient devices for energy storage and conversion.

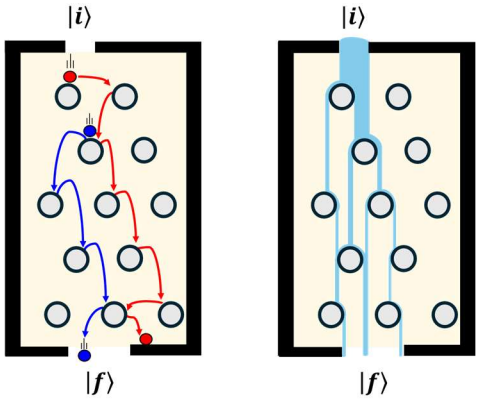

Figure 1-1: Comparing incoherent and coherent vibrational relaxation using the Plinko analogy. **Left.** Incoherent relaxation pathway where balls are dropped into the board from initial state $|i\rangle$. Red and blue colors represent two trajectories for the stochastic relaxation process. Only the blue trajectory transfers energy to state $|f\rangle$ before dissipating into the bath. **Right.** Coherent relaxation pathway represented by the flow of a liquid through the board. The structure of the board dictates how the delocalized state propagates from $|i\rangle$ to $|f\rangle$.

Studying coherent vibrational relaxation presents both theoretical and experimental challenges. Theoretically, accurately modeling vibrational relaxation in condensed-phase systems requires accounting for quantum mechanical interactions between many atoms, making such calculations computationally expensive and often impractical.[12–14] As a result, classical approximations[6,12,15,16] are often employed, but their validity in capturing coherence effects in experimental data remains uncertain.[17,18] The absence of a convenient and comprehensive theoretical framework for describing coherent vibrational relaxation complicates the interpretation of experimental data, as the relationship between experimental observables and underlying molecular properties is not always well defined.[18] This creates a circular problem in which limited theoretical understanding hinders the interpretation of experiments, while uncertainty in experimental interpretation provides limited guidance for improving theoretical models. Further, coherence states are inherently short lived,[11,19] as interactions with the molecular surroundings disrupt the phase relationships between the elements of a coherent superposition, leading to dephasing. Extracting meaningful information from experimental observables requires techniques capable of distinguishing between coherent and incoherent relaxation pathways with a high degree of temporal resolution. However, the analysis of coherence effects in complex molecular systems remains challenging without a reliable theoretical framework to link experimental observables to the physical properties of molecular systems.

Addressing these challenges requires an effort to refine both theoretical and experimental approaches. The work presented in this dissertation aims to contribute on the experimental side by leveraging coherent infrared spectroscopy to characterize how

factors such as interactions between vibrational excited states shape the coherent or incoherent nature of vibrational relaxation in chemical systems.

1.2. Overview of Coherent Infrared Spectroscopy

The primary experimental techniques utilized in this dissertation belong to the class of coherent infrared (IR) spectroscopies. In its simplest definition, spectroscopy is the study of interactions between light and matter. Coherent IR spectroscopies specifically probe the change in well-defined patterns of nuclear motion along chemical bonds (vibrational modes) due to perturbations by a coherent IR light source. The nature of the IR light-matter interactions thus reports on the properties of chemical bonds themselves, offering insights into chemical structures on molecular length scales. IR spectroscopy experiments which modify properties of the IR chromophore, the solvent environment, or the coherent IR light source can be used to investigate how vibrational relaxation processes respond to changes in the properties of molecular systems or their surroundings.

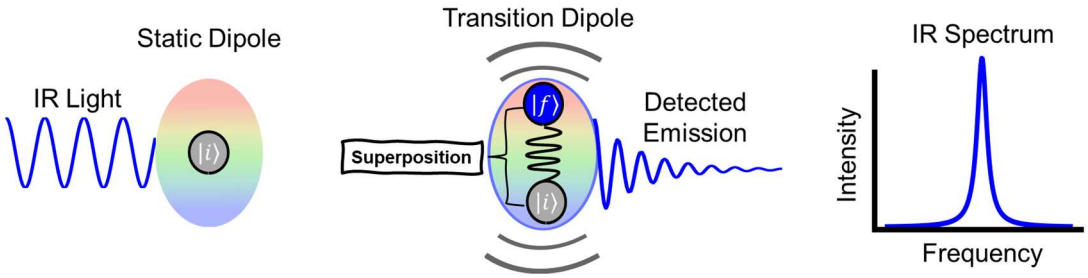

Figure 1.2-1: Operating principles of IR spectroscopy: **Left.** A molecule residing in an initial state before perturbation by IR light. **Middle.** Perturbation by resonant light generates a vibrational superposition between two states. The superposition state corresponds to coherent oscillations in the molecular dipole which emit radiation. **Right.** An IR spectrum gives the frequency domain representation of the emitted signal.

Infrared spectroscopy provides a potent set of experimental tools for studying molecular vibrations in condensed phase systems. The basic operating principle of IR spectroscopy involves using coherent IR light to perturb the intrinsic dipole moment of a molecular species, which arises from the spatial distribution of charges within a molecule. A cartoon depiction of a perturbation by IR light is given in figure 1.2-1. The left side of figure 1.2-1 depicts a molecule residing in an initial vibrational population state $|i\rangle$, before perturbation by a coherent IR light source. If energy of the incident IR light source matches the energy difference between two vibrational states in the molecule, the perturbation induces a transition from the initially occupied state $|i\rangle$ to the final state $|f\rangle$, forming a coherent superposition of $|i\rangle$ and $|f\rangle$. This coherent superposition is represented by a spring connecting states $|i\rangle$ and $|f\rangle$ in the middle section of figure 1.2-1. The generation of a vibrational superposition coincides with coherent oscillations in the molecular dipole moment. The oscillations of the dipole moment emit radiation at a frequency corresponding to the energy difference of states $|i\rangle$ and $|f\rangle$.

The record of the emitted radiation, represented in the frequency domain as a spectrum, provides a map of the vibrational energy levels of the system and the amplitude of the emitted signal at each frequency. On the right side of figure 1.2-1, the single peak appears on the frequency axis at the energy gap between states $|i\rangle$ and $|f\rangle$. The intensity of peaks in an IR spectrum reports on the probability of the incident radiation promoting the transition from $|i\rangle$ to $|f\rangle$ and is described by the transition dipole moment μ_{if}. The widths of peaks in an IR spectrum directly report on the coherence lifetimes of the emitted signal, offering insights into the stability of coherence states.

The inherent generation of vibrational superpositions in coherent IR experiments highlights their utility in studying coherent dynamics. Factors such as the intensities and frequency positions of peaks in an IR spectrum can additionally provide information on the interactions between different vibrational states, indicating the presence of relaxation pathways. This will be described in the next section in the context of linear IR absorption spectroscopy. Further, temporally separating the generation of an initial coherence state and detection of the emitted signal using time-dependent spectroscopies offers a means of studying the time evolution of coherent superpositions and the flow of vibrational energy.

1.2.1 Identifying Relaxation Pathways with Linear Absorption Spectroscopy

Infrared (IR) spectroscopy serves as a valuable tool for studying vibrational relaxation by identifying couplings between energetically similar vibrational states. When two vibrational modes share common patterns of nuclear motion, they can exchange energy at faster rates than those predicted by incoherent hopping mechanisms, through

a phenomenon known as resonance coupling. Resonance coupling can be thought of analogously to a child on a swing. If the child kicks their legs in synch with the arc of the swing, energy is efficiently transferred into the motion of the swing. Similarly, vibrational modes that involve overlapping nuclear motion can transfer energy between one another. Such resonance couplings are thought to play an important role in both the speed and directionality of vibrational relaxation. [20,21]

Experimentally, resonance coupling alters both the frequency positions and relative intensities of peaks in an IR spectrum, [22–24] making it possible to study vibrational coupling with IR spectroscopy. A special case of resonance coupling arises when an IR allowed transition, in which the light-matter interaction changes the vibrational energy level by a single quantum, couples to an IR forbidden two-quanta transition. This phenomenon, known as a Fermi resonance, [25] results in intensity redistribution and the appearance of a Fermi doublet in IR spectra. In the absence of coupling, the two quanta transition carries no transition dipole moment; however, resonance coupling redistributes intensity into the forbidden transition, making it experimentally observable. The relative intensities of peaks in a Fermi doublet directly relate to the strength of interaction between the coupled vibrational modes, [25–28] making it possible to estimate relaxation rates by comparing peak intensities in experimental spectra. As an example, linear absorption spectra for the Fermi coupled carbonyl fundamental (allowed) and ring overtone (forbidden) modes of ethylene carbonate (EC) and its triply ^{13}C substituted isotopologue are given in figure 1.2.1-1.

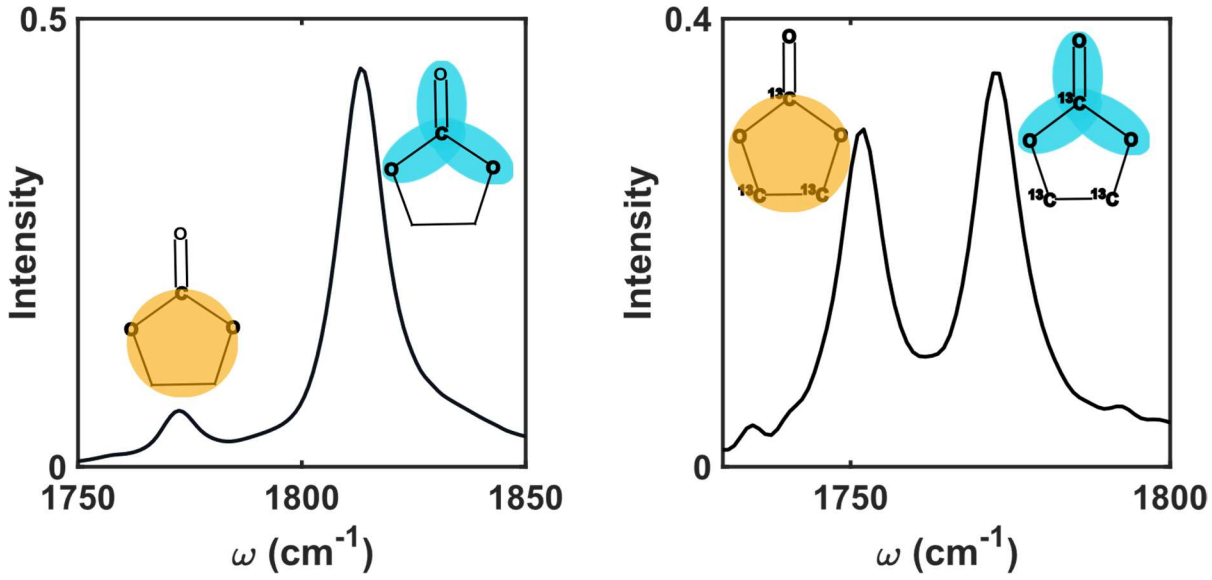

Figure 1.2.1-1: Linear IR spectra of the Fermi doublet in the carbonyl stretching region of EC (left) and its triply ^{13}C substituted isotopologue (right). Bond line drawings of the molecules are positioned next to each peak, with the highlighted region indicating the peak corresponds to transitions involving vibrations in the carbonyl (blue) or ring (orange) moeities.

The two largest peaks in each of the spectra above correspond to the Fermi coupled transitions. The more intense peak corresponds to a superposition involving the excited state $|C\rangle$ and the vibrational ground state. The motion of the atomic nuclei for $|C\rangle$ primarily appears in the carbon-oxygen bonds,[29,30] highlighted in blue. A superposition of the ground state and the second excited state of mode $|R\rangle$ gives rise to the less intense peak. The nuclear displacement of $|R\rangle$ mostly resides in the orange highlighted ring. In the absence of coupling, the transition dipole moment of the $|0\rangle \rightarrow |R\rangle$ transition would be zero. The presence of resonance coupling redistributes the intensity of the $|0\rangle \rightarrow |C\rangle$ transition, making the $|0\rangle \rightarrow |R\rangle$ transition visible in spectrum. The experimentally observed intensity of the ring transition reports on the strength of the resonance coupling. From figure 1.2.1-1, we see that the intensity of the ring transition is greater in the isotopic

compound. As such, we can expect stronger coupling and faster direct relaxation from $|C\rangle$ to $|R\rangle$ in the ^{13}C substituted isotopologue of EC.

However, vibrational relaxation rates between modes often depend on more than just the strength of resonance coupling. Indirect relaxation pathways can involve intermediate states, such as internal vibrational degrees of freedom in the molecule or vibrational modes in nearby solvent molecules. [21,31–35] Linear IR spectroscopies alone cannot predict whether these indirect pathways play a significant role in the relaxation between resonantly coupled states. Addressing this limitation requires time-resolved multidimensional spectroscopic techniques, which independently label the excitations of different vibrational modes as well as monitor their evolution over time. Such techniques enable the direct observation of relaxation, making it possible to disentangle complex relaxation mechanisms.

1.2.2 Two-Dimensional Infrared Spectroscopy

Two-dimensional infrared spectroscopy (2DIR) is a multi-dimensional and time-resolved experimental technique capable of reporting on both coherent and incoherent mechanisms of vibrational relaxation. While a more detailed description of 2DIR is given in chapter 2, this section offers a brief overview of the technique. A generic 2DIR pulse sequence is given on the left side of figure 1.2.2-1. In this picture, a molecular sample resting in the vibrational ground state is perturbed by three mid-IR pulses. The first pulse that interacts with the sample, E_1, generates a coherent superposition of the ground state and the first excited state of a vibrational mode. By scanning the time delay between E_1 and E_2, the oscillations of the coherence become recorded in the 2DIR signal. In the

frequency domain, this coherence labels the molecular response on the ω_1 excitation axis (right side of figure 1.2.2-1). The second pulse serves to destructively interfere with the coherence generated by E_1, placing the molecule in an excited state population that evolves incoherently over the population time, t_2. Tracking the evolution of 2DIR peak amplitudes enables 2DIR to report on incoherent population dynamics. Alternatively, the second pulse can generate a multi-level coherence between two excited states, a phenomenon knowns as quantum beating,[36,37] allowing the t_2 interval to additionally report on the dynamics of multi-level coherence states. The third pulse, E_3, again generates a coherent superposition that emits radiation contributing to the 2DIR signal pulse, E_{sig}. The frequency domain representation of the final coherence dictates the frequency position of the 2DIR signal on the ω_3 detection axis. As such, a single 2DIR spectrum can be thought of as a 3D map, in which the coherences generated by the first (ω_1) and third (ω_3) IR pulses serve to label the initial and final states of a relaxation pathway. The waiting time, t_2, represents the third dimension, over which population or multi-level coherence relaxation occurs. Note that in figure 1.2.2-1 two peaks are shown. The first peak, plotted in blue, represents a molecular response in which the third pulse generates a coherence involving the ground vibrational state. The second peak, plotted in red, corresponds to an excited state absorption process whose ω_3 frequency position is shifted by the vibrational anharmonicity of the mode.

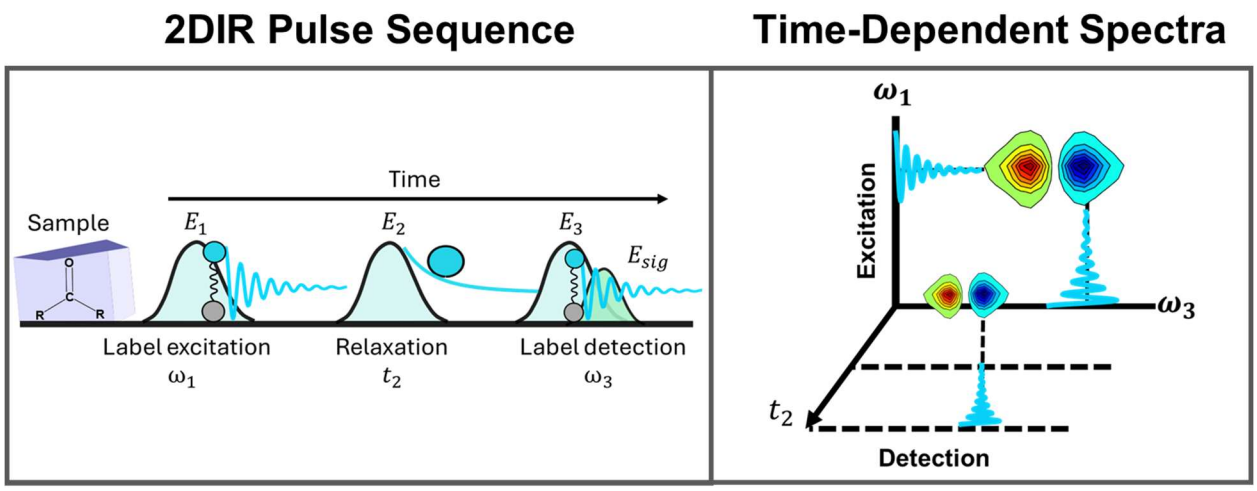

Figure 1.2.2-1: **Left.** Example 2DIR pulse sequence and molecular response pathway. The chemical sample is perturbed by three time-ordered mid-IR pulses, represented by light blue gaussian envelopes. Vibrational superpositions are depicted as two balls connected by a spring. The excited state population generated by the second pulse is represented by a light-blue circle. The third pulse generates another coherence state, whose emitted radiation contributes to the 2DIR signal. **Right.** Cartoon representation of a time-dependent 2D IR experiment for a single vibrational mode. The coherences generated by the first and third pulses are displayed on the ω_1 and ω_3 axes, respectively.

The ability of 2DIR to track both population and coherence dynamics makes it a powerful tool for investigating vibrational relaxation in chemical systems. By monitoring population dynamics during the waiting time, 2DIR experiments provide insights into the factors that influence the redistribution and dissipation of vibrational energy. Studies of vibrational population dynamics using 2DIR have been used to develop microscopic pictures of how hydrogen bonding influences vibrational relaxation rates[38,39] and to develop strategies for modifying intramolecular relaxation pathways based on the manipulation of vibrational couplings.[40–42] Ultimately, the information extracted from time-dependent 2DIR experiments can provide insights into the strength of resonance coupling between vibrational modes and interactions with the surrounding bath, which consists of solvent degrees of freedom and other internal molecular vibrations. However, interpreting

2DIR experiments requires theoretical frameworks that link experimental observables to underlying molecular dynamics. The next section provides background on the Redfield framework, a commonly used approach for describing vibrational dynamics in 2DIR.

1.3 Vibrational Dynamics in the Redfield Framework

Coupling between a molecular system and the surrounding environment, or "bath," gives rise to vibrational dynamics.[13,43–45] The bath may consist of both internal and external degrees of freedom, with its specific definition depending on the chosen model. In practice, the bath consists of all degrees of freedom not explicitly considered part of the "system" under study. The redistribution of energy between system states coincides with an equal change of energy in the bath. Redfield theory provides a microscopic description of vibrational relaxation by treating weak system-bath coupling with second order perturbation theory. [43,46–50] Redfield theory relies on the density matrix formalism of quantum mechanics. In the density matrix formalism, the diagonal elements of the density matrix, ρ, describe vibrational population states, which represent the probability of the system occupying a specific vibrational energy level. The off-diagonal coherence states give the phase relationships between elements of vibrational superpositions of system states. The Redfield equation describes the time evolution of the system density matrix, and is given as:[18,43,51]

(1-1) $$\frac{\partial}{\partial t}\rho_{ab}(\mathrm{t}) = -i\omega_{ab}\rho_{ab}(\mathrm{t}) - \sum_{cd} R_{ab,cd}\rho_{cd}.$$

Here ρ_{ab} is a given density matrix element, ω_{ab} corresponds to the frequency of ρ_{ab}, and the operator R_{abcd} encodes the relaxation terms. The Redfield equation states that the time evolution of a given density matrix element ρ_{ab}, is linked to each density matrix

element ρ_{cd} through the system-bath interactions encoded in $R_{ab,cd}$. The system operators contained in R_{abcd} describe the likelihood that interaction with the thermal bath induces energy transfer between system states.

Standard descriptions of 2DIR spectroscopy invoke the secular approximation to Redfield theory.[52–54] The secular approximation does not consider the elements of $R_{ab,cd}$ for which $\omega_{ab} \neq \omega_{cd}$. Population states such as ρ_{aa} evolve without phase, meaning that $\omega_{aa} = \omega_{bb} = 0$. Under the secular approximation, only terms such as $R_{ab,ab}$, $R_{aa,aa}$, and $R_{aa,bb}$ contribute to vibrational relaxation. Terms where the first and second pair of indices are the same ($R_{ab,ab}$, $R_{aa,aa}$) reflect the decay rates of density matrix elements due to interactions with the bath, while terms in which the first and second pair of indices are different ($R_{aa,bb}$) describe the transfer of amplitude from one density matrix element to another. The three sets of terms surviving the secular approximation describe coherence dephasing ($R_{ab,ab}$), population relaxation ($R_{aa,aa}$), and population transfer ($R_{aa,bb}$). When incorporated into theoretical descriptions of 2DIR, the secular approximation greatly simplified the interpretation and modeling of 2DIR experiments.[17,19,51,55] However, the secular approximation does not account for the intrasystem relaxation of vibrational superpositions. More robust descriptions of coherent dynamics must also account for coherence transfer ($R_{ab,cd}$) and coherence-population coupling ($R_{cd,aa}, R_{aa,cd}$). Coherence transfer (CT) is the quantum mechanical analog of population transfer, in which one coherent superposition converts into another. [56,57] Coherence-population coupling describes how vibrational coherences can influence the populations of specific vibrational energy levels, and vice versa.[58] As such,

there is interest in applying nonsecular models of 2DIR spectroscopy to study a wider range of coherent relaxation processes.

1.3.2 Studying Nonsecular Relaxation with 2DIR

Characterizing the dynamics of vibrational coherences using nonsecular descriptions of 2DIR remains an active area of research. Since Khalil and Tokmakoff first demonstrated the ability of nonsecular models to describe anomalous peaks in the 2DIR spectrum of $Rh(CO)_2(acac)$,[51] researchers have been interested in understanding how nonsecular processes manifest in experimental spectra and what chemical information those manifestations contain. Efforts at identifying spectroscopic signatures of coherence transfer have been the more successful thrust. Predictions of how nonsecular processes manifest under experimental conditions such as pulse polarization[59], excitation bandwidth[19], and the relative phases of the 2DIR pulse train[56,60] have produced a series of experimental tests for coherent dynamics. Applications of these methods to the study of the Fermi doublet of ethylene carbonate are the focus of chapter 3.

However, relating the observation of coherent vibrational dynamics to the properties of chemical systems remains challenging. For instance, a study of coherence transfer in the spectrum of dimanganese dodecacarbonyl[17] identified spectroscopic signatures of only a handful of theoretically predicted coherence transfer pathways, with the authors noting a lack of guiding principles for predicting which pathways are most likely to be observed experimentally. A theoretical investigation of the same system by Baiz et al.[55] attempted to resolve this discrepancy by comparing nonsecular relaxation

rates for models containing different numbers of dark vibrational modes. Their results suggest that observed coherence transfer rates depend on vibrational coupling between both experimentally observable transitions and dark states traditionally associated with the bath. Villaeys and Liang found that anomalous cross peaks in the 2DIR spectrum of benzonitrile and acetonitrile-d_3 mixtures could be modeled from intermolecular coherence transfer processes involving specific dark states which become populated by the dissipation of energy out of optically excited transitions.[61] Those results, which explicitly consider bright-dark anharmonic couplings, indicate a direct relationship between relaxation pathways involving dark states and the observation of coherent dynamics. The role of dark states in enabling the observation of coherent dynamics in 2DIR spectra was experimentally investigated by Eckert and Kubarych in a study of three diiron hexacarbonyl systems.[18] The authors found coherent oscillations in 2DIR cross peaks whose beating frequency corresponded to the energy gap between bright and dark vibrational modes, which could only be attributed to coherence transfer processes involving IR-inactive vibrations. Further, they found that chemical substitution of the bridging dithiolate group led to observation of unique coherent relaxation pathways in each compound. Their results prove interesting, as they indicate the possibility of manipulating coherent dynamics via straightforward chemical modifications. Modifying coherent dynamics by altering the nature of coupling to dark states would mark an important step towards developing chemically insightful models of coherent relaxation in 2DIR. Such an effort is the topic of chapter 4 of this dissertation.

1.4 Motivation for Studying the Vibrational Dynamics of Ethylene Carbonate (EC)

While this work uses EC as a model system for investigating coherent relaxation, the interest in studying its vibrational dynamics stems from its role as an electrolyte component in energy storage devices. Specifically, EC serves as a component of organic electrolyte mixtures composed of linear and cyclic carbonates in lithium-ion batteries.[62–68] The carbonyl stretching mode of several linear and cyclic carbonates have served as IR probes in 2DIR studies of lithium ion solvation.[62–65] However, overlapping IR peaks in the carbonyl region of multicomponent electrolytes challenge the unambiguous assignment of ion solvation structure and dynamics.[69–71] A linear IR absorption spectrum for a 1:1:1 molar equivalent mixture of diethyl carbonate (DEC), dimethyl carbonate (DMC), and EC is shown in figure 1.4-1. Three peaks appear in the spectrum shown in figure 1.4-1. Two of those peaks correspond to the Fermi doublet of EC, while the lowest frequency peak corresponds to an overlap of the carbonyl stretch of the linear carbonates DEC and DMC.

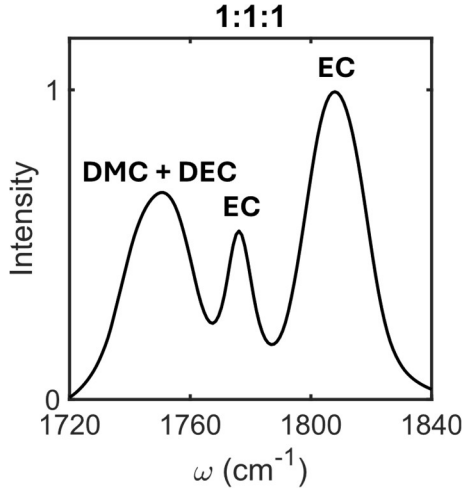

Figure 1.4-1: Linear IR absorption spectrum for the carbonyl region of a 1:1:1 molar mixture of DEC, DMC, and EC.

Spectral congestion presents additional challenges in 2DIR spectroscopy, where excited state absorption and cross peaks additionally contribute to peak overlap. Extracting chemical information from 2DIR spectra requires distinguishing the contributions of different molecular processes that contribute to the intensity and time evolution of each peak. The discovery of coherent relaxation pathways in EC, detailed in chapter 3, introduces additional complexity, as these processes can obscure or mimic the contributions of conventional pathways.

1.5 Dissertation Outline

The remainder of this dissertation is laid out as follows: Chapter 2 provides a description of the experimental techniques and theoretical tools used to characterize vibrational relaxation pathways in EC and closely related molecules. Chapter 3 details the identification of coherent relaxation pathways in EC using 2DIR spectroscopy, while chapter 4 compares the signatures of coherent relaxation pathways in a series of EC ^{13}C isotopologues. Chapter 5 summarizes the conclusions of chapters 3 and 4 and discusses future applications of isotopic substitution for suppressing coherent relaxation and eliminating spectral congestion in mixtures of organic carbonates containing EC.

References

(1) Levi, F.; Mostarda, S.; Rao, F.; Mintert, F. Quantum Mechanics of Excitation Transport in Photosynthetic Complexes: A Key Issues Review. *Rep. Prog. Phys.* **2015**, *78* (8), 082001. https://doi.org/10.1088/0034-4885/78/8/082001.

(2) Abramavicius, D.; Valkunas, L. Role of Coherent Vibrations in Energy Transfer and Conversion in Photosynthetic Pigment–Protein Complexes. *Photosynth Res* **2016**, *127* (1), 33–47. https://doi.org/10.1007/s11120-015-0080-6.

(3) Fassioli, F.; Dinshaw, R.; Arpin, P. C.; Scholes, G. D. Photosynthetic Light Harvesting: Excitons and Coherence. *Journal of The Royal Society Interface* **2014**, *11* (92), 20130901. https://doi.org/10.1098/rsif.2013.0901.

(4) Rather, S. R.; Bezdek, M. J.; Chirik, P. J.; Scholes, G. D. Dinitrogen Coupling to a Terpyridine-Molybdenum Chromophore Is Switched on by Fermi Resonance. *Chem* **2024**, *10* (3), 1028. https://doi.org/10.1016/j.chempr.2024.01.021.

(5) Leitner, D. M. Illuminating Fermi Resonances That Trigger Reaction in a Complex Molecule. *Chem* **2019**, *5* (2), 256–257. https://doi.org/10.1016/j.chempr.2018.12.023.

(6) Gruebele, M.; Wolynes, P. G. Vibrational Energy Flow and Chemical Reactions. *Acc. Chem. Res.* **2004**, *37* (4), 261–267. https://doi.org/10.1021/ar030230t.

(7) Cui, X.; Ruan, Q.; Zhuo, X.; Xia, X.; Hu, J.; Fu, R.; Li, Y.; Wang, J.; Xu, H. Photothermal Nanomaterials: A Powerful Light-to-Heat Converter. *Chem. Rev.* **2023**, *123* (11), 6891–6952. https://doi.org/10.1021/acs.chemrev.3c00159.

(8) Fabrikant, M. I.; Lauria, P.; Madjarov, I. S.; Burton, W. C.; Sutherland, R. T. Cooling Trapped Ions with Phonon Rapid Adiabatic Passage. arXiv March 18, 2024. https://doi.org/10.48550/arXiv.2403.02315.

(9) Walschaers, M.; Schlawin, F.; Wellens, T.; Buchleitner, A. Quantum Transport on Disordered and Noisy Networks: An Interplay of Structural Complexity and Uncertainty. *Annual Review of Condensed Matter Physics* **2016**, *7* (Volume 7, 2016), 223–248. https://doi.org/10.1146/annurev-conmatphys-031115-011327.

(10) Rather, S. R.; Scholes, G. D. From Fundamental Theories to Quantum Coherences in Electron Transfer. *J. Am. Chem. Soc.* **2019**, *141* (2), 708–722. https://doi.org/10.1021/jacs.8b09059.

(11) Scholes, G. D.; Fleming, G. R.; Chen, L. X.; Aspuru-Guzik, A.; Buchleitner, A.; Coker, D. F.; Engel, G. S.; van Grondelle, R.; Ishizaki, A.; Jonas, D. M.; Lundeen, J. S.; McCusker, J. K.; Mukamel, S.; Ogilvie, J. P.; Olaya-Castro, A.; Ratner, M. A.; Spano, F. C.; Whaley, K. B.; Zhu, X. Using Coherence to Enhance Function in Chemical and Biophysical Systems. *Nature* **2017**, *543* (7647), 647–656. https://doi.org/10.1038/nature21425.

(12) Bai, S.; Zhang, S.; Huang, C.; Shi, Q. Hierarchical Equations of Motion for Quantum Chemical Dynamics: Recent Methodology Developments and Applications. *Acc. Chem. Res.* **2024**, *57* (21), 3151–3160. https://doi.org/10.1021/acs.accounts.4c00492.

(13) Tanimura, Y. Numerically “Exact” Approach to Open Quantum Dynamics: The Hierarchical Equations of Motion (HEOM). *The Journal of Chemical Physics* **2020**, *153* (2), 020901. https://doi.org/10.1063/5.0011599.

(14) Takahashi, H.; Tanimura, Y. Simulating Two-Dimensional Correlation Spectroscopies with Third-Order Infrared and Fifth-Order Infrared–Raman Processes of Liquid Water. *The Journal of Chemical Physics* **2023**, *158* (12), 124108. https://doi.org/10.1063/5.0141181.

(15) Balzer, B.; Stock, G. Modeling of Decoherence and Dissipation in Nonadiabatic Photoreactions by an Effective-Scaling Nonsecular Redfield Algorithm. *Chemical Physics* **2005**, *310* (1), 33–41. https://doi.org/10.1016/j.chemphys.2004.10.001.

(16) Tanimura, Y.; Mukamel, S. Real-Time Path-Integral Approach to Quantum Coherence and Dephasing in Nonadiabatic Transitions and Nonlinear Optical Response. *Phys. Rev. E* **1993**, *47* (1), 118–136. https://doi.org/10.1103/PhysRevE.47.118.

(17) Nee, M. J.; Baiz, C. R.; Anna, J. M.; McCanne, R.; Kubarych, K. J. Multilevel Vibrational Coherence Transfer and Wavepacket Dynamics Probed with Multidimensional IR Spectroscopy. *The Journal of Chemical Physics* **2008**, *129* (8), 084503. https://doi.org/10.1063/1.2969900.

(18) Eckert, P. A.; Kubarych, K. J. Vibrational Coherence Transfer Illuminates Dark Modes in Models of the FeFe Hydrogenase Active Site. *The Journal of Chemical Physics* **2019**, *151* (5), 054307. https://doi.org/10.1063/1.5111016.

(19) Marroux, H. J. B.; Orr-Ewing, A. J. Distinguishing Population and Coherence Transfer Pathways in a Metal Dicarbonyl Complex Using Pulse-Shaped Two-Dimensional Infrared Spectroscopy. *J. Phys. Chem. B* **2016**, *120* (17), 4125–4130. https://doi.org/10.1021/acs.jpcb.6b02979.

(20) Gruebele, M.; Bigwood, R. Molecular Vibrational Energy Flow: Beyond the Golden Rule. *International Reviews in Physical Chemistry* **1998**, *17* (2), 91–145. https://doi.org/10.1080/014423598230117.

(21) Fujisaki, H.; Yagi, K.; Kikuchi, H.; Takami, T.; Stock, G. Vibrational Energy Transport in Acetylbenzonitrile Described by an *Ab Initio*-Based Quantum Tier Model. *Chemical Physics* **2017**, *482*, 86–92. https://doi.org/10.1016/j.chemphys.2016.09.010.

(22) Hamm, P.; Zanni, M. *Concepts and Methods of 2D Infrared Spectroscopy*; Cambridge University Press: Cambridge, 2011. https://doi.org/10.1017/CBO9780511675935.

(23) Tucker, M. J.; Kim, Y. S.; Hochstrasser, R. M. 2D IR Photon Echo Study of the Anharmonic Coupling in the OCN Region of Phenyl Cyanate. *Chemical Physics Letters* **2009**, *470* (1), 80–84. https://doi.org/10.1016/j.cplett.2009.01.025.

(24) Child, M. S.; Lawton, R. T. Local and Normal Vibrational States: A Harmonically Coupled Anharmonic-Oscillator Model. *Faraday Discuss. Chem. Soc.* **1981**, *71* (0), 273–285. https://doi.org/10.1039/DC9817100273.

(25) Bertran, J. F.; Ballester, L.; Dobrihalova, L.; Sánchez, N.; Arrieta, R. Study of Fermi Resonance by the Method of Solvent Variation. *Spectrochimica Acta Part A: Molecular Spectroscopy* **1968**, *24* (11), 1765–1776. https://doi.org/10.1016/0584-8539(68)80232-6.

(26) Kondratyuk, P. Analytical Formulas for Fermi Resonance Interactions in Continuous Distributions of States. *Spectrochimica Acta Part A: Molecular and Biomolecular Spectroscopy* **2005**, *61* (4), 589–593. https://doi.org/10.1016/j.saa.2004.05.010.

(27) Devendorf, G. S.; Hu, M.-H. A.; Ben-Amotz, D. Pressure Dependent Vibrational Fermi Resonance in Liquid CH3OH and CH2Cl2. *J. Phys. Chem. A* **1998**, *102* (52), 10614–10619. https://doi.org/10.1021/jp983068y.

(28) Curnow, O. J.; Crittenden, D. L. Are “Bright-State” Models Appropriate for Analyzing Fermi-Coupled Bands in Molecular Vibrational Spectra? *J. Phys. Chem. A* **2021**, *125* (6), 1355–1358. https://doi.org/10.1021/acs.jpca.0c10404.

(29) Schindler, W.; Zerda, T. W.; Jonas, J. High Pressure Raman Study of Intermolecular Interactions and Fermi Resonance in Liquid Ethylene Carbonate. *The Journal of Chemical Physics* **1984**, *81* (10), 4306–4313. https://doi.org/10.1063/1.447440.

(30) Fortunato, B.; Mirone, P.; Fini, G. Infrared and Raman Spectra and Vibrational Assignment of Ethylene Carbonate. *Spectrochimica Acta Part A: Molecular Spectroscopy* **1971**, *27* (9), 1917–1927. https://doi.org/10.1016/0584-8539(71)80245-3.

(31) *Vibrational States and Nitrile Lifetimes of Cyanophenylalanine Isotopomers in Solution | The Journal of Physical Chemistry A*. https://pubs.acs.org/doi/full/10.1021/acs.jpca.8b06300 (accessed 2024-10-18).

(32) Sibert, E. L., III; Hynes, J. T.; Reinhardt, W. P. Classical Dynamics of Highly Excited CH and CD Overtones in Benzene and Perdeuterobenzene. *The Journal of Chemical Physics* **1984**, *81* (3), 1135–1144. https://doi.org/10.1063/1.447806.

(33) Sibert, E. L., III; Reinhardt, W. P.; Hynes, J. T. Intramolecular Vibrational Relaxation and Spectra of CH and CD Overtones in Benzene and Perdeuterobenzene. *The Journal of Chemical Physics* **1984**, *81* (3), 1115–1134. https://doi.org/10.1063/1.447805.

(34) Bigwood, R.; Gruebele, M.; Leitner, D. M.; Wolynes, P. G. The Vibrational Energy Flow Transition in Organic Molecules: Theory Meets Experiment. *Proceedings of the National Academy of Sciences* **1998**, *95* (11), 5960–5964. https://doi.org/10.1073/pnas.95.11.5960.

(35) Zhang, J.; Wang, L.; Zhang, J.; Zhu, J.; Pan, X.; Cui, Z.; Wang, J.; Fang, W.; Li, Y. Identifying and Modulating Accidental Fermi Resonance: 2D IR and DFT Study of 4-Azido-l-Phenylalanine. *J. Phys. Chem. B* **2018**, *122* (34), 8122–8133. https://doi.org/10.1021/acs.jpcb.8b03887.

(36) Chuntonov, L.; Kuroda, D. G.; Ghosh, A.; Ma, J.; Hochstrasser, R. M. Quantum Beats and Coherence Decay in Degenerate States Split by Solvation. *J Phys Chem Lett* **2013**, *4* (11), 1866–1871. https://doi.org/10.1021/jz400826a.

(37) Rector, K. D.; Kwok, A. S.; Ferrante, C.; Tokmakoff, A.; Rella, C. W.; Fayer, M. D. Vibrational Anharmonicity and Multilevel Vibrational Dephasing from Vibrational Echo Beats. *The Journal of Chemical Physics* **1997**, *106* (24), 10027–10036. https://doi.org/10.1063/1.474060.

(38) Hamm, P.; Lim, M.; Hochstrasser, R. M. Structure of the Amide I Band of Peptides Measured by Femtosecond Nonlinear-Infrared Spectroscopy. *J. Phys. Chem. B* **1998**, *102* (31), 6123–6138. https://doi.org/10.1021/jp9813286.

(39) King, J. T.; Ross, M. R.; Kubarych, K. J. Water-Assisted Vibrational Relaxation of a Metal Carbonyl Complex Studied with Ultrafast 2D-IR. *J. Phys. Chem. B* **2012**, *116* (12), 3754–3759. https://doi.org/10.1021/jp2125747.

(40) Schmitz, A. J.; Pandey, H. D.; Chalyavi, F.; Shi, T.; Fenlon, E. E.; Brewer, S. H.; Leitner, D. M.; Tucker, M. J. Tuning Molecular Vibrational Energy Flow within an Aromatic Scaffold via Anharmonic Coupling. *J. Phys. Chem. A* **2019**, *123* (49), 10571–10581. https://doi.org/10.1021/acs.jpca.9b08010.

(41) Hassani, M.; Mallon, C. J.; Monzy, J. N.; Schmitz, A. J.; Brewer, S. H.; Fenlon, E. E.; Tucker, M. J. Inhibition of Vibrational Energy Flow within an Aromatic Scaffold via Heavy Atom Effect. *The Journal of Chemical Physics* **2023**, *158* (22), 224201. https://doi.org/10.1063/5.0153760.

(42) Bian, H.; Wen, X.; Li, J.; Zheng, J. Mode-Specific Intermolecular Vibrational Energy Transfer. II. Deuterated Water and Potassium Selenocyanate Mixture. *The Journal of Chemical Physics* **2010**, *133* (3), 034505. https://doi.org/10.1063/1.3458825.

(43) Redfield, A. G. The Theory of Relaxation Processes*. In *Advances in Magnetic and Optical Resonance*; Waugh, J. S., Ed.; Advances in Magnetic Resonance; Academic Press, 1965; Vol. 1, pp 1–32. https://doi.org/10.1016/B978-1-4832-3114-3.50007-6.

(44) Campaioli, F.; Cole, J. H.; Hapuarachchi, H. A Tutorial on Quantum Master Equations: Tips and Tricks for Quantum Optics, Quantum Computing and Beyond. arXiv March 29, 2023. https://doi.org/10.48550/arXiv.2303.16449.

(45) Kenkre, V. M.; Tokmakoff, A.; Fayer, M. D. Theory of Vibrational Relaxation of Polyatomic Molecules in Liquids. *The Journal of Chemical Physics* **1994**, *101* (12), 10618–10629. https://doi.org/10.1063/1.467876.

(46) Manzano, D. A Short Introduction to the Lindblad Master Equation. *AIP Advances* **2020**, *10* (2), 025106. https://doi.org/10.1063/1.5115323.

(47) Montoya-Castillo, A.; Berkelbach, T. C.; Reichman, D. R. Extending the Applicability of Redfield Theories into Highly Non-Markovian Regimes. *The Journal of Chemical Physics* **2015**, *143* (19), 194108. https://doi.org/10.1063/1.4935443.

(48) Abramavicius, D.; Mukamel, S. Quantum Oscillatory Exciton Migration in Photosynthetic Reaction Centers. *The Journal of Chemical Physics* **2010**, *133* (6), 064510. https://doi.org/10.1063/1.3458824.

(49) Palmieri, B.; Abramavicius, D.; Mukamel, S. Lindblad Equations for Strongly Coupled Populations and Coherences in Photosynthetic Complexes. *J Chem Phys* **2009**, *130* (20), 204512. https://doi.org/10.1063/1.3142485.

(50) Jang, S.; Cao, J.; Silbey, R. J. Fourth-Order Quantum Master Equation and Its Markovian Bath Limit. *The Journal of Chemical Physics* **2002**, *116* (7), 2705–2717. https://doi.org/10.1063/1.1445105.

(51) Khalil, M.; Demirdöven, N.; Tokmakoff, A. Vibrational Coherence Transfer Characterized with Fourier-Transform 2D IR Spectroscopy. *The Journal of Chemical Physics* **2004**, *121* (1), 362–373. https://doi.org/10.1063/1.1756870.

(52) Hartmann, R.; Strunz, W. T. Accuracy Assessment of Perturbative Master Equations: Embracing Nonpositivity. *Phys. Rev. A* **2020**, *101* (1), 012103. https://doi.org/10.1103/PhysRevA.101.012103.

(53) Eastham, P. R.; Kirton, P.; Cammack, H. M.; Lovett, B. W.; Keeling, J. Bath-Induced Coherence and the Secular Approximation. *Phys. Rev. A* **2016**, *94* (1), 012110. https://doi.org/10.1103/PhysRevA.94.012110.

(54) Ishizaki, A.; Fleming, G. R. On the Adequacy of the Redfield Equation and Related Approaches to the Study of Quantum Dynamics in Electronic Energy Transfer. *The Journal of Chemical Physics* **2009**, *130* (23), 234110. https://doi.org/10.1063/1.3155214.

(55) Baiz, C. R.; Kubarych, K. J.; Geva, E. Molecular Theory and Simulation of Coherence Transfer in Metal Carbonyls and Its Signature on Multidimensional Infrared Spectra. *J. Phys. Chem. B* **2011**, *115* (18), 5322–5339. https://doi.org/10.1021/jp109357d.

(56) Pakoulev, A. V.; Rickard, M. A.; Mathew, N. A.; Kornau, K. M.; Wright, J. C. Frequency-Domain Time-Resolved Four Wave Mixing Spectroscopy of Vibrational Coherence Transfer with Single-Color Excitation. *J. Phys. Chem. A* **2008**, *112* (28), 6320–6329. https://doi.org/10.1021/jp711014h.

(57) Rickard, M. A.; Pakoulev, A. V.; Kornau, K.; Mathew, N. A.; Wright, J. C. Interferometric Coherence Transfer Modulations in Triply Vibrationally Enhanced Four-Wave Mixing. *J. Phys. Chem. A* **2006**, *110* (40), 11384–11387. https://doi.org/10.1021/jp063917e.

(58) Collini, E. Spectroscopic Signatures of Quantum-Coherent Energy Transfer. *Chemical Society Reviews* **2013**, *42* (12), 4932–4947. https://doi.org/10.1039/C3CS35444J.

(59) Chuntonov, L.; Ma, J. Quantum Process Tomography Quantifies Coherence Transfer Dynamics in Vibrational Exciton. *J. Phys. Chem. B* **2013**, *117* (43), 13631–13638. https://doi.org/10.1021/jp4075493.

(60) Rickard, M. A.; Pakoulev, A. V.; Mathew, N. A.; Kornau, K. M.; Wright, J. C. Frequency- and Time-Resolved Coherence Transfer Spectroscopy. *J. Phys. Chem. A* **2007**, *111* (7), 1163–1166. https://doi.org/10.1021/jp0677804.

(61) Villaeys, A. A.; Liang, K. K. Description of Cross-Peaks Induced by Intermolecular Vibrational Energy Transfer in Two-Dimensional Infrared Spectroscopy. *Chemical Physics* **2015**, *450–451*, 12–20. https://doi.org/10.1016/j.chemphys.2015.01.010.

(62) Galle Kankanamge, S. R.; Kuroda, D. G. Molecular Structure, Chemical Exchange, and Conductivity Mechanism of High Concentration LiTFSI Electrolytes. *J. Phys. Chem. B* **2020**, *124* (10), 1965–1977. https://doi.org/10.1021/acs.jpcb.9b10795.

(63) Fulfer, K. D.; Kuroda, D. G. Solvation Structure and Dynamics of the Lithium Ion in Organic Carbonate-Based Electrolytes: A Time-Dependent Infrared Spectroscopy Study. *J. Phys. Chem. C* **2016**, *120* (42), 24011–24022. https://doi.org/10.1021/acs.jpcc.6b08607.

(64) Fulfer, K. D.; Kuroda, D. G. A Comparison of the Solvation Structure and Dynamics of the Lithium Ion in Linear Organic Carbonates with Different Alkyl Chain Lengths. *Phys. Chem. Chem. Phys.* **2017**, *19* (36), 25140–25150. https://doi.org/10.1039/C7CP05096H.

(65) Liang, C.; Kwak, K.; Cho, M. Revealing the Solvation Structure and Dynamics of Carbonate Electrolytes in Lithium-Ion Batteries by Two-Dimensional Infrared Spectrum Modeling. *J. Phys. Chem. Lett.* **2017**, *8* (23), 5779–5784. https://doi.org/10.1021/acs.jpclett.7b02623.

(66) Lim, C.; Kim, J. H.; Chae, Y.; Lee, K.-K.; Kwak, K.; Cho, M. Solvation Structure around Li+ Ions in Organic Carbonate Electrolytes: Spacer-Free Thin Cell IR

Spectroscopy. *Anal. Chem.* **2021**, *93* (37), 12594–12601. https://doi.org/10.1021/acs.analchem.1c02127.

(67) Zhang, X.; Kuroda, D. G. An Ab Initio Molecular Dynamics Study of the Solvation Structure and Ultrafast Dynamics of Lithium Salts in Organic Carbonates: A Comparison between Linear and Cyclic Carbonates. *The Journal of Chemical Physics* **2019**, *150* (18), 184501. https://doi.org/10.1063/1.5088820.

(68) Jiang, B.; Ponnuchamy, V.; Shen, Y.; Yang, X.; Yuan, K.; Vetere, V.; Mossa, S.; Skarmoutsos, I.; Zhang, Y.; Zheng, J. The Anion Effect on Li+ Ion Coordination Structure in Ethylene Carbonate Solutions. *J. Phys. Chem. Lett.* **2016**, *7* (18), 3554–3559. https://doi.org/10.1021/acs.jpclett.6b01664.

(69) Lim, C.; Jeon, J.; Park, K.; Liang, C.; Chae, Y.; Kwak, K.; Cho, M. Revisiting Ultrafast Dynamics in Carbonate-Based Electrolytes for Li-Ion Batteries: Clarifying 2D-IR Cross-Peak Interpretation. *J. Phys. Chem. B* **2023**, *127* (44), 9566–9574. https://doi.org/10.1021/acs.jpcb.3c05480.

(70) Lee, K.-K.; Park, K.; Lee, H.; Noh, Y.; Kossowska, D.; Kwak, K.; Cho, M. Ultrafast Fluxional Exchange Dynamics in Electrolyte Solvation Sheath of Lithium Ion Battery. *Nat Commun* **2017**, *8* (1), 14658. https://doi.org/10.1038/ncomms14658.

(71) Dereka, B.; Lewis, N. H. C.; Zhang, Y.; Hahn, N. T.; Keim, J. H.; Snyder, S. A.; Maginn, E. J.; Tokmakoff, A. Exchange-Mediated Transport in Battery Electrolytes: Ultrafast or Ultraslow? *J. Am. Chem. Soc.* **2022**, *144* (19), 8591–8604. https://doi.org/10.1021/jacs.2c00154.

Chapter 2
Experimental and Theoretical Methods

This chapter provides an overview of two-dimensional infrared spectroscopy (2DIR), details of the experimental equipment, and data analysis methods used in this dissertation. The goal of this dissertation is to use 2DIR to assess the role of vibrational coupling in facilitating coherent vibrational relaxation mechanisms in ethylene carbonate (EC) and two of its ^{13}C isotopologues. EC has been employed in mixtures of organic carbonates that serve as the electrolyte of lithium-ion batteries.[1–7] Such mixtures have been the focus of several time-dependent vibrational spectroscopy investigations,[1–4] but few studies probe the vibrational dynamics of EC directly.[7,8]

The chapter begins by providing an overview of 2DIR spectroscopy and the Feynman diagram representation of nonlinear response functions for a single vibrational mode. Next, an overview of the 100 kHz 2DIR spectrometer used in these experiments is provided. Methods for extracting rephasing and nonrephasing signals from the experimental conditions used in this dissertation are then given. The penultimate section of this chapter revisits the Feynman diagram picture for a system of two coupled oscillators and discusses the incorporation of coherent relaxation processes in Feynman diagrams as well as their effects on 2DIR spectra. The final section of this chapter details data analysis methods for studying vibrational dynamics with 2DIR.

2.1 Overview of 2DIR Spectroscopy

The signal recorded by a 2DIR experiment is the third order macroscopic polarization of the sample, which depends on the interaction of the molecular ensemble of oscillators and three sequential perturbations by mid-IR light. The macroscopic polarization is given as

$$P^{(3)} \propto \int_0^\infty dt_3 \int_0^\infty dt_2 \int_0^\infty dt_1 \, E_3(t-t_3)E_2(t-t_3-t_2)E_1(t-t_3-t_2-t_1) \cdot R^{(3)}(t_3,t_2,t_1). \tag{2-1}$$

Here, E_1, E_2, and E_3 are the electric fields of the three incident laser pulses. The subscript of each pulse denotes their time ordering, with E_1 arriving at the sample first and E_3 arriving last. The experimental time intervals between each set of pulses are denoted by t_1 and t_2, while t_3 describes the time period over which the signal is emitted by the sample. $R^{(3)}$ is the third order response function of the chemical system which encodes not only the evolution of the system due to interactions with the mid-IR laser pulses but also the vibrational relaxation of the system during the experimental time delays. Full derivations of the macroscopic polarization and molecular response functions are given elsewhere.[9,10] The total third order response function can be written as

$$R^{(3)}(t_3,t_2,t_1) = \left(\frac{i}{\hbar}\right)^3 \langle \mu(t_1+t_2+t_3)\left[\mu(t_1+t_2),\left[\mu(t_1),[\mu(0),\rho(-\infty)]\right]\right]\rangle. \tag{2-2}$$

In this equation, $\mu(t)$ is the transition dipole moment operator that describes the likelihood of a perturbation by an electric field to drive transitions between vibrational eigenstates, and $\rho(-\infty)$ is the system density matrix before the first light matter interaction, for which it is assumed that the system resides entirely in the ground state population $|0\rangle\langle 0|$. The

factor $\left(\frac{i}{\hbar}\right)^3$ arises from the application of time-dependent perturbation theory to three light-matter interactions. Thus, the term $[\mu(0), \rho(-\infty)]$ describes the possible vibrational transitions from the ground state to vibrational excited states by a generic E_1 pulse. During the experimental time delays the evolution of ρ occurs due to anharmonic coupling between the system and bath. The remaining dipole operators in the expectation value of equation 2-2 describe the possible transitions between vibrational states induced by E_2 $(\mu(t_1))$ and E_3 $(\mu(t_1 + t_2))$ as well as the vibrational transitions which lead to the emission of the third order signal $(\mu(t_1 + t_2 + t_3))$ over t_3. As such, the dipole operators describe the probability of optically induced transitions, while the time evolution of the density matrix characterizes the vibrational dynamics during the interpulse periods.

2DIR spectra represent a collection of molecular response pathways which encode information on the energy levels and time evolution of different vibrational states. Extracting information about chemical systems from 2DIR spectra requires accounting for the various response pathways contributing to the experimental spectrum. It is often convenient to do so by representing molecular response pathways using double sided Feynman diagrams, which can be associated with specific features in a 2DIR spectrum. To illustrate how Feynman diagrams aid the interpretation of 2DIR spectra, we begin with a simple description of a 2DIR experiment for a single anharmonic oscillator which is represented by figure 2.1-1.

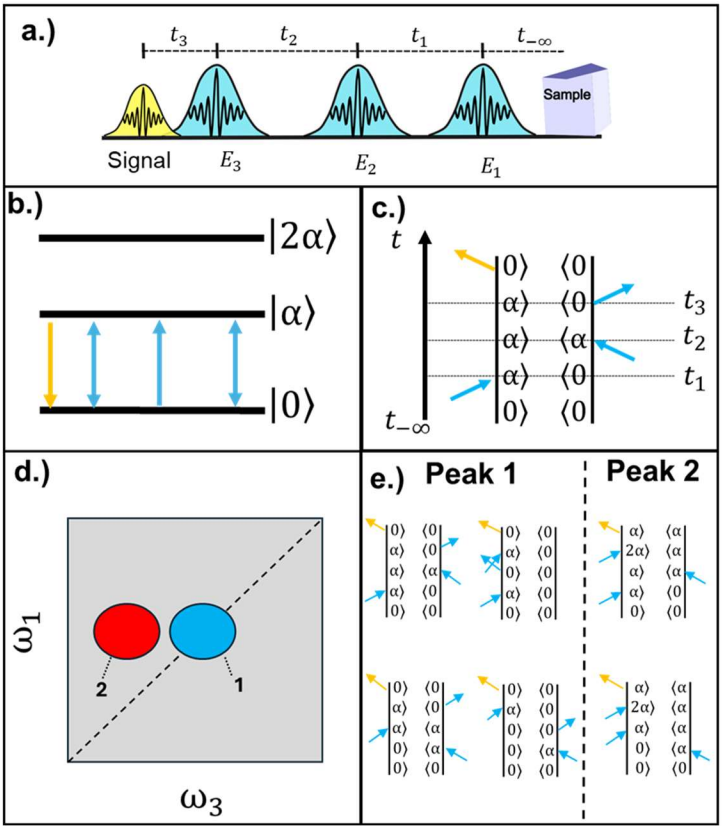

Figure 2.1-1: Overview of a 2DIR experiment for a single vibrational mode. **(a)** Depiction of the 2DIR pulse sequence described in the text. **(b)** Ladder diagram of a stimulated emission pathway accessed by a 2DIR experiment. Blue arrows correspond to the IR pulses. The yellow arrow corresponds to the emitted signal field. Double sided arrows indicate that the light-matter interaction generates a coherence state, while single sided arrows correspond to a change in vibrational populations. **(c)** Double sided Feynman diagram representation of the stimulated emission process depicted in **(b)**. Blue arrows represent interactions between the system and electric field. Yellow arrow represents the emitted signal. **(d)** Cartoon 2DIR spectrum for a single anharmonic oscillator. The dashed line indicates the diagonal line of the spectrum. **(e)** Double sided Feynman diagrams contributing to the peaks in the 2DIR spectrum shown in **d**.

Figure 2.1-1 gives an overview of a 2DIR experiment probing a single vibrational mode, $|\alpha\rangle$. A standard 2DIR pulse sequence is given in figure 2.1-1**a**. The input electric fields (blue) consist of two excitation or "pump" pulses (E_1 and E_2) and a single detection or "probe" pulse (E_3). After the sample interacts with the probe pulse, it emits a signal field (yellow) that encodes all molecular response pathways contributing to the 2DIR spectrum. One possible response pathway sampled in a 2DIR experiment describes the processes

of stimulated emission. Depictions of stimulated emission are given in the ladder diagram representation (2.1-1**b**) and the double-sided Feynman diagram representation (2.1-1**c**). Both representations convey similar information and are described in parallel. In figures 2.1-1**a** and 2.1-1**b** time increases from right to left, while in figure 2.1-1**c** time increases from bottom to top. Further details of the Feynman diagram representation are given in the next section. Before the arrival of E_1, the system occupies the ground population state at time $t = t_{-\infty}$, indicated by the lowest rung in figure 2.1-1**b** and the state $|0\rangle\langle 0|$ in figure 2.1-1**c**. When the first pump pulse arrives, it generates the coherence state $|\alpha\rangle\langle 0|$ which oscillates over t_1. The record of the signal over t_1 is then Fourier transformed to label the pathway at $\omega_{\alpha,0}$ on the ω_1 axis of the 2DIR spectrum in figure 2.1-1**d**. The second pulse collapses the coherence to generate an excited state population in $|\alpha\rangle\langle\alpha|$. The subsequent t_2 interval, often referred to as the waiting time, then reports on the relaxation of the vibrational population state $|\alpha\rangle\langle\alpha|$. After the waiting time of the experiment, E_3 converts the excited state population into the $|\alpha\rangle\langle 0|$ coherence state. The relaxation of $|\alpha\rangle\langle 0|$ emits a photon of frequency $\omega_{\alpha,0}$ which labels the pathway on the ω_3 axis of figure 2.1-1**d**.

The utility of the Feynman diagram representation lies in its ability to compactly relate the underlying response pathways to the (ω_1, ω_3) positions of different peaks in the 2DIR spectrum. For the stimulated emission pathway discussed above, the system occupies the same $|\alpha\rangle\langle 0|$ coherence during both the t_1 and t_3 coherence periods. As such, the pathway contributes to the diagonal ($\omega_1 = \omega_3$) peak in figure 2.1-1**d**, labeled as peak 1. Figure 2.1-1**e** gives additional Feynman diagrams which contribute to peak 1, as well as diagrams for the excited state absorption pathways contributing to peak 2. Note

that the excited state absorption pathways pass through the $|2\alpha\rangle\langle\alpha|$ coherence (or its complex conjugate) during t_3, causing them to appear at a different frequency on the ω_3 axis. This frequency shift corresponds to the vibrational anharmonicity of mode $|\alpha\rangle$. The different colors for the diagonal (blue) and off-diagonal (red) peaks in figure 2.1-1**d** indicate peaks with opposite amplitude signs. For the work presented herein, blue peaks indicate negative absorption amplitude due to ground state bleach or stimulated emission processes. For convenience, these peaks are collectively referred to as bleach features. Red peaks correspond to positive absorption amplitude due to excited state absorption processes. The change in the amplitude of different pathways arises due to a time-domain π phase shift between the emissive/bleaching and absorptive signals generated by the interaction with E_3. The ω_3 shift of the excited state absorption pathways relative to the bleach/emission pathways illustrates the idea that 2DIR spectra represent a 2D frequency-domain map of the coherences generated by E_1 and E_3.[11] The spectral position of a given response pathway can be read off from the first and last coherence states of the Feynman diagram. In the study of vibrational dynamics, this provides a tool to quickly relate t_2 evolution of the individual response pathways to peaks in the 2DIR spectrum. This feature will prove useful for illustrating the effects of nonsecular relaxation processes, which have not yet been considered, on the measurement and interpretation of 2DIR dynamical observables.

Rephasing and Nonrephasing Response Pathways

The previous section offered a description of stimulated emission pathways which treated the ladder and Feynman diagram representations as equivalent. However, the Feynman diagram representation provides additional information on the complex interactions between the chemical system and the electric field, providing additional details about the molecular response. Feynman diagrams can be separated into two classes, rephasing and nonrephasing, based on the phase conjugation of the t_1 and t_3 coherence states. Equivalently, the wavevector directions of the emitted signal ($\vec{k}_{sig}$) separates the rephasing ($\vec{k}_{sig} = -\vec{k}_1 + \vec{k}_2 + \vec{k}_3$) and nonrephasing ($\vec{k}_{sig} = +\vec{k}_1 - \vec{k}_2 + \vec{k}_3$) signals. The 2DIR spectra presented in this work were collected with a partly collinear beam geometry[12,13] for which $\vec{k}_1 = \vec{k}_2$ and $\vec{k}_{sig} = \vec{k}_3$.[9] The spectra are then collected as purely absorptive spectra, which are the sum of the rephasing and nonrephasing signals. Methods for extracting rephasing and nonrephasing signals from purely absorptive spectra are described in section 2.3. At present, we focus on how the two signals manifest in the Feynman diagram representation.

Stimulated emission pathways for both rephasing and nonrephasing diagrams are shown in figure 2.1-2.

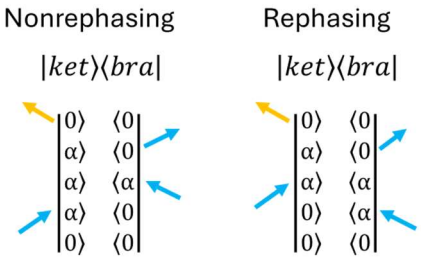

Figure 2.1-2: Rephasing (right) and nonrephasing (left) stimulated emission response pathways.

In the nonrephasing pathway, shown on the lefthand side of figure 2.1-2, the first light-matter interaction involves an excitation on the ket side of the density matrix. Conversely, in the rephasing pathway shown on the right, the first interaction occurs on the bra side. In the nonrephasing pathway, phase of the complex signal accumulates in the same direction ($|\alpha\rangle\langle 0|$) during both t_1 and t_3, leading to a continuous loss of coherence in the 2DIR signal. However, for rephasing pathways, phase accumulates in the opposite direction ($|0\rangle\langle\alpha|$) during the first coherence period. The phase reversal in the t_3 evolution of rephasing pathways produces a photon echo that enhances the signal. This echo can be observed by comparing the experimental rephasing (black) and nonrephasing (magenta) signals shown in figure 2.1-3. The signals shown in figure 2.1-3 were obtained from the experimental 2DIR spectrum of EC, which had not been Fourier transformed into the ω_1 frequency domain.

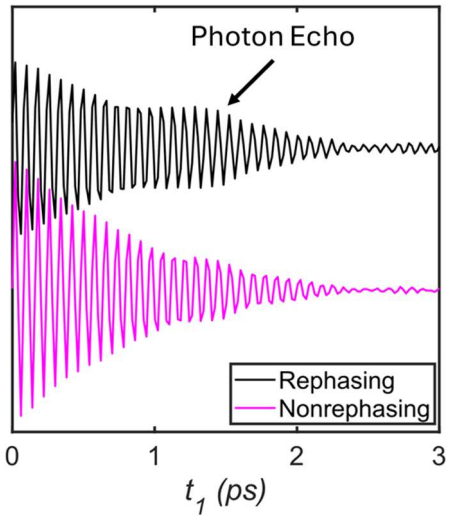

Figure 2.1-3: Rephasing (black) and nonrephasing (magenta) 2DIR signal taken from an experimental spectrum of ethylene carbonate. Time domain signals taken at ω_3 = 1811 cm^{-1} and t_2 = 0 ps. The horizontal axis gives the t_1 time interval out to 3 ps. The signal intensities have been self-normalized and offset to facilitate comparison.

We see that the envelope of the nonrephasing signal decays exponentially as a function of the t_1 coherence period. This decay reflects the accumulation of phase drift due to system-bath interactions. The rephasing signal is largely governed by the same decay, except for the appearance of a photon echo. This is denoted in figure 2.1-3 and can be seen by the increase in intensity of the rephasing signal. The significance of the photon echo in using 2DIR spectroscopy to characterize the timescales of dephasing processes is discussed further in section 2.5.1.

Rules for Interpreting Double Sided Feynman Diagrams

Before moving to a description of 2DIR spectra of coupled vibrational modes and their relaxation pathways (which will involve many Feynman diagrams), it is useful to review a non-exhaustive list of rules for interpreting the Feynman diagram representation of third order response functions.[9]

1.) The left and right sides of the diagram correspond to the time evolution of the ket and bra sides of the density matrix, respectively. Time increases from bottom to top.

2.) An arrow pointing inwards represents a process in which the system gains energy due to interactions with an external field, while arrows pointing outwards indicate a de-excitation process. The emitted signal always points outward.

3.) An arrow pointing to the right represents an electric field interaction with a positive wavevector ($\vec{k}_n$), and an arrow pointing to the left indicates a negative wavevector. The wavevector of the emitted signal is the sum of the wavevectors of the input fields and points to the left by convention.

2.2 100 kHz 2DIR Spectrometer

The following section details the 100 kHz mid-IR spectrometer used to perform the 2DIR experiments presented in chapters 3 and 4. The spectra contained in chapter 5 were obtained using a 1 kHz 2DIR spectrometer whose description can be found elsewhere.[14] A schematic of the 100 kHz laser system is shown in figure 2.2-1.

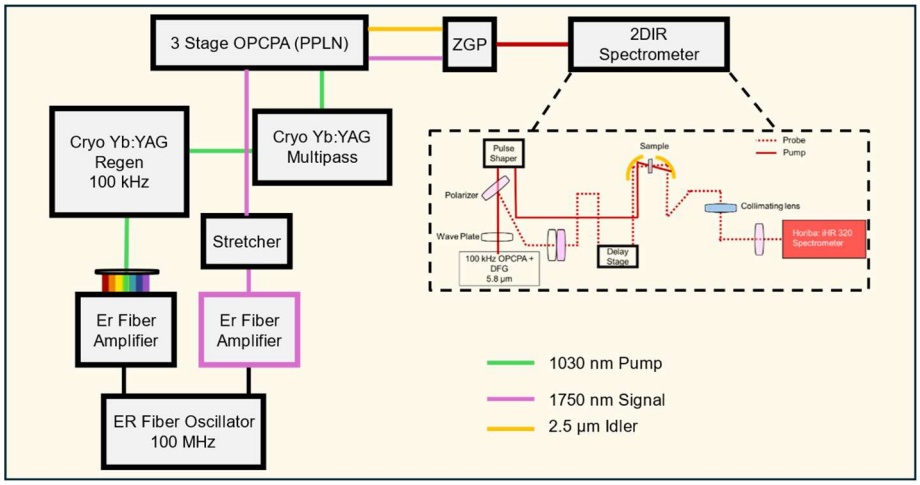

Figure 2.2-1: Schematic overview of the 100 kHz OPCPA 2DIR spectrometer used to perform 2DIR experiments.

Briefly, an erbium fiber oscillator seeds two fiber amplifiers (Menlo Systems) coupled to photonic crystal fibers (PCF). One PCF output is amplified by a pair of ytterbium doped yttrium aluminum garnet (Yb:YAG) amplifiers. The PCF outputs seed a three-stage periodically poled lithium niobate (PPLN) optical parametric chirped pulsed amplifier (OPCPA). The output beams of the OPCPA are converted to mid-IR through difference frequency generation (DFG) in a zinc germanium diphosphide (ZGP) crystal. The mid-IR output is split into pump and probe lines. The pump beam is sent to a mid-IR pulse shaper that uses a germanium acousto-optic modulator (AOM) to generate two excitation pulses for the 2DIR experiment. The probe beam is sent through a motorized delay stage before rejoining the pump beam at a pair of parabolic mirrors that focus the two beams onto the sample. The 2DIR signal emits collinearly with the probe beam. After the sample, the probe and signal travel to a spectrometer, where they are Fourier transformed by a diffraction grating and recorded on a 64-element mercury cadmium telluride (MCT) detector.

2.2.1 Generating Signal and Pump Beams for Nonlinear Frequency Conversion

Generation of the 100 kHz mid-IR pulse train used for 2DIR experiments begins with a Menlo Systems ELMO Erbium fiber oscillator whose 100 MHz output feeds into two Er fiber amplifiers coupled to two PCFs. The amplifiers generate 180 mW pulse trains for the pump and seed lines of the three-stage PPLN OPCPA. Setting the current of the seed amplifier to -100 mA produces a Raman shifted pulse train with a center wavelength of 1750 nm and 60 fs pulse duration. The seed pulses are stretched to reduce peak power before being sent to the OPCPA. The amplifier-PCF pair for the pump line produces a continuum which is sent through a 10 nm bandpass filter to isolate the region of the spectrum centered near 1030 nm which corresponds to the emission wavelength of cryogenically cooled Yb:YAG crystal. Before amplification the repetition rate of the pump line is downshifted to 100 kHz using a Pockels cell. The 100 kHz 1030 nm pulse train is then amplified in a cryogenically cooled Yb:YAG regenerative amplifier which produces a train of 10 ps pulses with a pulse energy of 55 μJ. The output of the regenerative amplifier is further amplified by a Yb:YAG multi-pass amplifier which increases the pulse energy to 300 μJ. The multi-pass output is then split into three lines, each of which pumps one OPCPA stage.[13]

2.2.2 Generation of mid-IR light: OPCPA and DFG

The three stage OPCPA uses PPLN crystals pumped by the 1030 nm pulse train to amplify the 1750 nm signal line. The amplified 1750 nm signal is retained for the first and second stages while the pump and idler are discarded. After the third OPCPA stage,

both the amplified 1750 nm signal and 2.5 μm idler are retained. The signal is compressed by a transmission grating compressor to a 106 fs pulse duration. The idler is compressed in a 250 mm silicon material compressor to produce 146 fs pulses. The signal and idler are then combined in a ZGP crystal where difference frequency generation produces mid-IR pulses centered at 5.8 μm.

2.2.3 100 kHz 2DIR Spectrometer

The mid-IR pulse train is split into pump and probe lines by a waveplate polarizer combination which determines the distribution of energy in the pump and probe pulses. The probe line is sent through another waveplate polarizer pair and travels to an electronically controlled delay stage which generates the t_2 dimension of the 2DIR experiments. The pump line passes through a mid-IR pulse shaper (QuickShape+, PhaseTech Spectroscopy) which will be discussed in the next section. The 2DIR experiments contained in this dissertation utilize a partly collinear beam geometry in which the pump and probe are slightly offset as they enter a pair of gold-plated parabolic mirrors. The parabolic mirrors focus the pump and probe beams onto the sample. After the sample the probe line is collimated, sent through a final polarizer, and into a Horiba iHR320 spectrometer where the signal is dispersed by a diffraction grating. The individual frequencies of the signal field are directed onto a 64-element mercury cadmium telluride detector (Infrared Systems) which generates the ω_3 axis of the 2DIR spectrum.

The noise introduced by shot-to-shot fluctuations in the probe pulse was treated using a two reference pixel noise reduction scheme. [15,16] In this scheme, two MCT pixels that do not carry 2DIR signal serve as reference pixels. The covariance between the shot-

to-shot noise of the reference (ΔI_{Ref}) and signal pixels (ΔI_{Sig}), along with the variance of ΔI_{Ref}, is recorded over 10,000 shots to obtain an optimized scaling factor from the linear regression of ΔI_{Sig} on ΔI_{Ref}. The form of the correction factor, b, is given by $b = \frac{cov(\Delta I_{Sig},\ \Delta I_{Ref})}{var(\Delta I_{Ref})}$. During the 2DIR experiment, the additive noise of subsequent laser shots is subtracted according to $\Delta I_{Sig} - \Delta I_{Ref} \cdot b$. This significantly reduces the shot-to-shot noise in the experimental data.

2.2.4 Mid-IR Pulse Shaper

The individual pulses in the pump line are split into a pair of temporally separated pulses by a mid-IR pulse shaper,[12] depicted in figure 2.2.4-1.

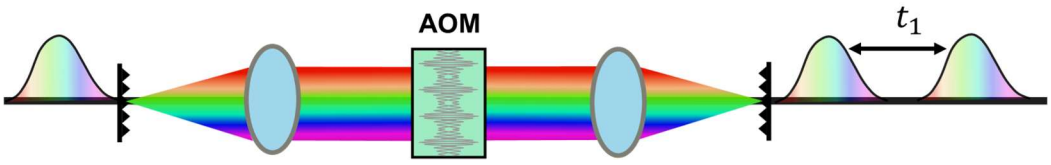

Figure 2.2.4-1: Cartoon depiction of an AOM pulse shaper. From left to right: A single input pulse is dispersed by a diffraction grating and focused onto a germanium crystal within the AOM. The acoustic waveform of the AOM alters the dispersion of different colors. The diffracted light is recollimated by a curved mirror and directed onto a diffraction grating such that the signal envelope produces two temporally separated pulses.

A broadband pulse enters the pulse shaper and is separated into its constituent frequency components using a diffraction grating. The diffracted beam is focused with a curved mirror and directed towards the germanium AOM, which sits in the focal plane of the shaper. A piezo-electric transducer generates an acoustic wave within the germanium window. The pressure gradient of the acoustic wave introduces a spatially dependent

refractive index that allows for controlling the dispersion of each color in the broadband pulse. The diffracted beam exits the AOM and is focused by a second curved mirror and directed onto a second grating. Using PhaseTech Software and a radio frequency waveform generator, the AOM is programmed to split the input pulse into a pair of temporally separated output pulses. Scanning the delay between the two output pulses generates the t_1 axis of the 2DIR experiment. Pump selective 2DIR experiments,[17,18] discussed in section 2.5.2 of this chapter as well as chapters 3 and 4, are performed by blocking portions of the pump spectrum in the focal plane of the shaper, either manually or by manipulating the acoustic waveform applied to the shaper.

2.2.5 Phase Manipulation of the 2DIR Signal

The programmable nature of the AOM waveform additionally enables 2DIR collection techniques that take advantage of the signal's (S_{2DIR}) dependence on the relative phase relationship between the two pump pulses ($\Delta\Phi_{12} = \Phi_1 - \Phi_2$).[12] The first technique described here applies a fixed rotating frame to $\Delta\Phi_{12}$ such that $\Delta\Phi_{12} = -\omega_{RF}t_1$ where ω_{RF} is the frequency of the rotating frame. This effectively downshifts the 2DIR signal by ω_{RF} which reduces the sampling rate required to avoid aliasing in S_{2DIR}. The experiments contained in this dissertation use a rotating frame frequency of ω_{RF} = 1400 cm^{-1}. The second technique is known as phase cycling and takes advantage of the fact that a π phase shift in $\Delta\Phi_{12}$ induces a π phase shift in S_{2DIR}. This phase shift inverts the positive and negative going oscillations in the signal, while leaving contributions from noise and unwanted response pathways that do not depend on $\Delta\Phi_{12}$ unchanged. Consequently, subtraction of signals collected with a relative π phase shift to one another amplifies the underlying 2DIR signal and eliminates unwanted contributions. The

experiments used the 4-frame phase cycling procedure, summarized in table 2.2.5-1. In this procedure frames A and C have zero phase shift between the pump pulses and frames B and D have a π phase shift. 2DIR data sets are collected for each frame, and then recombined according to (A-B)+(C-D). The individual subtraction steps followed by addition results in doubling the magnitude of S_{2DIR} while suppressing unwanted signals. The resulting data sets are then recombined to give a total amplitude enhancement of $4S_{2DIR}$ compared to the individual frames.

Table 2.2.5-1: Phase of each pump pulse, relative phase shift between pump pulses, and sign of the 2DIR signal for a 4-frame phase cycling scheme.

	ϕ_1	ϕ_2	$\Delta\phi_{12}$	S_{2DIR}
A	0	0	0	$+S$
B	0	π	π	$-S$
C	π	π	0	$+S$
D	π	0	π	$-S$
$(\boldsymbol{A}-\boldsymbol{B})+(\boldsymbol{C}-\boldsymbol{D})$				$4S_{2DIR}$

2.3 Extracting Rephasing and Nonrephasing Signals

The rephasing and nonrephasing 2DIR signals can be extracted from data collected with the 4-frame phase cycling scheme and experimental geometry discussed in the previous sections.[19] Matlab code for generating the rephasing and nonrephasing spectra can be found in appendix B. Figure 2.3-1 provides a visual summary of the

procedure for obtaining the rephasing and nonrephasing spectra. In figure 2.3-1, $S(t_1, t_2, \omega_3)$ gives the experimentally collected spectrum. This data set represents the purely absorptive signal which has been Fourier transformed over t_3 by a grating and recorded by a mid-IR detector. This signal is the sum of the rephasing and nonrephasing response pathways.

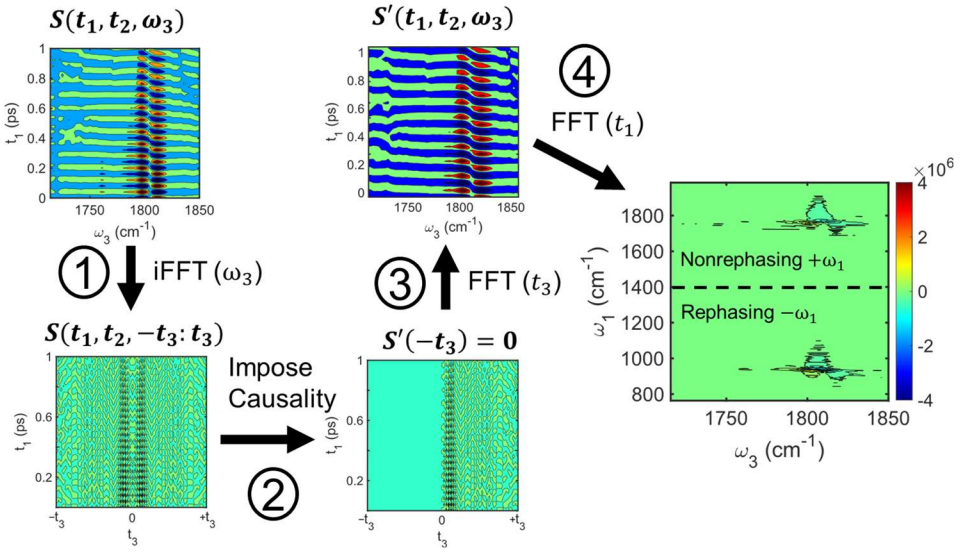

Figure 2.3-1: Workflow for separating rephasing and nonrephasing spectra from a purely absorptive 2DIR spectrum collected using a 4-frame phase cycling scheme.

Step 1 for separating the rephasing and nonrephasing signals is to perform an inverse Fourier transform to recover the fully time domain signal $S(t_1, t_2, -t_3 : t_3)$, which is complex in t_3 and centered about $t_3 = 0$. Only the real parts of the complex data sets are shown in figure 2.3-1. Step 2 imposes causality on the t_3 dimension, meaning all negative values of t_3 are set to zero. This produces a causal data set denoted as $S'(t_1, t_2, -t_3 = 0)$, which is then Fourier transformed back into the ω_3 domain during step 3. Step 4 is identical to

the procedure for obtaining the purely absorptive spectrum from the experimental data. It involves taking the real part of the Fourier transform over t_1. When this is performed for the causal data set, the rephasing and nonrephasing spectra appear symmetrically about $\omega_1 = \omega_{RF}$. The nonrephasing spectrum is found in the $\omega_{RF} + \omega_1$ region of the spectrum, while the rephasing spectrum appears inverted in the $\omega_{RF} - \omega_1$ half of the spectrum.

The success of this data processing routine is demonstrated in figure 2.3-2, where time-dependent peak amplitudes, referred to as kinetic traces, for a diagonal bleach peak are compared between the experimentally collected “raw” purely absorptive spectrum and a purely absorptive spectrum reconstructed by summing the rephasing and nonrephasing signals. On the left of figure 2.3-2 is an experimental 2DIR spectrum of the carbonyl stretching region of ethylene carbonate dissolved in THF. The spectrum in the middle of figure 2.3-2 is reconstructed by summing the rephasing and nonrephasing spectra obtained by enforcing causality in the time domain data.

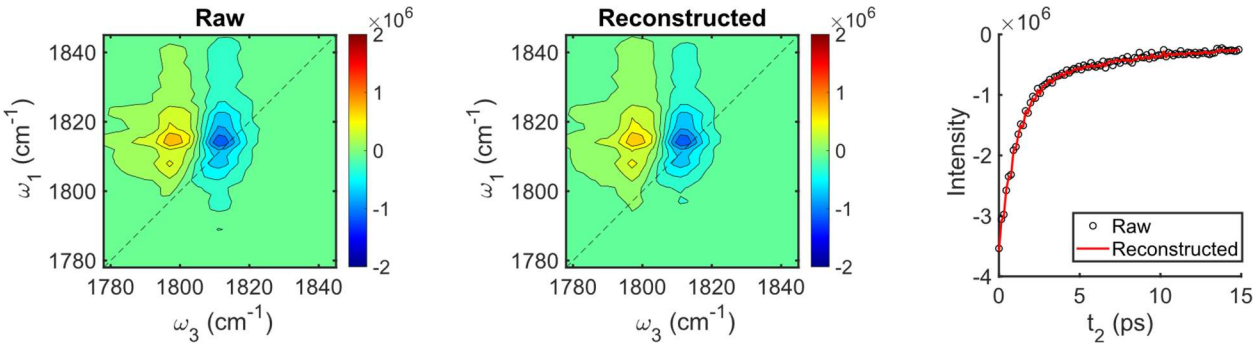

Figure 2.3-2: Comparing the kinetic traces taken from raw and reconstructed purely absorptive spectra for a sample of ethylene carbonate dissolved in THF. The kinetic traces of the most intense region of the diagonal bleach are shown on the right for both raw (black, dotted) and reconstructed (red, solid) data sets.

The two spectra are qualitatively quite similar, although the reconstructed spectra do not perfectly emulate the raw data. This is likely due to the additional digitized Fourier transforms required to make the causal data set. However, a comparison of the peak amplitude decay between the two spectra shows that the information on vibrational dynamics is almost exactly retained. Kinetic traces taken from the most intense point on the diagonal bleach peak of both spectra are plotted on the right of figure 2.3-2. The raw (black, dotted) and reconstructed (red, solid) traces are nearly identical, demonstrating the reliability of the method described above.

2.4 2DIR of Coupled Oscillators

One advantage of 2DIR spectroscopy over lower dimensional techniques is the ability to resolve response pathways in which the initial and final light matter interactions involve different vibrational modes and therefor appear as off diagonal cross peaks in the 2DIR spectrum. Such pathways may report on anharmonic couplings between different oscillators,[20–23] vibrational energy transfer pathways,[24–27] or chemical exchange.[28,29] Often, the molecular response embeds information on all three phenomena in the same

2DIR spectrum. Isolating the contributions of different pathways thus requires carefully accounting for the underlying response pathways contributing to each peak in a 2DIR spectrum. Consider a simple system of two anharmonically coupled vibrational modes, denoted by $|\alpha\rangle$ and $|\beta\rangle$. A cartoon 2DIR spectrum for such system is given in figure 2.4-1. As with the spectrum given for a single anharmonic oscillator shown in figure 2.1-1, blue peaks correspond to pathways in which the interaction between the chemical system and E_3 leads to loss of absorption, while red peaks correspond to excited state absorption pathways. Orange peaks in figure 2.4-1 also correspond to excited state absorption pathways but arise due to either chemical exchange or vibrational energy transfer processes during the t_2 interval. Additionally figure 2.4-1 gives Feynman diagrams whose excitation frequency corresponds to the fundamental transition of $|\alpha\rangle$. The diagrams for the diagonal peaks which were given in figure 2.1-1 are omitted.

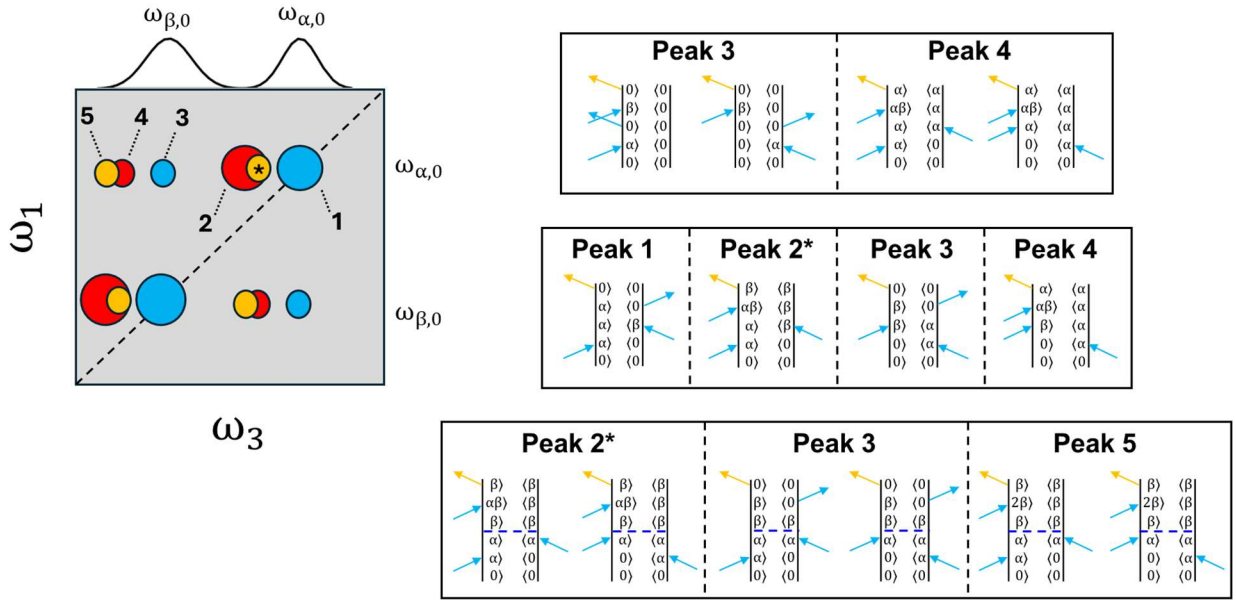

Figure 2.4-1. **Left.** Cartoon depiction for a 2DIR spectrum of a pair of coupled oscillators. **Right.** Sets of Feynman diagrams contributing to peaks in the top row of the 2DIR spectrum presented on the left. Population transfer is indicated by a blue dashed line in the Feynman diagrams.

The Feynman diagrams listed in figure 2.4-1 have been further organized by their behavior during the t_2 waiting period. The first set of Feynman diagrams given in figure 2.4-1 correspond to cross peaks for ground state bleach (peak 3) or excited state absorption (peak 4) pathways. Compared to the diagonal peak pair of a single oscillator, they do not encode any unique information with respect to the t_2 dynamics of the system. However, the final light matter interaction of peak 4 promotes one side of the density matrix to the combination band $|\alpha\beta\rangle$, and its ω_3 position reports on the strength of the coupling between $|\alpha\rangle$ and $|\beta\rangle$. The other pathways contain additional information with respect to vibrational relaxation processes.

The second set of Feynman diagrams correspond to quantum beating (QB) response pathways. Unlike the previously described response pathways which occupy a population state during the waiting period, QB pathways represent fully coherent pathways and their t_2 evolution directly reports on the coherence between the two coupled oscillators. As such, QB pathways cause peak intensities to oscillate along t_2 at the frequency difference of the two vibrational modes which make up the coherent superposition. Note that QB pathways do not exclusively contribute to cross peaks in the 2DIR spectrum. Nonrephasing QB pathways directly contribute to the diagonal bleach labeled as peak 1. Nonrephasing QB pathways also impact the diagonal excited state absorption peaks, although their center frequency is shifted on ω_3. This shift occurs because they occupy a coherence involving a combination band during t_3, rather than an overtone. As such, the absorptive nonrephasing QB pathway is labeled as contributing to peak 2*, where the asterisk indicates that the peak is slightly shifted from the true center

of peak 2. QB contributions to cross peaks arise from the rephasing diagrams, at least in the secular approximation. This is an idea we will revisit shortly.

The final set of pathways listed in figure 2.4-1 corresponds to the exchange of vibrational populations. This can arise due to chemical exchange, in the case where $|\alpha\rangle$ and $|\beta\rangle$ correspond to two distinct conformations of the same chemical system. Exchange pathways can also arise due to vibrational energy transfer processes, which are the focus of this dissertation. These pathways reflect the dissipation of vibrational energy between the vibrational populations of chemical systems. This transfer process is marked by a blue dashed line in the corresponding Feynman diagrams.

2.4.1 The Feynman Diagram Representation of Coherent Relaxation

The predicted effects of coherent relaxation processes on different features in a 2DIR spectrum can be described by including the nonsecular processes described in chapter 1, such as coherence transfer, into the Feynman diagram representation of 2DIR response pathways.[17,30–33] Coherent relaxation processes are denoted by a red dashed line in the Feynman diagrams shown in figure 2.4.1-1. The furthest diagram to the left shows a secular quantum beating pathway, while the diagrams to the right contain an additional nonsecular coherent relaxation process occurring over the t_1, t_2, and t_3 time intervals, respectively. The cartoon 2DIR spectra shown beneath each diagram will be used to describe how the Feynman diagram representation aids in the interpretation of coherent relaxation processes.

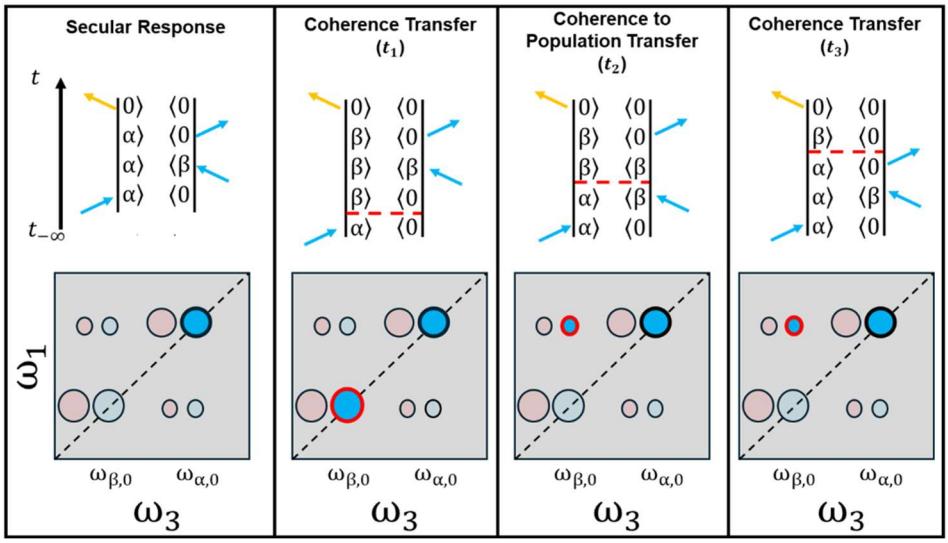

Figure 2.4.1-1. Example of incorporating nonsecular relaxation in double sided Feynman diagrams. (Top left to right) Feynman diagrams for a secular quantum beating pathway, and the same pathway with a coherent relaxation process (red dashed line) occurring during the t_1, t_2, and t_3 time intervals. (Bottom) Cartoon 2DIR spectra which show the peaks that receive amplitude for the secular (brighter blue) and nonsecular (red outline) pathways.

The brightly colored peaks in the cartoon 2DIR spectra shown beneath each diagram indicate the peaks that receive amplitude from both the coherent relaxation processes (red outline) and the secular quantum beating pathway (black outline).

In the example of the secular quantum beating pathway, the first and third light-matter interaction both generate an $|\alpha\rangle\langle 0|$ coherence state, causing the pathway to contribute to a diagonal peak located at $\omega_{\alpha,0}$ on both axes. However, the inclusion of coherence transfer or coherence to population transfer leads to new pathways which contribute to other peaks in the 2DIR spectrum. For the t_1 coherence transfer process, the initially excited $|\alpha\rangle\langle 0|$ state partially decays into the state $|\beta\rangle\langle 0|$ before the arrival of the second pulse. This causes the new pathway to appear at $\omega_1 = \omega_{\beta,0}$ in the spectrum, while retaining the amplitude of the light-matter interaction between the first pulse and the

transition dipole moment of $|\alpha\rangle$.[17] The second pulse in the coherent pathway generates a population state $|\beta\rangle\langle\beta|$ whose initial amplitude now depends on the transition dipole moment strength of $|\alpha\rangle$ and the coherence transfer rate. The third pulse generates the state $|\beta\rangle\langle 0|$, causing the coherent pathway to contribute to the diagonal peak at $\omega_{\beta,0}$ on both axes. Similar reasoning can be used to predict the effects of the t_2 and t_3 coherent relaxation processes shown in figure 2.4.1-1. In both of those diagrams, the coherent relaxation process causes the beating of the $|\alpha\rangle\langle\beta|$ multi-level coherence to appear on cross peaks, instead of on the diagonal peaks, as expected for nonrephasing pathways.[31,34] Compared to descriptions of 2DIR that invoke the secular approximation, coherent relaxation pathways mix both the transition dipole moment strengths and t_2 relaxation processes (population transfer, population relaxation, and multilevel coherence decay) that contribute to peaks in 2DIR spectra. For this reason, great care should be taken in analyzing chemical systems that display coherent relaxation mechanisms.

2.5 Studying Dynamics with 2DIR

The ability of 2DIR to report on chemical dynamics predominantly comes from the ability to study the evolution of peak shapes and peak amplitudes as a function of the t_2 waiting time. Methods for analyzing the t_2 evolution of 2DIR line shapes and peak amplitudes peaks are presented in the first parts of this section. The use of pump-selective 2DIR experiments to study t_1 coherence transfer processes is described in the third section.

2.5.1 Spectral Diffusion

The line shapes of vibrational spectra of molecules in solution are determined by two mechanisms.[11] The first mechanism, inhomogeneous broadening, arises from the static distribution of transition frequencies in an ensemble of oscillators individually coupled to a local environment. Inhomogeneous broadening reflects the heterogeneity of solvent-solute microstates in solutions. The second mechanism, homogeneous broadening, describes changes in transition frequencies whose cumulative effects average out across the entire ensemble. Homogeneous broadening is linked to processes such as the pure dephasing of individual oscillators,[11] vibrational relaxation,[35] and solvation dynamics.[11,36,37] For an inhomogenously broadened system, this dynamic sampling of different microstates leads to time-dependent changes in the spectral line shape, a process known as spectral diffusion. A schematic representation of spectral diffusion for an ensemble of oscillators is given in figure 2.5.1-1.

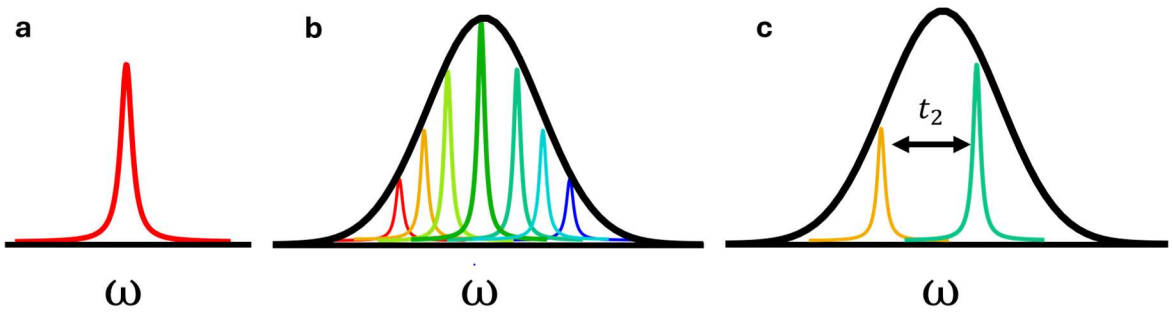

Figure 2.5.1-1 **(a)** Spectrum of a single oscillator homogeneously broadened via pure dephasing, representing a singular microstate. **(b)** Spectrum of an ensemble of homogenously broadened oscillators whose center frequencies and homogenous linewidths are determined by their local environments. **(c)** Depiction of spectral diffusion, as measured in 2DIR. In this representation, the oscillators in individual states sample other microstates over t_2.

Figure 2.5.1-1**a** shows a spectrum corresponding to an oscillator in a single local environment. The width of the peak in the frequency domain is inversely proportional to the dephasing rate of the coherence for that microstate. The spectrum of the ensemble, shown in figure 2.5.1-1**b,** consists of the sum of many homogenously broadened spectra, producing an inhomogenously broadened distribution. The spectral width of the ensemble response characterizes the differences in energy among the different microstates in the system. As the system samples other microstates, individual oscillators "swap" local environments, leading to spectral diffusion. The swapping of two individual oscillators is shown in figure 2.5.1-1**c** as a function of the waiting time t_2.

The rate of spectral diffusion for diagonal peaks in 2DIR spectra approximates the frequency-frequency correlation function (FFCF) for an ensemble of oscillators. The FFCF measures the correlation in the center frequency of the t_1 and t_3 coherences generated by the first and third pulses of a 2DIR experiment, respectively. At the earliest waiting times, individual oscillators are "frozen" in their local environments, the two coherence periods remain highly correlated, and the FFCF is maximized. At increasing waiting times, the individual oscillators sample different local environments, leading to a loss of correlation between the t_1 and t_3 coherence states. The rate of decay for the FFCF can be linked to different mechanisms of homogeneous broadening in chemical systems,[38,39] such as the fluctuations of hydrogen bonds in liquid water.[40]

One method for approximating the FFCF from the spectral diffusion of congested or otherwise complex 2DIR spectra is by comparing the relative intensities of the rephasing and nonrephasing intensities of diagonal peaks. The characteristic photon echo of rephasing signals, shown previously in figure 2.1-3, arises due to the equal but

opposite phase accumulation of the inhomogenously broadened t_1 and t_3 coherence states.[11] The photon echo increases the amplitude of the rephasing signal at early values of t_2. As the system evolves over t_2, homogeneous broadening suppresses the formation of the photon echo, causing the rephasing and nonrephasing signals to equalize in amplitude. The relative intensities of the rephasing and nonrephasing signals can be compared using the inhomogeneity index (II),[37,41] defined as

(2-3) $$II(t_2) = \frac{A_R(t_2) - A_{NR}(t_2)}{A_R(t_2) + A_{NR}(t_2)}.$$

Here, A_R and A_{NR} give the integrated intensity of the absolute value of the rephasing and non-rephasing spectra for a specific peak in the 2DIR spectrum. The inhomogeneity index can then be related to the normalized FFCF through the equation

(2-4) $$\bar{C}(t_2) = sin\left(\frac{\pi}{2}\, x\, II\right)$$

where $\bar{C}(t_2)$ is the normalized FFCF.

2.5.2 Time Dependent Peak Amplitudes

The change in 2DIR peak amplitudes during the t_2 waiting period reflects the sum of the dynamical processes of each response pathway contributing to that peak. Those processes include population relaxation, population transfer, coherence dephasing, and multi-level coherence transfer. These processes can be observed by integrating or averaging each 2DIR peak over a range of frequencies in the ω_1 and ω_3 directions and plotting the intensity as a function of t_2. The intensity vs. t_2 plot is referred to as a kinetic trace. Analysis of the kinetic trace can be used to quantify the rates of coherence dephasing for QB pathways, population relaxation for diagonal peaks, and population

transfer rates for 2DIR cross peaks. At present, there is no established method to extract information on nonsecular rate constants directly from the 2DIR spectra, and analysis of nonsecular processes focuses on identifying pathways rather than quantifying relaxation rates. The methods used to quantify population relaxation in diagonal peaks and coherence dephasing from cross peaks are described in the following section. Additionally, methods for identifying coherent relaxation pathways from Fourier analysis of kinetic traces for diagonal and cross peaks in the 2DIR spectrum are reviewed.

Diagonal Kinetic Trace

We begin our description of time-dependent peak amplitudes by analyzing the kinetic trace for the diagonal bleach of the carbonyl fundamental of ethylene carbonate-$^{13}C_3$ (^{3}EC) dissolved in tetrahydrofuran (THF). The 2DIR spectrum is given in figure 2.5.2-1**a**, where the red circle indicates the region of integration. For this peak, we expect the t_2 peak amplitude to reflect contributions from both carbonyl population relaxation and the decoherence of nonrephasing quantum beating pathways. The contributions of QB pathways can be seen in the corresponding kinetic trace of figure 2.5.2-1**b**, where we observe strong oscillations at early waiting times due to quantum beating, as well as a decay corresponding to the population relaxation.

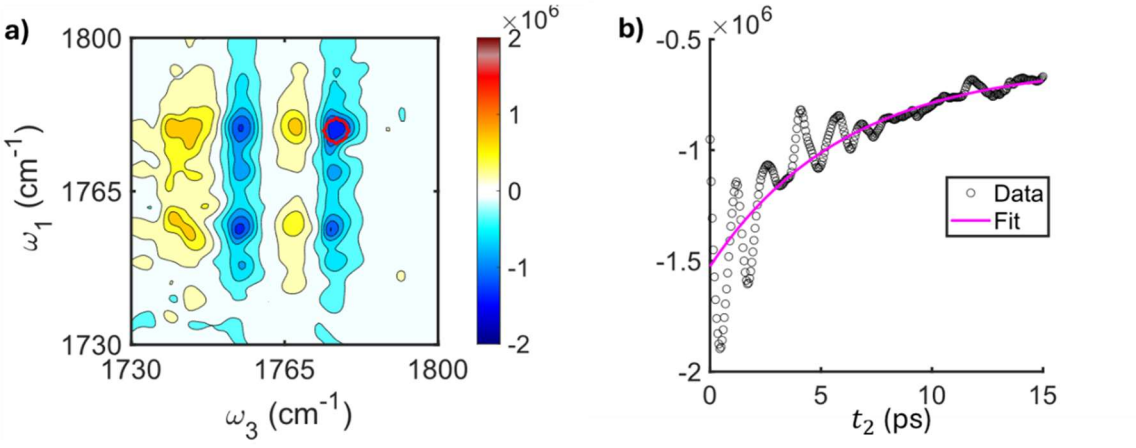

Figure 2.5.2-1: **(a)** 2DIR spectrum of the carbonyl stretching region of ^{3}EC dissolved in THF taken at t_2 = 5 ps. The red circular region indicates the integration region of the kinetic trace. **(b)** The kinetic trace (black, dotted) and corresponding exponential fit (magenta) of the region indicated in **a**.

To extract the time constant of the population relaxation, the kinetic trace is first fit to a mono-exponential decay of the form $ae^{\frac{-t_2}{T_1}} + C$, where T_1 reports on the vibrational lifetime of the carbonyl stretch. Measurements of T_1 give information on the overall strength of the coupling between the carbonyl stretch to other vibrational degrees of freedom in both ethylene carbonate and the solvent.[42–44] This fit, given as a solid magenta line in figure 2.5.2-1**b**, returns a value of T_1 = 6.59 ± 0.07 ps.

Diagonal peaks are expected to report on the decoherence of multiple t_2 coherence states due to the contributions of nonrephasing QB pathways. The additional modes involved in the multi-level coherences can be identified by taking the Fourier transform of the diagonal kinetic trace shown in figure 2.5.2-1**b,** or the residual in which the exponential component has been subtracted from the kinetic trace. An example for the latter method is given in figure 2.5.2-2.

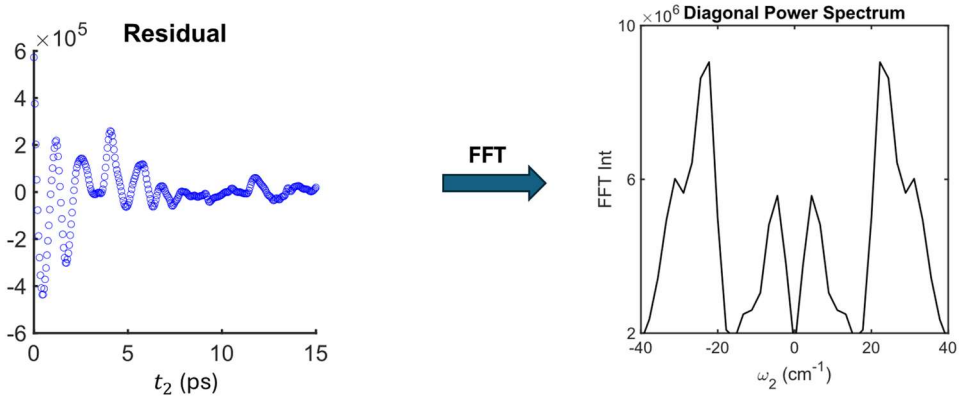

Figure 2.5.2-2. **Left**. Residual of the diagonal trace after subtracting the exponential fit to the kinetic trace shown in figure 2.5.2-1**b**. **Right**. Power spectrum generated by taking the fast Fourier transform of the residual kinetic trace for the diagonal bleach.

The multiple peaks in the power spectrum on the right side of figure 2.5.2-2 can be attributed to vibrational modes which couple to the carbonyl stretch and whose frequency separation from the carbonyl mode corresponds to the peak positions on the ω_2 axis. The peaks observed in the power spectrum of figure 2.5.2-2 indicate that the carbonyl mode couples to additional modes whose frequencies appear at $\pm$ 22 cm^{-1} and $\pm$ 31 cm^{-1} relative to the frequency of the carbonyl fundamental. The lower frequency peak appearing at 5.5 cm^{-1} cannot be unambiguously interpreted. Low frequency features in power spectra are highly sensitive to the subtraction of the exponential component and may appear as artefacts of the fitting procedure.

As multiple QB pathways contribute to the diagonal peaks, it can be difficult to isolate the decoherence rate for any individual peak from the diagonal power spectrum. Additionally, Fourier analysis is quite sensitive to interference due to spectral congestion and incomplete fits to the population dynamics can introduce low frequency peaks in the

power spectrum. As such, analysis of specific decoherence terms can be simplified for highly coupled systems by analyzing cross peaks instead.

Cross Peak Kinetic Trace

In this section we outline a procedure for assessing coherence dephasing from 2DIR cross peaks. Figure 2.5.2-3**a** shows the same 2DIR spectrum as figure 2.5.2-1**a**, only with the region of interest moved to a cross peak bleach.

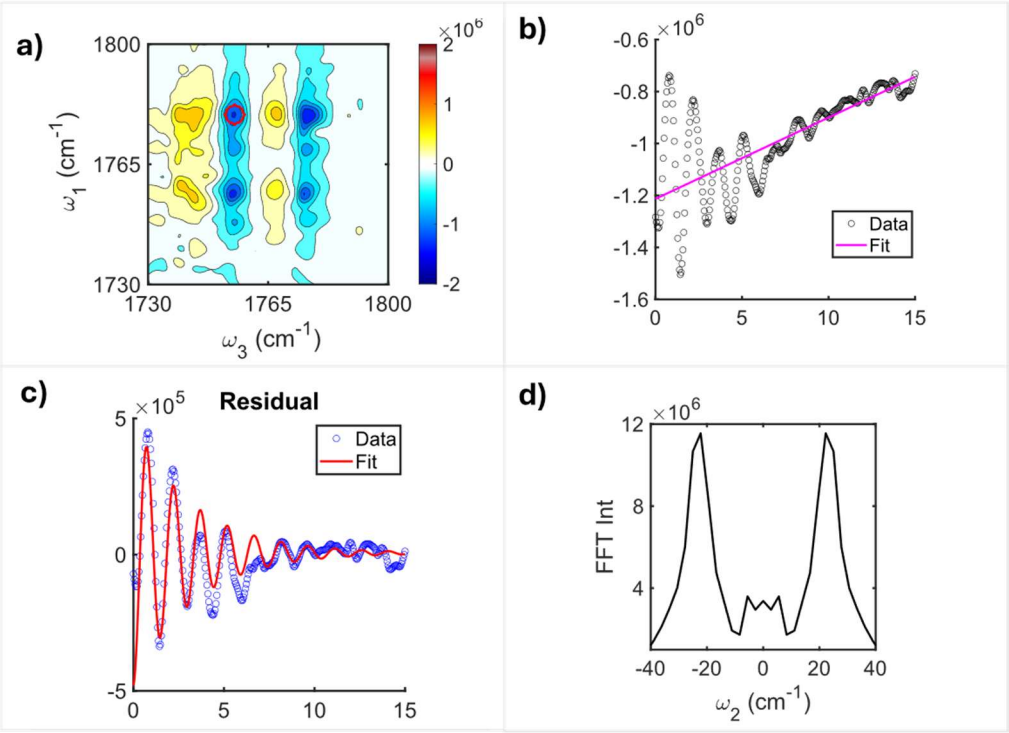

Figure 2.5.2-3. Analysis of intraband coherence dephasing for a 2DIR cross peak. **(a)** Same 2DIR spectrum shown in figure 2.5.2-1**a**, with the region of integration on a cross peak. **(b)** Cross peak kinetic trace and single exponential fit. **(c)** Residual trace fit to a damped exponential. **(d)** The power spectrum of the residual trace for the cross peak bleach.

The oscillatory component of 2DIR cross peaks reports on a single rephasing QB pathway, and the decoherence rate can be measured from the decay of the residual. The population transfer rate is not directly measured in the work contained in this dissertation

due to overlap with coherent relaxation pathways. To measure the decay of the intraband coherence contributing to the cross peak kinetic trace, the kinetic trace is again fit to a relaxation term (2.5.2-3**b**)**,** and the residual is obtained by subtracting the fit. The residual, shown as a blue scatter plot in figure 2.5.2-3**c**, is then fit to the damped exponential $ae^{\frac{-t_2}{T_d}}\cos(2\pi\omega \cdot t_2 + d)$. Here T_d gives the damping rate, ω gives the frequency of the oscillation, and d is a phenomenological phase offset. The damping rate approximates the dephasing time of the coherence, which in this case corresponds to 3.2 ps. The decoherence time can be similarly assessed by fitting the decay of the envelope or absolute values of the residual. The assumption that only a single oscillation contributes to the cross peak kinetic trace is checked in the power spectrum in figure 2.5.2-3**d.** Under the secular approximation only a single frequency component should appear in the power spectrum, which is largely what is observed. The power spectrum shows a single strong peak at 22 cm^{-1}, which corresponds to the frequency separation of the ω_1 and ω_3 positions of the cross peak.

Pump Selective 2DIR

One method for checking for t_1 coherence transfer pathways is the use of pump selective 2DIR experiments. In a pump-selective experiment, the resonance bandwidth of the first two excitation pulses is limited so that certain vibrational transitions cannot be directly excited by the first two pulses.[8,17] Consequently, no molecular response pathways should contribute to the unpumped region of the 2DIR spectrum, and no QB pathways involving unpumped vibrations should contribute to kinetic traces of peaks in the 2DIR spectrum. However, t_1 coherence transfer pathways, such as those discussed in section

2.4.1, may still lead to the observation of peaks in the unpumped region of a 2DIR spectrum.

An example of pump selective experiments for ^{3}EC is given in figure 2.5.2-4. In the experiment in figure 2.5.2-4**a**, the higher frequency carbonyl fundamental lies within the pump bandwidth, while lower frequency transitions are blocked. Figure 2.5.2-4**b** shows the opposite scenario, in which the carbonyl fundamental is no longer resonant with the pump transition.

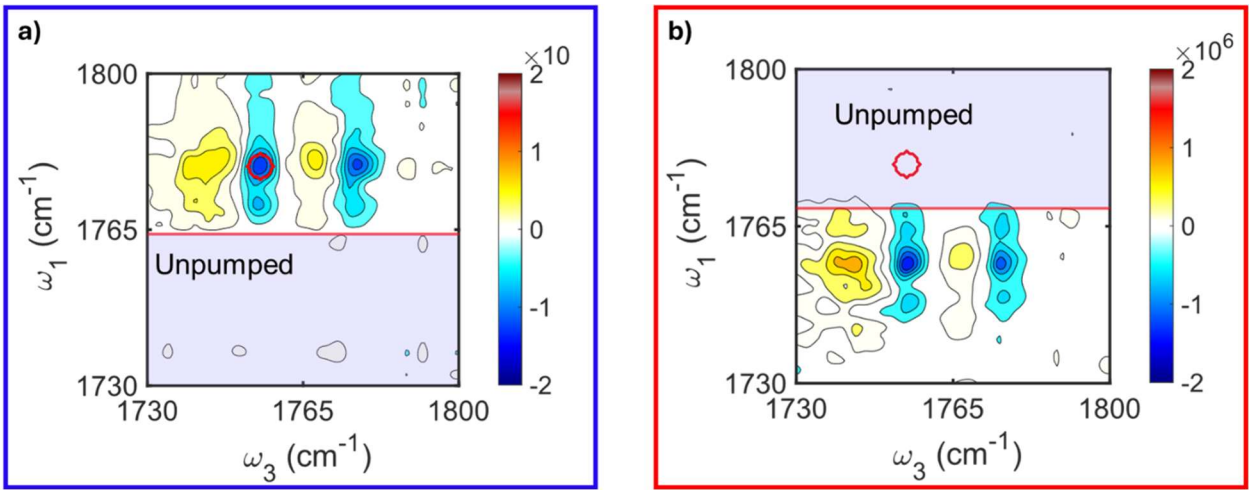

Figure 2.5.2-4. Pump selective 2DIR spectra of the carbonyl region of ^{3}EC. Unpumped regions of the 2DIR spectra are shaded in a bluish grey color. The separation between the pumped and unpumped regions is marked by a red horizontal line. Red circles indicate the integration regions for the kinetic traces shown in figure 2.5.2-5. **(a)** Pump selective experiment in which the transitions with lower frequencies than the carbonyl fundamental are blocked. **(b)** Pump selective spectra in which high frequency transitions, including the carbonyl fundamental, are blocked.

To see the effects of utilizing pump selective experiments, we can compare the kinetic traces of the cross peak, indicated by red circles in figure 2.5.2-4, to the noise of the experiment under different excitation bandwidths. For the fully pumped spectrum (not shown), it is expected that both quantum beating and vibrational population transfer

contribute to the cross peak kinetic trace. When the low frequency side of the pump pulse is blocked (2.5.2-4**a**), quantum beating contributions are expected to be suppressed. Finally, no significant intensity should be observed in the kinetic trace when the high frequency side of the pump bandwidth is blocked (2.5.2-4**b**). The pixel noise is obtained by averaging the magnitude of the 2DIR signal in a region of the spectrum outside the bandwidth of all three pulses. The results of analysis for the three experimental conditions are shown in figure 2.5.2-5.

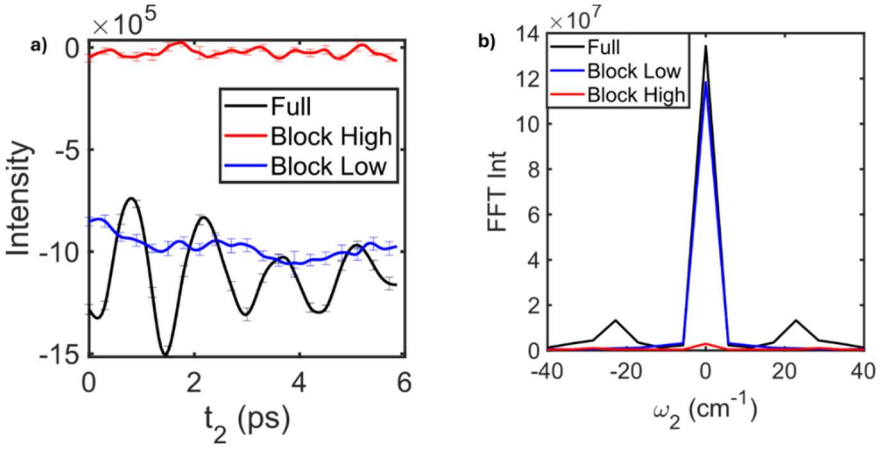

Figure 2.5.2-5. Comparing cross peak t_2 dynamics for full (black) and pump selective (blue, red) 2DIR experiments**.** Pump selective 2DIR spectra are shown in 2.5.2-4. **(a)** Kinetic traces for the cross peak bleach of each experiment plotted to 6 ps. Error bars give the pixel noise of the experiment **(b)** Power spectra of the raw kinetic trace for each experiment.

The kinetic trace for the fully pumped experiment is plotted in black while the pump-selective experiments are colored in blue for the “block low” spectrum (2.5.2-4**a)** and red for the “block high” experiment (2.5.2-4**b)**. The fully pumped kinetic trace shows strong quantum beating contributions, whose frequency component appears near 23 cm^{-1} in the power spectrum plotted in figure 2.5.2-5**b**. The “block low” experiment shows similar population dynamics, but no oscillations are observed in the kinetic trace or

corresponding power spectrum. This indicates a suppression of the quantum beating pathways. Finally, the “block high” experiment yields a kinetic trace with intensity comparable to the noise of the experiment. This indicates that no t_1 coherence transfer pathway contributes significantly to the amplitude of the cross peak. If the intensity of the kinetic trace for the unpumped cross peak was greater than the noise, as will be shown for a similar system in chapters 3 and 4, it would be interpreted as an indication of coherence transfer occurring in the system.

2.6 Summary and Implementation

In this chapter, we provide an overview of 2DIR and review the theoretical and experimental tools used to study coherent vibrational relaxation in chapters 3 and 4. Feynman diagrams provide a compact theoretical tool for predicting how both coherent and incoherent relaxation processes manifest in 2DIR spectra under different experimental conditions. This representation informs the use of both pump selective 2DIR experiments and Fourier analysis of t_2 peak amplitude oscillations for rephasing, nonrephasing, and purely absorptive 2DIR signals to identify signatures of coherent relaxation in EC and its ^{13}C isotopologues. Additionally, methods for analyzing timescales of spectral diffusion, multilevel coherence dephasing, and vibrational population relaxation from 2DIR spectra are also reviewed in this chapter. The study presented in chapter 3 details the identification of coherent relaxation processes in EC and discusses those processes’ impact on 2DIR dynamic observables. Analysis of population relaxation timescales is used in chapter 4 to determine the extent to which a manifold of dark states contributes to the redistribution of vibrational energy across the EC isotopic series. The direct or indirect nature of population relaxation dynamics is then compared to the

spectroscopic signatures of coherent relaxation across the isotopic series, granting deeper insights into the molecular properties which drive coherent vibrational relaxation.

References

(1) Galle Kankanamge, S. R.; Kuroda, D. G. Molecular Structure, Chemical Exchange, and Conductivity Mechanism of High Concentration LiTFSI Electrolytes. *J. Phys. Chem. B* **2020**, *124* (10), 1965–1977. https://doi.org/10.1021/acs.jpcb.9b10795.

(2) Fulfer, K. D.; Kuroda, D. G. Solvation Structure and Dynamics of the Lithium Ion in Organic Carbonate-Based Electrolytes: A Time-Dependent Infrared Spectroscopy Study. *J. Phys. Chem. C* **2016**, *120* (42), 24011–24022. https://doi.org/10.1021/acs.jpcc.6b08607.

(3) Fulfer, K. D.; Kuroda, D. G. A Comparison of the Solvation Structure and Dynamics of the Lithium Ion in Linear Organic Carbonates with Different Alkyl Chain Lengths. *Phys. Chem. Chem. Phys.* **2017**, *19* (36), 25140–25150. https://doi.org/10.1039/C7CP05096H.

(4) Liang, C.; Kwak, K.; Cho, M. Revealing the Solvation Structure and Dynamics of Carbonate Electrolytes in Lithium-Ion Batteries by Two-Dimensional Infrared Spectrum Modeling. *J. Phys. Chem. Lett.* **2017**, *8* (23), 5779–5784. https://doi.org/10.1021/acs.jpclett.7b02623.

(5) Lim, C.; Kim, J. H.; Chae, Y.; Lee, K.-K.; Kwak, K.; Cho, M. Solvation Structure around Li+ Ions in Organic Carbonate Electrolytes: Spacer-Free Thin Cell IR Spectroscopy. *Anal. Chem.* **2021**, *93* (37), 12594–12601. https://doi.org/10.1021/acs.analchem.1c02127.

(6) Zhang, X.; Kuroda, D. G. An Ab Initio Molecular Dynamics Study of the Solvation Structure and Ultrafast Dynamics of Lithium Salts in Organic Carbonates: A Comparison between Linear and Cyclic Carbonates. *The Journal of Chemical Physics* **2019**, *150* (18), 184501. https://doi.org/10.1063/1.5088820.

(7) Jiang, B.; Ponnuchamy, V.; Shen, Y.; Yang, X.; Yuan, K.; Vetere, V.; Mossa, S.; Skarmoutsos, I.; Zhang, Y.; Zheng, J. The Anion Effect on Li+ Ion Coordination Structure in Ethylene Carbonate Solutions. *J. Phys. Chem. Lett.* **2016**, *7* (18), 3554–3559. https://doi.org/10.1021/acs.jpclett.6b01664.

(8) Guerrieri, L.; Hall, S.; Luther, B. M.; Krummel, A. T. Signatures of Coherent Vibrational Dynamics in Ethylene Carbonate. *The Journal of Chemical Physics* **2024**, *161* (16), 164504. https://doi.org/10.1063/5.0216515.

(9) Hamm, P.; Zanni, M. *Concepts and Methods of 2D Infrared Spectroscopy*; Cambridge University Press: Cambridge, 2011. https://doi.org/10.1017/CBO9780511675935.

(10) Sung, J.; Silbey, R. J. Four Wave Mixing Spectroscopy for a Multilevel System. *The Journal of Chemical Physics* **2001**, *115* (20), 9266–9287. https://doi.org/10.1063/1.1413979.

(11) Mukamel, S. *Principles of Nonlinear Optical Spectroscopy*; Oxford Series in Optical and Imaging Sciences; Oxford University Press: Oxford, New York, 1999.

(12) Shim, S.-H.; Zanni, M. T. How to Turn Your Pump–Probe Instrument into a Multidimensional Spectrometer: 2D IR and Vis Spectroscopiesvia Pulse Shaping. *Phys. Chem. Chem. Phys.* **2009**, *11* (5), 748–761. https://doi.org/10.1039/B813817F.

(13) Luther, B. M.; Tracy, K. M.; Gerrity, M.; Brown, S.; Krummel, A. T. 2D IR Spectroscopy at 100 kHz Utilizing a Mid-IR OPCPA Laser Source. *Opt. Express, OE* **2016**, *24* (4), 4117–4127. https://doi.org/10.1364/OE.24.004117.

(14) Christopher Thomas Kuhs. INVESTIGATING MOLECULAR INTERACTIONS CONTRIBUTING TO SELF-ASSEMBLY ON ULTRAFAST TIME SCALES WITH TWO-DIMENSIONAL INFRARED SPECTROSCOPY. PhD, Colorado State University, Fort Collins, Colorado, 2019. https://api.mountainscholar.org/server/api/core/bitstreams/8d0262fb-33f6-4048-a1f5-4a01a2e4c705/content.

(15) Feng, Y.; Vinogradov, I.; Ge, N.-H. General Noise Suppression Scheme with Reference Detection in Heterodyne Nonlinear Spectroscopy. *Opt. Express, OE* **2017**, *25* (21), 26262–26279. https://doi.org/10.1364/OE.25.026262.

(16) Feng, Y.; Vinogradov, I.; Ge, N.-H. Optimized Noise Reduction Scheme for Heterodyne Spectroscopy Using Array Detectors. *Opt. Express, OE* **2019**, *27* (15), 20323–20346. https://doi.org/10.1364/OE.27.020323.

(17) Marroux, H. J. B.; Orr-Ewing, A. J. Distinguishing Population and Coherence Transfer Pathways in a Metal Dicarbonyl Complex Using Pulse-Shaped Two-Dimensional Infrared Spectroscopy. *J. Phys. Chem. B* **2016**, *120* (17), 4125–4130. https://doi.org/10.1021/acs.jpcb.6b02979.

(18) Nishida, J.; Tamimi, A.; Fei, H.; Pullen, S.; Ott, S.; Cohen, S. M.; Fayer, M. D. Structural Dynamics inside a Functionalized Metal–Organic Framework Probed by Ultrafast 2D IR Spectroscopy. *Proc Natl Acad Sci U S A* **2014**, *111* (52), 18442–18447. https://doi.org/10.1073/pnas.1422194112.

(19) Zhang, Z.; Wells, K. L.; Hyland, E. W. J.; Tan, H.-S. Phase-Cycling Schemes for Pump–Probe Beam Geometry Two-Dimensional Electronic Spectroscopy. *Chemical Physics Letters* **2012**, *550*, 156–161. https://doi.org/10.1016/j.cplett.2012.08.037.

(20) Brüggemann, J.; Wolter, M.; Jacob, C. R. Quantum-Chemical Calculation of Two-Dimensional Infrared Spectra Using Localized-Mode VSCF/VCI. *The Journal of Chemical Physics* **2022**, *157* (24), 244107. https://doi.org/10.1063/5.0135273.

(21) Donaldson, P. M.; Guo, R.; Fournier, F.; Gardner, E. M.; Barter, L. M. C.; Barnett, C. J.; Gould, I. R.; Klug, D. R.; Palmer, D. J.; Willison, K. R. Direct Identification and Decongestion of Fermi Resonances by Control of Pulse Time Ordering in Two-Dimensional IR Spectroscopy. *The Journal of Chemical Physics* **2007**, *127* (11), 114513. https://doi.org/10.1063/1.2771176.

(22) Okumura, K.; Jonas, D. M.; Tanimura, Y. Two-Dimensional Spectroscopy and Harmonically Coupled Anharmonic Oscillators. *Chemical Physics* **2001**, *266* (2), 237–250. https://doi.org/10.1016/S0301-0104(01)00252-X.

(23) Rector, K. D.; Kwok, A. S.; Ferrante, C.; Tokmakoff, A.; Rella, C. W.; Fayer, M. D. Vibrational Anharmonicity and Multilevel Vibrational Dephasing from Vibrational Echo Beats. *The Journal of Chemical Physics* **1997**, *106* (24), 10027–10036. https://doi.org/10.1063/1.474060.

(24) Park, J. Y.; Mondal, S.; Kwon, H.-J.; Sahu, P. K.; Han, H.; Kwak, K.; Cho, M. Effect of Isotope Substitution on the Fermi Resonance and Vibrational Lifetime of Unnatural Amino Acids Modified with IR Probe: A 2D-IR and Pump-Probe Study of 4-Azido-L-Phenyl Alanine. *The Journal of Chemical Physics* **2020**, *153* (16), 164309. https://doi.org/10.1063/5.0025289.

(25) Hassani, M.; Mallon, C. J.; Monzy, J. N.; Schmitz, A. J.; Brewer, S. H.; Fenlon, E. E.; Tucker, M. J. Inhibition of Vibrational Energy Flow within an Aromatic Scaffold via Heavy Atom Effect. *The Journal of Chemical Physics* **2023**, *158* (22), 224201. https://doi.org/10.1063/5.0153760.

(26) Schmitz, A. J.; Pandey, H. D.; Chalyavi, F.; Shi, T.; Fenlon, E. E.; Brewer, S. H.; Leitner, D. M.; Tucker, M. J. Tuning Molecular Vibrational Energy Flow within an

Aromatic Scaffold via Anharmonic Coupling. *J. Phys. Chem. A* **2019**, *123* (49), 10571–10581. https://doi.org/10.1021/acs.jpca.9b08010.

(27) Rubtsova, N. I.; Rubtsov, I. V. Vibrational Energy Transport in Molecules Studied by Relaxation-Assisted Two-Dimensional Infrared Spectroscopy. *Annual Review of Physical Chemistry* **2015**, *66* (Volume 66, 2015), 717–738. https://doi.org/10.1146/annurev-physchem-040214-121337.

(28) *Dynamics of Liquids, Molecules, and Proteins Measured with Ultrafast 2D IR Vibrational Echo Chemical Exchange Spectroscopy | Annual Reviews*. https://www.annualreviews.org/content/journals/10.1146/annurev-physchem-073108-112712 (accessed 2024-08-27).

(29) Dereka, B.; Lewis, N. H. C.; Zhang, Y.; Hahn, N. T.; Keim, J. H.; Snyder, S. A.; Maginn, E. J.; Tokmakoff, A. Exchange-Mediated Transport in Battery Electrolytes: Ultrafast or Ultraslow? *J. Am. Chem. Soc.* **2022**, *144* (19), 8591–8604. https://doi.org/10.1021/jacs.2c00154.

(30) Khalil, M.; Demirdöven, N.; Tokmakoff, A. Vibrational Coherence Transfer Characterized with Fourier-Transform 2D IR Spectroscopy. *The Journal of Chemical Physics* **2004**, *121* (1), 362–373. https://doi.org/10.1063/1.1756870.

(31) Nee, M. J.; Baiz, C. R.; Anna, J. M.; McCanne, R.; Kubarych, K. J. Multilevel Vibrational Coherence Transfer and Wavepacket Dynamics Probed with Multidimensional IR Spectroscopy. *The Journal of Chemical Physics* **2008**, *129* (8), 084503. https://doi.org/10.1063/1.2969900.

(32) Eckert, P. A.; Kubarych, K. J. Vibrational Coherence Transfer Illuminates Dark Modes in Models of the FeFe Hydrogenase Active Site. *The Journal of Chemical Physics* **2019**, *151* (5), 054307. https://doi.org/10.1063/1.5111016.

(33) Chuntonov, L.; Ma, J. Quantum Process Tomography Quantifies Coherence Transfer Dynamics in Vibrational Exciton. *J. Phys. Chem. B* **2013**, *117* (43), 13631–13638. https://doi.org/10.1021/jp4075493.

(34) Baiz, C. R.; Kubarych, K. J.; Geva, E. Molecular Theory and Simulation of Coherence Transfer in Metal Carbonyls and Its Signature on Multidimensional Infrared Spectra. *J. Phys. Chem. B* **2011**, *115* (18), 5322–5339. https://doi.org/10.1021/jp109357d.

(35) Rey, M. J.; Reilly, C. J.; Massari, A. M. Vibrational Heavy Atom Effect on Relaxation and Solvent Shell Dynamics in Group VIII Trimetallic Carbonyls. *The Journal of Chemical Physics* **2024**, *161* (5), 054305. https://doi.org/10.1063/5.0216474.

(36) Boeij, W. P. de; Pshenichnikov, M. S.; Wiersma, D. A. ULTRAFAST SOLVATION DYNAMICS EXPLORED BY FEMTOSECOND PHOTON ECHO SPECTROSCOPIES. *Annual Review of Physical Chemistry* **1998**, *49* (Volume 49, 1998), 99–123. https://doi.org/10.1146/annurev.physchem.49.1.99.

(37) Roberts, S. T.; Loparo, J. J.; Tokmakoff, A. Characterization of Spectral Diffusion from Two-Dimensional Line Shapes. *The Journal of Chemical Physics* **2006**, *125* (8), 084502. https://doi.org/10.1063/1.2232271.

(38) Fenn, E. E.; Fayer, M. D. Extracting 2D IR Frequency-Frequency Correlation Functions from Two Component Systems. *The Journal of Chemical Physics* **2011**, *135* (7), 074502. https://doi.org/10.1063/1.3625278.

(39) Guo, Q.; Pagano, P.; Li, Y.-L.; Kohen, A.; Cheatum, C. M. Line Shape Analysis of Two-Dimensional Infrared Spectra. *J Chem Phys* **2015**, *142* (21), 212427. https://doi.org/10.1063/1.4918350.

(40) Roberts, S. T.; Ramasesha, K.; Tokmakoff, A. Structural Rearrangements in Water Viewed Through Two-Dimensional Infrared Spectroscopy. *Acc. Chem. Res.* **2009**, *42* (9), 1239–1249. https://doi.org/10.1021/ar900088g.

(41) Duan, R.; Mastron, J. N.; Song, Y.; Kubarych, K. J. Direct Comparison of Amplitude and Geometric Measures of Spectral Inhomogeneity Using Phase-Cycled 2D-IR Spectroscopy. *The Journal of Chemical Physics* **2021**, *154* (17), 174202. https://doi.org/10.1063/5.0043961.

(42) Kocheril, P. A.; Wang, H.; Lee, D.; Naji, N.; Wei, L. Nitrile Vibrational Lifetimes as Probes of Local Electric Fields. *J. Phys. Chem. Lett.* **2024**, *15* (19), 5306–5314. https://doi.org/10.1021/acs.jpclett.4c00597.

(43) Bigwood, R.; Gruebele, M.; Leitner, D. M.; Wolynes, P. G. The Vibrational Energy Flow Transition in Organic Molecules: Theory Meets Experiment. *Proceedings of the National Academy of Sciences* **1998**, *95* (11), 5960–5964. https://doi.org/10.1073/pnas.95.11.5960.

(44) Gruebele, M.; Bigwood, R. Molecular Vibrational Energy Flow: Beyond the Golden Rule. *International Reviews in Physical Chemistry* **1998**, *17* (2), 91–145. https://doi.org/10.1080/014423598230117.

Chapter 3
Signatures of Coherent Vibrational Energy Transfer in Ethylene Carbonate[1]

3.1 Overview

Despite having practical applications in battery technology and serving as a model system for Fermi resonance coupling, ethylene carbonate (EC) receives little direct attention as a vibrational probe in nonlinear vibrational spectroscopy experiments. EC contains a Fermi resonance which is well characterized in the linear spectrum, and the environmental sensitivity of its Fermi resonance peaks could make it a good molecular probe for two-dimensional infrared spectroscopy (2DIR) experiments. As a model system, we investigate the linear and 2DIR vibrational spectrum of the carbonyl stretching region of ethylene carbonate in tetrahydrofuran (THF). The 2DIR spectrum reveals peak dynamics which evolve coherently. We characterize these dynamics in the context of Redfield theory and find evidence that EC dynamics proceed through coherent pathways, including singular coherence transfer pathways which have not been widely observed in other studies. We find that coherent contributions play a significant role in the observed dynamics of cross peaks in the 2DIR spectrum which must be accounted for to extract accurate measurements of early waiting time dynamics.

[1] Reprinted with permission from {Luke Guerrieri, Sarah Hall, Brad M. Luther, Amber T. Krummel' Signatures of coherent vibrational dynamics in ethylene carbonate. *J. Chem. Phys.* 28 October 2024; 161 (16): 164504}

3.2 Introduction

As the need for safer and more efficient energy storage devices grows, an increasing amount of research has been dedicated to understanding the underlying molecular physics dictating the function of battery technologies.[1–6] Linear and time dependent nonlinear vibrational spectroscopies have been increasingly employed as a means of studying the structure and dynamics of electrolyte solutions relevant to battery performance, with a fair amount of attention given to organic electrolytes composed of mixtures of linear and cyclic carbonates commonly found in commercial lithium-ion batteries.[1,2,4–13] Ion solvation primarily occurs through interaction with the carbonyl mode of the electrolyte components,[1,2,10,12] so it is desirable to probe the carbonyl stretching region directly. As such the carbonyl stretching regions of several organic carbonates have been used as molecular probes in 2DIR experiments to gain insight on the role of the electrolyte in device function. Ethylene carbonate (EC) is a common component of these mixtures, but time dependent vibrational studies which directly study EC are overall scarce,[13] and to our knowledge, nonexistent for the carbonyl region. One stated reason for this is due to the presence of an additional Fermi resonance band[2] in the carbonyl region which contributes to spectral congestion.

That same Fermi resonance makes EC a model compound for linear IR and Raman studies of Fermi resonance coupling.[14–18] Time dependent IR studies show that coherent excitations of Fermi doublets introduce oscillations in peak intensities which may obscure underlying population dynamics.[19–22] However, coherent oscillations in peak intensities are also a signature of coherent vibrational energy transfer (CVET).[23–26] This raises the possibility that the coherent oscillations observed in 2DIR spectra of Fermi

resonances could result from CVET pathways, in which case they reflect important elements of the system dynamics. To our knowledge there have been no time dependent vibrational studies directly investigating the extent of CVET in Fermi coupled systems. Theoretical models of coherent energy transfer often assume the coupling of coherence states is facilitated by coupling to bath coordinates. This could be of particular importance in studies of organic battery electrolytes which use carbonyl transitions of a particular solvent element as an IR probe. Moreover, the bath in the organic electrolyte cocktail is a sea of carbonates. In this case the presence of energetically similar transitions in the electrolyte and the IR probe may provide a mechanism for coherent dynamics.

To assess the viability of EC as an IR probe molecule, we set out to characterize the 2DIR spectrum of EC using tetrahydrofuran (THF) as a model solvent. THF has previously been used as a model solvent in studies of linear carbonates coordinated to lithium ions, as it has some similar dielectric properties to linear carbonates used in battery electrolytes.[4] In this system we detect clear signatures of coherent excitations and interpret them in the context of nonsecular Redfield theory.[27,28] Nonsecular Redfield theory allows for additional relaxation pathways in which coherent superpositions of system eigenstates couple to other coherences or to population states.[27,29–31] This framework has been employed[31,32] to describe long lived coherences observed in time dependent electronic spectra of photosynthetic pigments[33,34] and was recently utilized to identify vibrational energy transport to IR-inactive modes in a 2DIR study of metal carbonyl compounds.[24] The spectral signatures of nonsecular relaxation are well characterized by joint theoretical and experimental 2DIR studies,[23,26] and those signatures are easily understood by incorporating nonsecular relaxation into the well-

known Feynman diagram representation of third order response functions. In this framework coherent oscillations in peak intensities are directly related to features in the linear and 2DIR spectra. Within the context of Redfield theory, we compare the frequency positions of oscillating peaks in rephasing and non-rephasing spectra to confirm the presence of CVET. We then use pump selective experiments to characterize the CVET contributions to features in the 2DIR spectrum.

3.3 Experimental Methods

3.3.1 Sample Preparation and Linear IR

Ethylene carbonate (EC) and tetrahydrofuran (THF) were purchased from Sigma-Aldrich and Oakwood Chemical, respectively. Both were used without further purification. We stored EC in a vacuum desiccator to avoid contamination from water. Samples for linear and 2DIR experiments consisted of 50-75 mM EC dissolved in THF. The solutions were sandwiched between a pair of 1 mm calcium fluoride (CaF_2) plates (Crystran) with a diameter of 25.4 mm and a 25 μm path length determined by a Teflon spacer (Harrick). We collected linear IR measurements with a Bruker Optics Vertex 70 spectrometer set to 64 scans and a resolution of 2 cm^{-1}. Time dependent linear IR measurements indicated that the sample remained stable over a four-hour period, which served as the upper limit for collection of 2DIR data.

3.3.2 100 kHz 2DIR spectrometer

A home built OPCPA ultrafast laser system produced the 100 kHz mid-IR pulse train used in 2DIR experiments. The operating principles of the system have been described previously.[35–37] These experiments utilized mid-IR pulses centered at

1750 cm^{-1} with a FWHM of 214 cm^{-1}. A $\frac{\lambda}{2}$ waveplate and mid-IR thin film polarizer split the OPCPA output into pump and probe lines with tunable energy. Pulse energies at the sample were evenly divided between the two pump pulses and a single probe pulse, with an average of 0.1 μJ of energy per pulse.

3.3.3 2DIR Data Collection

All 2DIR measurements took place in a partly collinear heterodyned pump-probe geometry[38] using a mid-IR pulse shaper (QuickShape+, PhaseTech Spectroscopy). Descriptions of 2DIR spectroscopy in this geometry are available elsewhere[20,35,38,39] and will not be described here. For clarity, we refer to t_1 as the coherence time beginning at the interaction of the first pump pulse with the sample and terminating at the arrival of the second pump pulse. Similarly, t_2 gives the waiting time of the experiment between pulses two and three, while t_3 describes the final coherence period during which third order signal emits. Data collection utilized a 1x4 (2x2) phase cycling scheme[40] with a rotating frame of 1400 cm^{-1} and t_1 scan times ranging from 0 ps to 3 ps, 8 ps, or 10 ps. All t_1 scans consisted of 401 steps; however, we found improved signal intensity when oversampling the earlier regions of our free induction decay. As such, we utilized varying t_1 scan times to improve either t_1 resolution or signal to noise in our limited experimental window. Because we find evidence the signatures of CVET are sensitive to t_1 scan lengths, we do not directly compare the dynamics of data sets taken with different final t_1 delays. Appendix A.4 [2] explores this result in more detail by using varying window functions to simulate different t_1 scan times.

[2] Supplementary information for this chapter is provided in appendix A.

Fourier transform of the heterodyned 2DIR signal about t_3 took place on a monochromator, and the frequency resolved signal was measured using a 64-element mercury cadmium telluride (MCT) array detector at 100 kHz (Infrared Systems.) The geometry of the 64-element array and monochromator produced a spectral window spanning 1714-1849 cm^{-1} with an approximate resolution of 2.1 cm^{-1}. A mechanically controlled delay stage on the probe line yielded waiting time scans spanning either 0-6 ps or 0-15 ps. Scan times were chosen to optimize either signal to noise or the resolution of Fourier transforms over t_2. We employ a reference pixel noise reduction scheme[41,42] to limit the impact of probe noise on our spectra.

Data collection occurred in both the XXXX and XXYY polarization schemes[39,43] which were recombined to yield isotropic data sets presented in this work.[20] The free induction decay at each pixel was treated with an exponential window function for the final 2 ps of each scan, zero padded with an additional 401 steps, and normalized to the laser power. A Fourier transform along t_1 generated the excitation axis ω_1. All 2D spectra and kinetic traces presented in this work consist of the real Fourier transform of the signal. Rephasing and non-rephasing spectra were obtained according to methods outlined previously.[44] While it is more common to generate rephasing and non-rephasing signals from a 1x3 phase cycling scheme[45] we find that the purely absorptive spectrum obtained by combining the rephasing and non-rephasing signals agrees with the experimentally collected purely absorptive data.

3.3.4 Pump Selective 2DIR

We employed pump selective 2DIR experiments to assess the significance of nonsecular relaxation in our system. We take advantage of the diffraction gratings in our pulse shaper to limit pump bandwidth, in line with previous experiments.[25,40] To maintain temporal resolution, we compress our pulses for both full and pump-selective experiments, which could cause variations in the pump pulse temporal profile. However, we do not detect significant differences in the dynamics of certain peaks (see A.3) in the pump selective and full pump experiments. We take the consistency of these peak dynamics as indicating changes in the signal due to the pump temporal profile are not detectable within experimental error.

3.4 Nonsecular Relaxation in 2DIR Spectroscopy

Signatures of coherent vibrational energy transfer in 2DIR spectra are well documented[23,24,26,46] and often addressed in the context of the Redfield equation[27] which we describe briefly.

(3-1) $$\frac{\partial}{\partial t}\rho_{ab}(\mathrm{t}) = -i\omega_{ab}\rho_{ab}(\mathrm{t}) - \sum_{cd}\Gamma_{abcd}\rho_{cd}$$

Here ρ_{ab} is a given density matrix element, ω_{ab} corresponds to the frequency of ρ_{ab}, and Γ_{abcd} is an element of the relaxation tensor which encodes information on the exchange of amplitude between ρ_{ab} and ρ_{cd}. Equation 1 results from a second order perturbative treatment which assumes weak system-bath coupling.[27,47–51] The secular approximation to Redfield theory assumes dynamical independence of the off-diagonal coherence (ρ_{ab}) elements of the density matrix. In other words, coherence states do not exchange amplitude with other elements in the absence of an external force (such as a laser pulse).

This leaves only the relaxation terms Γ_{aaaa}, Γ_{aabb}, and Γ_{abab} which describe population relaxation, population transfer, and coherence dephasing, respectively. When incorporated into third order response theory, the secular approximation greatly reduces both the number of response pathways considered and the computational complexity of chemical dynamics simulations used to interpret 2DIR experiments.[23,25,26,46]

However, nonsecular relaxation may arise when bath interactions mutually couple a coherence state to other elements of the density matrix,[24,46,52–56] resulting in coherent dynamics. To characterize CVET one may include the full Redfield tensor in 2DIR simulations.[23,26,46,55,57,58] Such treatments explicitly consider Redfield tensor elements of the type Γ_{abac} , Γ_{abcd}, Γ_{abcc} and Γ_{aacd}. The first two terms describe coupling between coherences, and we refer to both as coherence transfer (CT). The last two terms describe coupling between populations and coherences. In both cases energy transfer occurs without a loss of phase information and is facilitated by mutual coupling to a bath coordinate. Timescales of these CVET processes follow the lifetime of the originating state. In the case of CT this corresponds to coherence dephasing times, while coherence-population coupling may occur over the coherence lifetime of the doubly excited state or the vibrational lifetime of the population. Joint theoretical and computational investigations identify several spectral signatures of CVET such as line broadening,[23,52] forbidden peaks at early waiting times,[26,57] and additional oscillations in t_2 peak dynamics.[23,24,46,57]

Interpretations of these results are facilitated using Feynman diagrams which offer a convenient, if qualitative, means of accounting for CVET in 2DIR spectra. We present a handful of possible single-step CVET 2DIR pathways in figure 3.4-1(**b**,**c**).

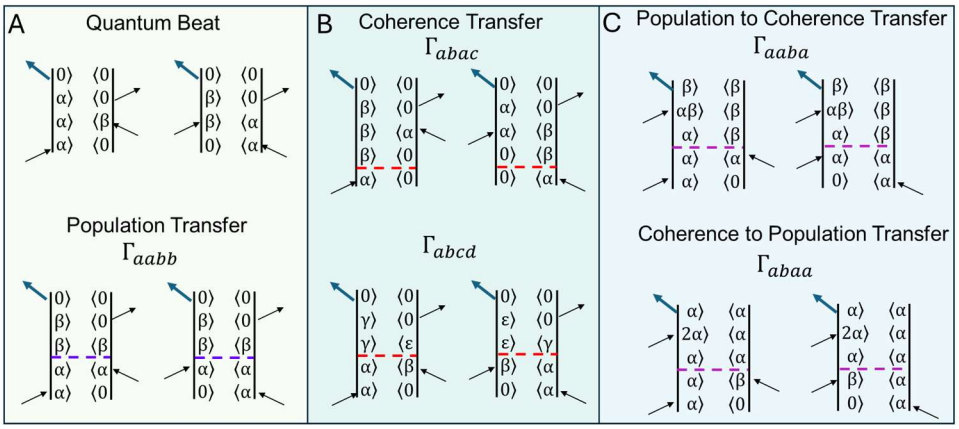

Figure 3.4-1: Examples of the Feynman diagram representation of various response pathways accessible by 2DIR: **(a)** quantum beating and population transfer, **(b)** coherence transfer, and **(c)** population-coherence transfer. The Redfield tensor elements for population transfer and nonsecular relaxation are given above the diagrams for the respective pathways. Dashed lines represent relaxation between system states.

These pathways consider a system of four coupled oscillators with singly excited states denoted by $|\alpha\rangle$, $|\beta\rangle$, $|\gamma\rangle$, and $|\varepsilon\rangle$. Secular diagrams for population transfer and quantum beating (QB) are given in figure 3.4-1(**a**) for comparison. The dashed horizontal lines in figure 3.4-1 indicate relaxation between states. To connect this representation to the above discussion, we include the Redfield tensor element for each dynamic response pathway. The upper two diagrams of figure 3.4-1(**b**) describe coherence transfer during the t_1 coherence period, and analogous diagrams can be drawn for CVET occurring during t_3. CVET contributions to cross peaks at early waiting times can be visualized by t_1 and t_3 CT pathways whose ω_1 and ω_3 positions match population transfer diagrams. Such processes also account for line shape distortions by introducing new dynamical processes during the coherence periods. Oscillations in peak intensities are accounted for by the creation of new quantum beating pathways when nonsecular relaxation is considered. QB pathways inherently pass through a coherence state during the t_2 waiting period,[25,26,46] and their intensities along t_2 fluctuate at the difference frequency of the

transitions making up the coherence. Conveniently, QBs manifest at unique frequency positions in the rephasing and non-rephasing diagrams under secular conditions. Deviations from this convention then give an experimental indication of nonsecular relaxation. The t_1 CT diagrams in figure 3.4-1(**b**) represent coherence transfer pathways which reverse the phase matching dependence of oscillatory peak positions with respect to the secular QBs in figure 3.4-1(**a**). The lifetime of CVET pathways is expected to be limited by the dephasing times of the coherences involved, and predominantly contribute to dynamics at early waiting times.[25]

While the Feynman diagram representation proves useful for assessing the potential impacts of additional relaxation pathways, the number of possible pathways quickly grows to the point of intractability (further examples given in A.6). Other works invoke the orientational symmetry requirements of third order response functions[43] to limit the number of relaxation pathways between orthogonal states.[23,24] However, in the case of Fermi coupling, transition dipole moments of the Fermi resonance peak are expected to have significant contributions from the fundamental,[20,39,59,60] and orientational restrictions are relaxed.[46] Marroux et al. proposed a method for eliminating QB pathways and certain coherence transfer pathways by utilizing pump selective experiments.[25] This method makes elimination of Feynman pathways in which the two pump pulses interact with separate oscillators at t_1 and t_2 possible, given sufficient control of the pump bandwidth. Such experiments fully eliminate QBs and reduce the number of nonsecular pathways available to the system. However, nonsecular pathways in which both excitation pulses resonate with a single oscillator still produce peaks in the unpumped regions of these spectra. We leverage this fact to explore complex networks of CVET in our system.

3.5 Results and Discussion

3.5.1 Linear IR

The linear IR (black) and second derivative (magenta) spectra of the carbonyl stretching region of EC in THF [figure 3.5.1-1] resolve three characteristic bands,[14,16,18] located at 1773 cm^{-1}, 1814 cm^{-1} and 1858 cm^{-1}.

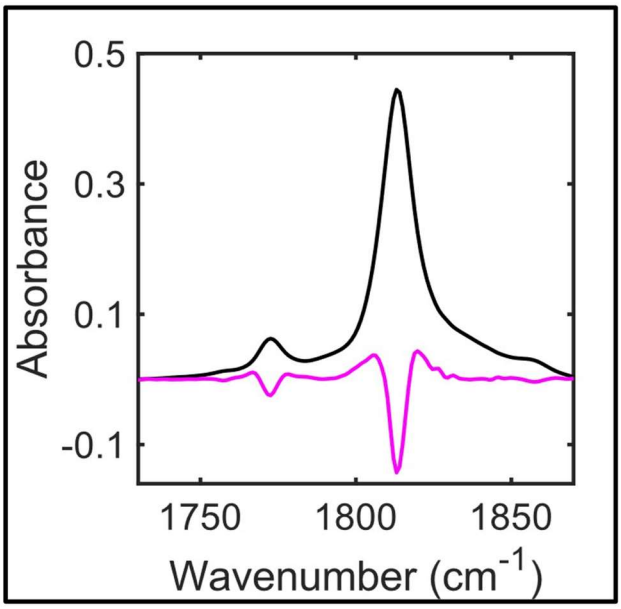

Figure 3.5.1-1: Background subtracted FTIR spectrum of EC in THF (black) and corresponding second derivative spectrum (magenta). Second derivative is scaled by a factor of 9.

The most intense band corresponds to the fundamental of the C=O carbonyl stretch, which is the only fundamental transition expected in the carbonyl region.[16,18] We assume all other bands arise from Fermi resonance couplings with the fundamental and do not consider multiple solvent configurations at this time. Of the two most intense Fermi resonance peaks, the lower frequency mode at 1773 cm^{-1} is assigned to the $2\nu_7$ overtone

of the ring breathing mode. The higher frequency band at 1858 cm^{-1} is then assigned to the $\nu_6 + \nu_7$ combination band between the ring breathing and stretching modes. Previous IR studies of liquid EC assign the fundamental frequencies for the $\nu_2, \nu_7,$ and ν_6 transitions to peaks at 1804 cm^{-1}, 893 cm^{-1} and 1073 cm^{-1} respectively.[16] The 10 cm^{-1} blue shift of the fundamental in figure 3.5.1-1 relative to previously reported values indicates nonnegligible solvatochromic effects in THF and reflects the general sensitivity of Fermi resonance bands to the local chemical environment.[14–18] As such, precise vibrational mode assignments for the linear spectrum require solvent inclusive frequency calculations which are beyond the scope of this work. We maintain the assignments of these bands out of convention, and our interpretation of the vibrational spectra relies chiefly on their fundamental (ν_2) and Fermi resonance ($\nu_6 + \nu_7,\ 2\nu_7$) character.

Between the fundamental and Fermi resonance peaks, the spectrum contains several weaker features which manifest as asymmetry on the high frequency side of the fundamental. Our second derivative spectrum indicates the presence of several additional peaks, which also appear as cross peaks in our 2D spectra. Further discussion of 2DIR cross peaks collected using our full pump bandwidth are given in A.5. In both linear and nonlinear experiments, the peaks at 1822 cm^{-1} and 1828 cm^{-1} appear as shoulders to the fundamental transition. Higher frequencies show a broad feature from 1831-1840 cm^{-1}. Below the fundamental we observe weak transitions in the range of 1780-1795 cm^{-1} as well as a small peak at 1758 cm^{-1}. We highlight the 1758 cm^{-1} peak due to its proximity to the carbonyl stretching modes of linear carbonates used in conjunction with EC in electrolyte solutions for lithium-ion batteries.[61] While the frequency positions of some of these features overlap with assignments made for solid ethylene carbonate,[16]

we do not expect aggregation in our sample based on prior concentration dependent studies.[14,15] However, time dependent linear IR spectra show slight changes in the relative peak intensities of the ν_2 and $2\nu_7$ bands after four hours, which likely reflect concentration dependent changes due to the evaporation of THF from the sample cell. To avoid the possibility of introducing concentration effects, we limit the acquisition time of our 2DIR experiments.

The linear IR spectrum of EC in THF highlights the congested nature of the carbonyl stretching region. We assume the three largest bands ($1773\,\mathrm{cm}^{-1}$,$1814\,\mathrm{cm}^{-1}$,$1858\,\mathrm{cm}^{-1}$) correspond to the $2\nu_7, \nu_2$ and $\nu_6 + \nu_7$ modes. The remaining bands arise from a complex network of Fermi resonance couplings between multi-quanta states and the ν_2 fundamental transition. We expect that some Fermi resonance bands share common first excited states, as is the case for the $2\nu_7$ and $\nu_6 + \nu_7$ bands. Due to the small size and high symmetry of EC this is a safe assumption,[16] and it suggests the possibility of dynamical pathways involving two or more Fermi resonance bands. To experimentally confirm the presence of such pathways and identify the coherent or incoherent nature of vibrational energy transfer in the carbonyl stretching region, we turn to 2DIR.

3.5.2 Diagonal Bleach: $\boldsymbol{\nu_2}$ and $\boldsymbol{2\nu_7}$

In this section we investigate the diagonal features of the ν_2 ($1814\,\mathrm{cm}^{-1}$) and $2\nu_7$ ($1773\,\mathrm{cm}^{-1}$) transitions. To separate intensity oscillations arising from secular quantum beating pathways and those arising from nonsecular CVET pathways, we compare the peak dynamics of the purely absorptive, real rephasing, and real non-rephasing spectra.

The rephasing and non-rephasing spectra were extracted from the purely absorptive data by previously outlined methods.[44] The results of this processing are shown in figure 3.5.2-1.

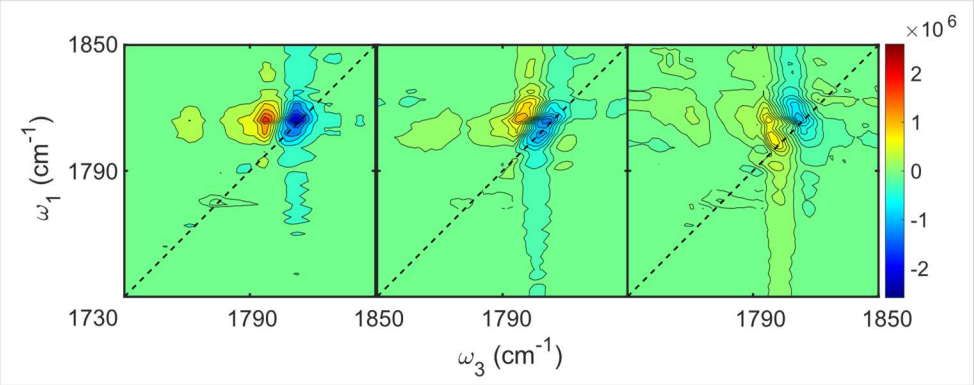

Figure 3.5.2-1: Left to right: The purely absorptive, real rephasing, and real non-rephasing 2DIR spectra at $t_2 = 300$ fs.

In non-rephasing (rephasing) spectra, secular quantum beats pathways appear as diagonal (cross) peaks. In the absence of CVET, oscillations in the diagonal peak intensities should only appear in the non-rephasing spectrum.

The 2DIR spectra of the ν_2 and $2\nu_7$ diagonal peaks are given in figure 3.5.2-2(**a**,**d**). Blue and red colors correspond to bleach and absorption features, respectively. figure 3.5.2-2(**a**) shows the ν_2 fundamental bleach at 1814 cm^{-1} and its corresponding absorption at 1797cm^{-1}, giving an observed diagonal anharmonicity of 17 cm^{-1}. The 2D spectrum also reveals an additional shoulder at 1808cm^{-1} which was not detected in the linear IR spectrum. We observe several cross peaks involving the fundamental in both the ω_1 and ω_3 directions. Slices along each frequency axis are given in A.5, as well as biexponential fits to the kinetic traces of select cross peaks obtained by integrating a square region of the peak intensities.

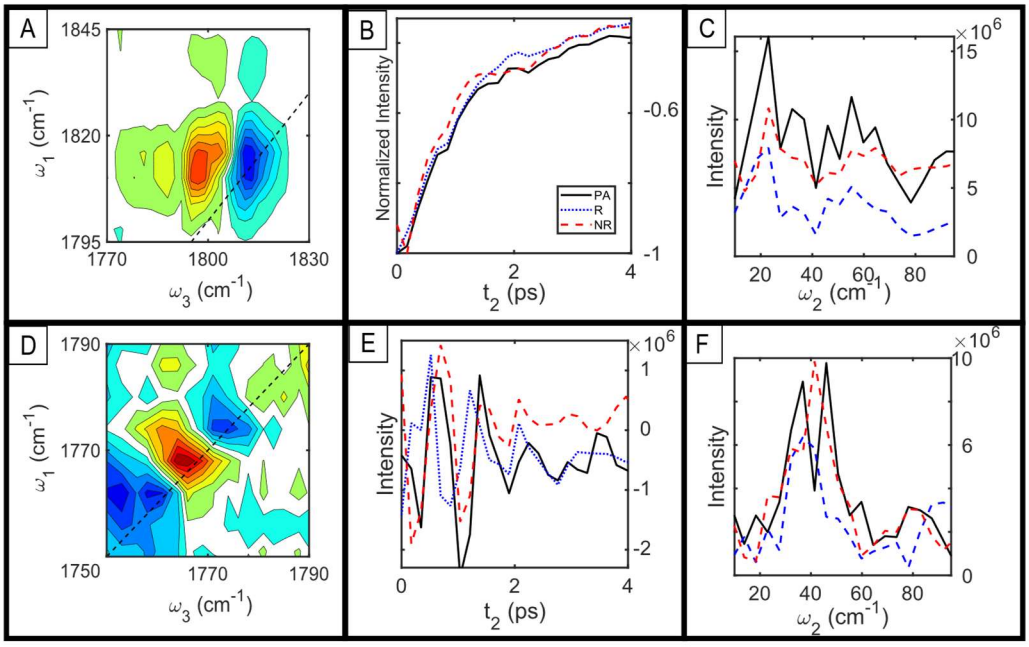

Figure 3.5.2-2: **(a).** Purely absorptive 2DIR spectrum of the diagonal band of the ν_2 transition at $t_2 = 300$ fs. The color scale ranges from -2.5E7 to 2.5E7 intensity units. **(b)**. Kinetic trace of the diagonal bleach for the purely absorptive (black solid), real rephasing (blue dotted), and real non-rephasing (red dashed) spectra. **(c)**. Absolute value power spectrum obtained by subtracting biexponential fits of the kinetic traces and Fourier-transforming about t_2. **(d)**. Real non-rephasing spectrum for the diagonal $2\nu_7$ Fermi resonance peak at $t_2 = 100$ fs and color scale -3E6 to 3E6. **(e-f)** Kinetic trace and power spectrum of diagonal bleach in (**d**).

To highlight oscillatory features in the ν_2 diagonal bleach, we plot the self-normalized kinetic traces [figure 3.5.2-2(**b**)] for the purely absorptive (black), real rephasing (blue), and real non-rephasing (red) spectra. Oscillations in the real rephasing spectrum indicate the presence of nonsecular relaxation,[49] although we first address the possibility of beating due to spectral overlap.[26,54] The power spectra, obtained by taking the Fourier transform of the kinetic trace over t_2, for each phase matching condition [figure 3.5.2-2(**c**)] show beat frequencies to at least 55 cm^{-1} which exceeds the approximately

16 cm^{-1} Gaussian linewidth obtained from the linear spectrum (see A.1). In that light congestion seems insufficient to explain the oscillatory dynamics of the fundamental bleach. Additionally, the presence of multiple peaks over a range of frequencies points to CVET pathways involving the fundamental and multiple Fermi resonance peaks.[46]

The oscillations in the diagonal peak intensities are clearly present in the $2\nu_7$ Fermi resonance peak at 1773 cm^{-1}. The non-rephasing spectrum of the $2\nu_7$ peak at t_2 =100 fs is plotted in figure 3.5.2-2(**d**). As shown by the kinetic trace in figure 3.5.2-2(**e**), this peak manifests predominantly as an oscillation. This likely reflects the low oscillator strength of the Fermi resonance transition compared to that of the fundamental. Based on the ratio of intensities between the two peaks in the linear spectrum (A.1) and the intensity of the diagonal bleach in figure 3.5.2-2(**a**), we estimate that response pathways involving only the $2\nu_7$ transition would only slightly exceed the noise floor of the experiment. On the contrary, QB pathways involving the stronger ν_2 transition should appear with much greater intensity, leading to the observed oscillations in figure 3.5.2-2(**e**). It is additionally possible that the low anharmonicity of the underlying ring mode causes annihilation between the excited state absorption and bleach features of traditional response pathways.[62] This further implies that the off-diagonal anharmonicity of the QB pathways exceeds the diagonal anharmonicity associated with the $2\nu_7$ mode. Again, oscillations in the real rephasing kinetic trace and corresponding peaks in the power spectrum indicate the 2DIR peak dynamics contain CVET contributions. The rephasing power spectrum in figure 3.5.2-2(**f**) contains peaks with notable intensity at $\omega_2 = 41\ \mathrm{cm}^{-1}$ (1732 cm^{-1}, 1814 cm^{-1}) and $\omega_2 = 85\ \mathrm{cm}^{-1}$ (1688 cm^{-1},1858 cm^{-1}), where the values in parentheses are 1773 $\mathrm{cm}^{-1} \pm \omega_2$. The $+\omega_2$ values coincide exactly with

the frequencies of the ν_2 fundamental transition (1814 cm^{-1}) and $\nu_7 + \nu_6$ Fermi resonance peak (1858 cm^{-1}), indicating that CVET processes involving both the fundamental and other Fermi coupled modes contribute to the observed dynamics of the $2\nu_7$ diagonal feature. As we detect neither evidence of vibrational ladder climbing[24,63,64] (A.7) nor accidental peak overlap[65] (A.8), we consider the dynamics observed in figure 3.5.2-2(**b**,**e**) to reflect genuine CVET pathways between vibrational resonance states in EC.

CVET contributions also appear in the observed frequency-frequency correlation function (FFCF) of the ν_2 diagonal bleach. The normalized FFCF, denoted by $\bar{C}(t_2)$, for the ν_2 band is given on the left-hand side of figure 3.5.2-3.

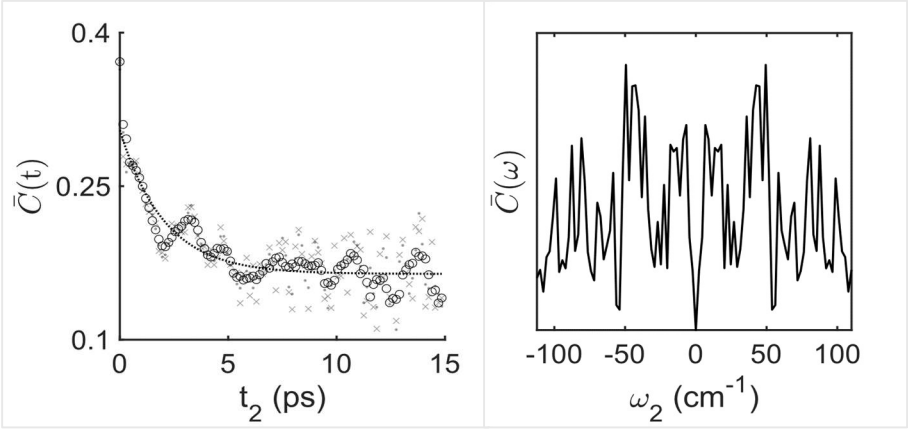

Figure 3.5.2-3: **Left.** The normalized frequency-frequency correlation function for the fundamental bleach obtained by inhomogeneity index. Scatter plots are given for rephasing and non-rephasing intensities treated with a moving average (circles), Savitzky–Golay (dot), and no filter (x). The dashed line gives the mono-exponential fit of the dotted line. **Right.** Normalized power spectral density obtained by subtracting the fit from the FFCF and Fourier-transforming about the waiting time.

We obtain the FFCF by means of the inhomogeneity index,[45,66] defined by:

(3-2) $$II(t_2) = \frac{A_R(t_2) - A_{NR}(t_2)}{A_R(t_2) + A_{NR}(t_2)}$$

and

(3-3) $$\bar{C}(t_2) = sin\left(\frac{\pi}{2}\, x\, II\right).$$

Here A_R and A_{NR} give the integrated intensity of the absolute value of the rephasing and non-rephasing spectra for a region of interest. We assess the contribution of noise by comparing the experimental FFCF when treating rephasing and non-rephasing intensities with different noise filters. The scatter plots in figure 3.5.2-3 correspond to a moving average filter (circles), Savitzky-Golay filter (x's), or no noise filter (dots). As all three data sets show similar oscillatory character out to 5 ps, we take this as the upper limit for experimentally resolving oscillations from noise. We fit $\bar{C}(t_2)$ to the form $ae^{\frac{-t_2}{\tau_{corr}}} + c$, yielding τ_{corr} =2.05 ± 0.36 ps. In the absence of strong coupling, τ_{corr} provides an approximate upper bound to the timescales of CVET involving the state $|v_2\rangle\langle 0|$ or its complex conjugate. Both the kinetic traces in figure 3.5.2-2(**b**,**e**) and the FFCF in figure 3.5.2-3 oscillate at times later than τ_{corr}, suggesting an extension of coherence lifetimes due to the coupling of coherences with elements of the system and/or bath.

The coupling of the system to low frequency bath modes may give rise to the oscillations of the FFCF. Such assignments have been made previously for time dependent vibrational studies of hydrogen bonding in water.[67–69] To assess the character of the oscillations, we investigate the spectral density $\bar{C}(\omega)$, obtained by subtracting the exponential component of $\bar{C}(t_2)$ and taking the Fourier transform of $\bar{C}(t_2)$. Those results are given on the right-hand side of figure 3.5.2-3. While the power spectral density reflects

many peaks, there are clusters near 11 cm^{-1}, 45 cm^{-1}, and 87 cm^{-1}. Librational motions with a frequency of 94 cm^{-1} were reported in the Raman spectrum of solid EC.[16] A computational and experimental study of the low frequency modes of THF found evidence of modes with frequencies in the 57-100 cm^{-1} range by neutron inelastic scattering, Raman active modes in the range of 14-70 cm^{-1} at temperatures of 150 K, and a 75 cm^{-1} IR band in liquid THF at 173 K.[70] Computational studies which examine coupling between EC dissolved in THF may attribute the oscillatory features of the 2DIR spectrum to such low frequency modes.

In the context of nonsecular relaxation between system states, such oscillations may arise from CVET processes during the t_2 waiting period. In this interpretation the timescales of the oscillations reflect either the dephasing times of coherences involving multiple excited states, or the lifetimes of populations coupled to coherence states. As we do not detect a dampening of the oscillations in $\bar{C}(t_2)$ before the onset of noise, we cannot use timescales to distinguish these effects directly. Instead, we estimate them from the quantum beating character of the $2\nu_7$ diagonal feature. The integrated intensity of the fits to the linear spectrum yields an approximately 3:1 transition dipole strength ratio for the ν_2 and $2\nu_7$ band. We expect the decay of the diagonal feature of the $2\nu_7$ band predominantly describes the dephasing of the coherence state $|\nu_2\rangle\langle 2\nu_7|$, as coherences between Fermi resonance states contribute only weakly.

To obtain dynamical data on the Fermi resonance band we follow the method of Roberts et al.[66] The relaxation is calculated according to:

(3-4) $$A_R + A_{NR} = \frac{\pi}{\langle \delta\omega^2 \rangle \sqrt{1-\bar{C}(t_2)^2}} e^{\frac{-t_2}{T_1}}$$

where T_1 is the vibrational relaxation and $\delta\omega$ is the fluctuation amplitude.[39,71] Rearranging this equation allows one to solve for T_1 while avoiding destructive interference between the rephasing and non-rephasing pathways. We test this method using the ν_2 diagonal bleach for which we obtain a biexponential decay with time constants of $T_1^{fast} = 1.39 \pm 0.3$ ps and $T_1^{slow} = 14.92 \pm 0.31$ ps. We compare these fits to values obtained by fitting the kinetic trace of the purely absorptive spectrum and find excellent agreement (see A.5). We then apply this metric to the $2\nu_7$ diagonal band, giving a singular exponential decay with time constant $T_1 = 0.94 \pm 0.29$ ps. Given that this feature appears as a quantum beat, it is not clear that this truly reflects population relaxation, but it does provide an estimate for the lifetimes of the doubly excited coherence states contributing to the underlying QB pathways. As most of the oscillator strength in the system comes from the ν_2 fundamental transition, we assign the decay of the $2\nu_7$ diagonal bleach feature to the dephasing of the state $|\nu_2\rangle \langle 2\nu_7|$. This rapid dephasing remains insufficient to explain the oscillatory behavior of the ν_2 diagonal bleach. It is possible that coherences between the fundamental and other Fermi resonance bands are longer lived, however the lack of dampening in the oscillations of the FFCF or the ν_2 diagonal kinetic trace suggests coherence lifetimes comparable to the population lifetime of the fundamental band. As coherences typically decay on timescales faster than vibrational relaxation, we instead interpret these long-lived oscillations as evidence of coherence-population coupling. In

this interpretation the interconversion of population and coherence states contributes to oscillations in the dynamics of the rephasing and non-rephasing spectra. Observation of coherence-population coupling does not preclude coupling between coherence states, which we investigate using pump selective 2DIR experiments.

3.5.3 Pump selective 2DIR

In this section we consider the positions and intensities of bandwidth forbidden cross peaks appearing in the unpumped regions of the pump selective spectra presented in figure 3.5.3-1. These peaks provide an additional experimental check for the presence of CVET. In a Feynman diagram picture one can imagine such peaks arising from responses of the form:

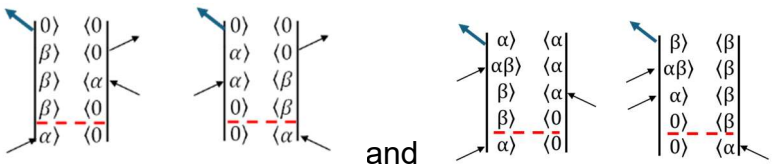

in which the transition from the ground state to α lies within the pump bandwidth and the ground state to β transition does not. Under these conditions no secular response pathways produce features at $\omega_1 = \omega_{\beta,0}$. This provides an intuitive picture by which the surviving nonsecular pathways contain character of both the allowed and bandwidth forbidden transitions over t_1, and therefore contribute to the unpumped region of the spectrum. While the Feynman diagram representation is not exact, we do find experimental evidence that forbidden cross peaks on the ω_1 axis correspond to coherence transfer occurring over the t_1 interval. In A.4 we compare the dynamics of the same cross peak under fully pumped (ordinary) and pump selective (forbidden)

conditions. We treat the time domain data with varying window functions and find the forbidden cross peaks show a greater sensitivity to the effective t_1 scan time. Whether this sensitivity can be leveraged to suppress or characterize CVET contributions in future 2DIR experiments remains to be seen.

The vertically plotted spectra of the righthand side of figure 3.5.3-1 give the normalized pump spectrum for each pump selective 2DIR experiment (left). The red dashed lines indicate the region in which the pump intensity falls below 10% of the maximum, and we consider features in this region to be bandwidth forbidden. The forbidden region of each spectrum is highlighted with a blue/grey background. We describe cross peaks in the fully pumped spectra as ordinary cross peaks. The frequency cutoffs of the pump pulses in figure 3.5.3-1(**a-d**) are: ω_{pump}>1795 cm^{-1}, ω_{pump}>1816 cm^{-1}, ω_{pump}<1831 cm^{-1} , and ω_{pump}<1815 cm^{-1}. The linear IR spectrum is plotted above for convenience.

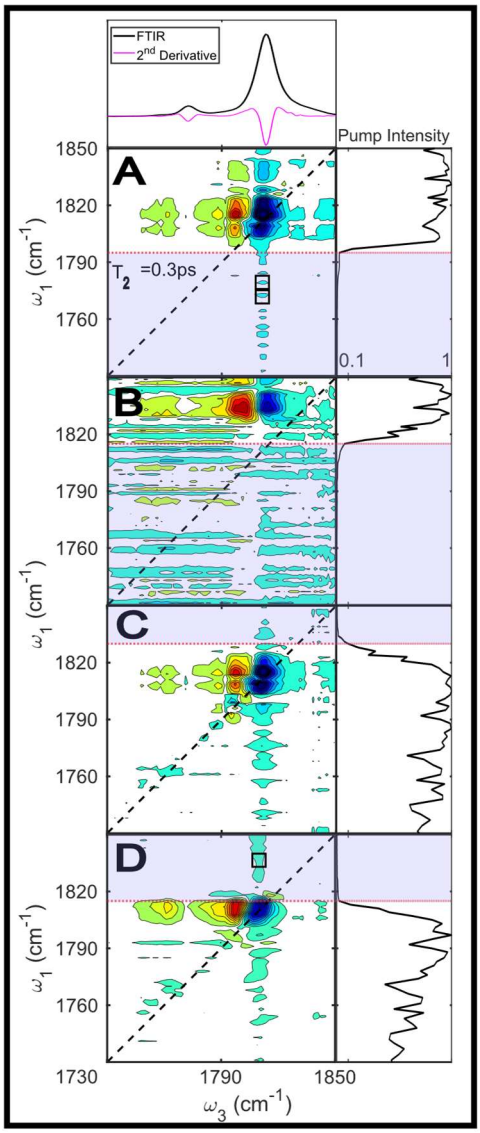

Figure 3.5.3-1: **Right.** normalized pump spectrum for each pump selective 2DIR experiment. **Left.** Pump selective 2DIR spectra at t_2 =300 fs. The red dashed lines indicate the ω_1 frequency at which features are considered forbidden, and the forbidden regions are marked by a blue/grey background. Black squares indicate cross peaks discussed in figure 3.5.3-2. The pump frequency cutoffs and color scale for each experiment are: (**a**) ω_{pump}>1795 cm^{-1} ($\pm$3E6) ,(**b**) ω_{pump} >1816 cm^{-1} ($\pm$2.5E5), (**c**) ω_{pump}<1831 cm^{-1} ($\pm$2.3E6), and (**d**). ω_{pump}<1815 cm^{-1} ($\pm$1.8E6).

Only the experiment in which the ν_2 fundamental transition (1814 cm^{-1}) lies outside the pump frequency [figure 3.5.3-1(**b**)] fails to resolve forbidden peaks, likely due to blocking the strong ν_2 fundamental transition. We focus our analysis on the bandwidth forbidden

peaks appearing at the detection frequency of the ν_2 fundamental. The number of anomalous peaks and the range over which they appear along ω_1 in figure 3.5.3-1 suggests CVET pathways disperse vibrational energy over many different overtone and combination states of low frequency modes. The observation of these forbidden peaks is significant, in that single coherence transfer pathways have been omitted in other studies investigating nonsecular relaxation in 2DIR, on the basis of transition dipole moment orthogonality in the corresponding model system.[25,26] The spectral signatures of single coherence transfer are thus not well characterized. This makes EC a strong candidate for theoretical investigations which may provide additional insight for interpreting coherence transfer in 2DIR spectra.

One alternative explanation for the range of forbidden peaks is incomplete cancellation between rephasing and non-rephasing pathways, resulting in phase twist.[25,26] This may arise from both secular and nonsecular quantum beating pathways and leads to distortions in the absorptive spectrum. If this is the origin of the forbidden peaks, their intensity should decay according to coherence dephasing rather than population lifetimes.[28] One would then expect the forbidden peaks to decay more rapidly during the waiting period. We fit the kinetic trace of four cross peaks to biexponential decays. The normalized fits to the intensity of forbidden pump-selective (colored) and ordinary full-pump (black) spectra are presented as insets of figure 3.5.3-2.

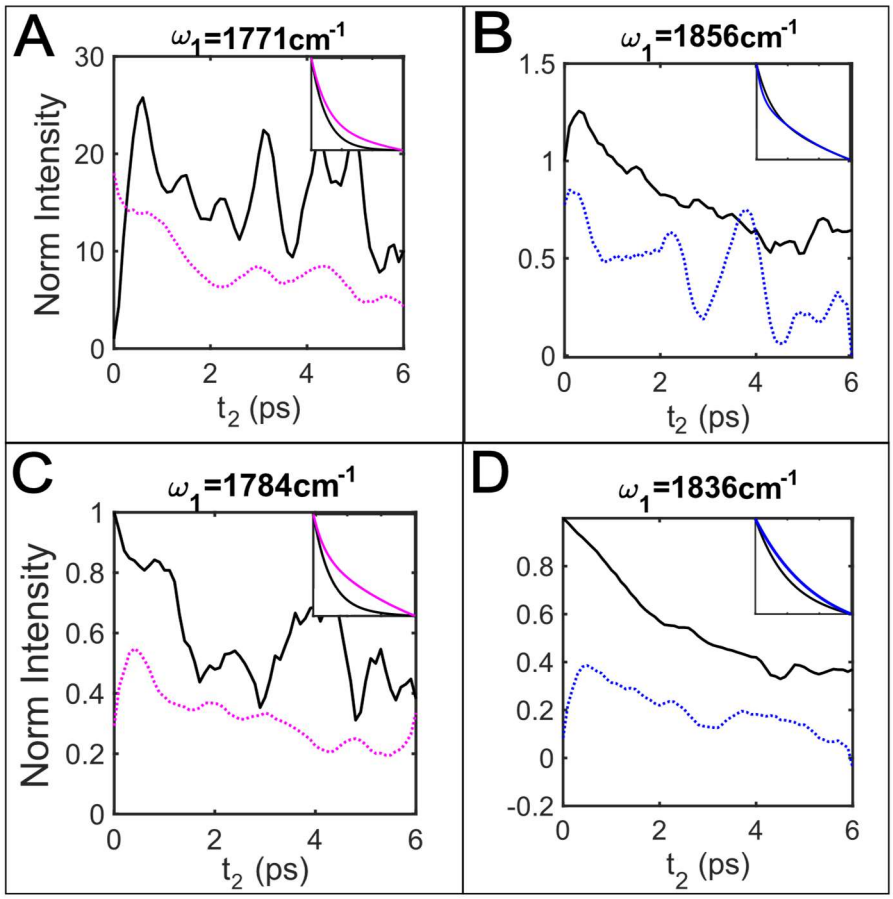

Figure 3.5.3.-2: Comparing kinetic traces for bandwidth forbidden cross peaks (dotted lines) to their ordinary cross peak (solid black). Both intensities are normalized to the fully pumped intensity at zero waiting time. (**a,c**) taken from pump selective experiment $\omega_{pump} > 1795\ \mathrm{cm}^{-1}$. (**b,d**) taken from pump selective experiment $\omega_{pump} < 1815\ \mathrm{cm}^{-1}$. Inset of each figure gives the normalized biexponential fit of the decay component of the integrated intensities. All kinetic traces were treated with a moving average filter to suppress high frequency noise.

The ω_1 position of the cross peak is given above each plot. From the fits in figure 3.5.3-2, we see that the forbidden peaks and the corresponding fully pumped cross peaks share similar t_2 dynamics and are therefore unlikely to be the result of incomplete cancellation between the rephasing and non-rephasing pathways. The observation that the bandwidth forbidden peaks in figure 3.5.3-2(**a**,**c**,**d**) have somewhat slower decays could suggest that ordinary pathways passing through a Fermi resonance population during t_2 are subject

to rapid relaxation, while CVET pathways involving t_2 coherences decay more slowly due to coupling with population states.

Next, we assess the potential impacts of CVET on interpretation of cross peak intensities. In the main portion of figure 3.5.3-2, we plot the ordinary and bandwidth forbidden cross peaks normalized to the initial intensity of the ordinary cross peak. figure 3.5.3-2(**a**,**b**) correspond to cross peaks between the fundamental and two most intense Fermi resonance bands ($2\nu_7, \nu_6 + \nu_7$) in the linear spectrum. Both show an initial growth in the fully pumped spectrum, indicating rapid vibrational energy transfer between the Fermi resonance modes and the ν_2 fundamental. Based on the ω_1 position of the cross peaks, growths in the kinetic trace could be interpreted as energy transfer from the Fermi resonance modes into the fundamental; however, a similar growth appears for the $\nu_6 + \nu_7$ bandwidth forbidden kinetic trace [figure 3.5.3-2(**b**)]. This indicates that the growth is not due to population transfer into ν_2, but rather it reflects CVET from the fundamental into $\nu_6 + \nu_7$. As such the dynamics could be significantly misinterpreted in the secular approximation. The bandwidth forbidden kinetic trace of the $2\nu_7$ cross peak [figure 3.5.3-2(**a**)] presents even more interesting dynamics, in that the initial intensity appears greater in the absence of direct excitation. This defies conventional wisdom, and we cannot offer a satisfactory explanation. Such results may reflect complicated relaxation processes involving multiple steps. Conversely, the cross peaks represented in figure 3.5.3-2(**c**,**d**) clearly show an initial growth only for forbidden peaks. In the case of figure 3.5.3-2(**c**), it appears this growth interferes with additional oscillatory components. This suggests the possibility of interference between secular quantum beating and potentially many CVET processes. If oscillatory processes contain phase offsets or different frequency

components, neither may be directly resolvable by experiment. In figure 3.5.3-2(**d**) the coherent growth appears masked by additional incoherent relaxation mechanisms present in the ordinary cross peak. Taken together these dynamics indicate a complex relationship between CVET, population dynamics, and secular quantum beating which need to be accounted for to extract accurate dynamics from 2DIR spectra.

From these experiments we also obtain some insight on the relative strength of CVET processes contributing to different peaks. Khalil et al. demonstrated the intensity of forbidden peaks at $t_2 = 0$ is proportional to the nonsecular transfer rate.[26] Applying this result to our pump selective experiments, we express the initial intensity of the forbidden cross peak as a percentage of the initial intensity of the ordinary cross peak. This metric gives an estimate of CVET character of the early time dynamics of each cross peak. We apply this metric to the kinetic traces in figure 3.5.3-2 to assess the strength of nonsecular relaxation for the cross peaks in figure 3.5.3-2(**b**-**d**). We do not interpret this value for figure 3.5.3-2(**a**), as competing effects clearly need consideration. The other peaks behave as expected, although the peaks in figure 3.5.3-2(**b**) and figure 3.5.3-2(**c**) show significant CVET contributions which make up 77% and 29% of the zero waiting time intensities, respectively. The peak in figure 3.5.3-2(**d**) indicates the weakest CVET character, with only 8% of its early waiting time intensity present in the pump selective data. It is interesting that the strongest Fermi resonance bands in the linear spectrum also show the greatest CVET character, although we cannot say if this indicates a more significant relationship or is simply a coincidence. Isotope labeling or solvent variational 2DIR experiments may serve to clarify the cause and nature of CVET in ethylene carbonate. The degree to which CVET presents itself in other Fermi coupled systems can

be assessed by time dependent vibrational studies which focus on identifying coherent dynamics.

3.6 Conclusion

From the linear IR spectrum, we observe that the carbonyl region of EC in THF represents a complex vibrational landscape containing multiple Fermi resonance peaks and a single fundamental transition. Immediately upon investigating the diagonal dynamics of the ν_2 fundamental we find evidence of coherent dynamics in the form of multiple oscillations in the real rephasing kinetic trace. The power spectrum of the oscillations in the kinetic trace suggests the coherent dynamics reflect coupling of the fundamental and several Fermi resonance modes. The diagonal bleach of the $2\nu_7$ Fermi resonance peak appears entirely as an oscillation and its power spectrum reveals CVET not only with the fundamental but also amongst Fermi resonance bands. We find the coherence lifetimes of the ν_2 and $2\nu_7$ diagonal peaks shorter than the timescale of coherent oscillations in the spectrum. We take this to indicate that the long-lived oscillations arise from coupling between coherence and population states.

We then confirm the presence of single coherence transfer pathways with pump selective 2DIR experiments. In those experiments we observe bandwidth forbidden peaks in the unpumped region of the spectrum, indicating single coherence transfer processes. As such it could serve as a system against which to test more general models of coherent dynamics. Upon investigating the relative intensities of unpumped cross peaks, we observe that several cross peaks contain significant contributions from CVET, with the cross peak corresponding to the $2\nu_7$ band appearing more strongly when it lies outside

the pump bandwidth. We find that the growth of forbidden cross peaks obscures the nature of vibrational dynamics in the system. The dynamics of forbidden peaks reflect a complex interplay of coherent and incoherent dynamics which must be carefully considered to extract accurate dynamical information from experiments. Future work will be needed to characterize these coherent dynamics and assess their information content, so that we can better utilize molecules like EC as vibrational probes.

References

(1) Galle Kankanamge, S. R.; Kuroda, D. G. Molecular Structure, Chemical Exchange, and Conductivity Mechanism of High Concentration LiTFSI Electrolytes. *J. Phys. Chem. B* **2020**, *124* (10), 1965–1977. https://doi.org/10.1021/acs.jpcb.9b10795.

(2) Fulfer, K. D.; Kuroda, D. G. Solvation Structure and Dynamics of the Lithium Ion in Organic Carbonate-Based Electrolytes: A Time-Dependent Infrared Spectroscopy Study. *J. Phys. Chem. C* **2016**, *120* (42), 24011–24022. https://doi.org/10.1021/acs.jpcc.6b08607.

(3) Fulfer, K. D.; Kuroda, D. G. Ion Speciation of Lithium Hexafluorophosphate in Dimethyl Carbonate Solutions: An Infrared Spectroscopy Study. *Phys. Chem. Chem. Phys.* **2018**, *20* (35), 22710–22718. https://doi.org/10.1039/C8CP03315C.

(4) Fulfer, K. D.; Galle Kankanamge, S. R.; Chen, X.; Woodard, K. T.; Kuroda, D. G. Elucidating the Mechanism behind the Infrared Spectral Features and Dynamics Observed in the Carbonyl Stretch Region of Organic Carbonates Interacting with Lithium Ions. *J. Chem. Phys.* **2021**, *154* (23), 234504. https://doi.org/10.1063/5.0049742.

(5) *Tale of a "Non-interacting" Additive in a Lithium-Ion Electrolyte: Effect on Ionic Speciation and Electrochemical Properties | The Journal of Physical Chemistry C*. https://pubs.acs.org/doi/10.1021/acs.jpcc.1c09193 (accessed 2024-03-12).

(6) Dereka, B.; Lewis, N. H. C.; Zhang, Y.; Hahn, N. T.; Keim, J. H.; Snyder, S. A.; Maginn, E. J.; Tokmakoff, A. Exchange-Mediated Transport in Battery Electrolytes: Ultrafast or Ultraslow? *J. Am. Chem. Soc.* **2022**, *144* (19), 8591–8604. https://doi.org/10.1021/jacs.2c00154.

(7) Fulfer, K. D.; Kuroda, D. G. A Comparison of the Solvation Structure and Dynamics of the Lithium Ion in Linear Organic Carbonates with Different Alkyl Chain Lengths. *Phys. Chem. Chem. Phys.* **2017**, *19* (36), 25140–25150. https://doi.org/10.1039/C7CP05096H.

(8) Liang, C.; Kwak, K.; Cho, M. Revealing the Solvation Structure and Dynamics of Carbonate Electrolytes in Lithium-Ion Batteries by Two-Dimensional Infrared Spectrum Modeling. *J. Phys. Chem. Lett.* **2017**, *8* (23), 5779–5784. https://doi.org/10.1021/acs.jpclett.7b02623.

(9) Lim, C.; Kim, J. H.; Chae, Y.; Lee, K.-K.; Kwak, K.; Cho, M. Solvation Structure around Li+ Ions in Organic Carbonate Electrolytes: Spacer-Free Thin Cell IR Spectroscopy. *Anal. Chem.* **2021**, *93* (37), 12594–12601. https://doi.org/10.1021/acs.analchem.1c02127.

(10) *Two-Dimensional Infrared Spectroscopy and Molecular Dynamics Simulation Studies of Nonaqueous Lithium Ion Battery Electrolytes | The Journal of Physical*

Chemistry B. https://pubs.acs.org/doi/10.1021/acs.jpcb.9b02026 (accessed 2024-03-12).

(11) *Effect of Solvation Shell Structure and Composition on Ion Pair Formation: The Case Study of LiTDI in Organic Carbonates | The Journal of Physical Chemistry C*. https://pubs.acs.org/doi/10.1021/acs.jpcc.9b07469 (accessed 2024-03-12).

(12) Zhang, X.; Kuroda, D. G. An Ab Initio Molecular Dynamics Study of the Solvation Structure and Ultrafast Dynamics of Lithium Salts in Organic Carbonates: A Comparison between Linear and Cyclic Carbonates. *J. Chem. Phys.* **2019**, *150* (18), 184501. https://doi.org/10.1063/1.5088820.

(13) Jiang, B.; Ponnuchamy, V.; Shen, Y.; Yang, X.; Yuan, K.; Vetere, V.; Mossa, S.; Skarmoutsos, I.; Zhang, Y.; Zheng, J. The Anion Effect on Li+ Ion Coordination Structure in Ethylene Carbonate Solutions. *J. Phys. Chem. Lett.* **2016**, *7* (18), 3554–3559. https://doi.org/10.1021/acs.jpclett.6b01664.

(14) Fini, G.; Mirone, P.; Fortunato, B. Evidence for Short-Range Orientation Effects in Dipolar Aprotic Liquids from Vibrational Spectroscopy. Part 1.—Ethylene and Propylene Carbonates. *J. Chem. Soc. Faraday Trans. 2 Mol. Chem. Phys.* **1973**, *69* (0), 1243–1248. https://doi.org/10.1039/F29736901243.

(15) Schindler, W.; Zerda, T. W.; Jonas, J. High Pressure Raman Study of Intermolecular Interactions and Fermi Resonance in Liquid Ethylene Carbonate. *J. Chem. Phys.* **1984**, *81* (10), 4306–4313. https://doi.org/10.1063/1.447440.

(16) Fortunato, B.; Mirone, P.; Fini, G. Infrared and Raman Spectra and Vibrational Assignment of Ethylene Carbonate. *Spectrochim. Acta Part Mol. Spectrosc.* **1971**, *27* (9), 1917–1927. https://doi.org/10.1016/0584-8539(71)80245-3.

(17) Klassen, B.; Aroca, R.; Nazri, M.; Nazri, G. A. Raman Spectra and Transport Properties of Lithium Perchlorate in Ethylene Carbonate Based Binary Solvent Systems for Lithium Batteries. *J. Phys. Chem. B* **1998**, *102* (24), 4795–4801. https://doi.org/10.1021/jp973099d.

(18) Bertran, J. F.; Ballester, L.; Dobrihalova, L.; Sánchez, N.; Arrieta, R. Study of Fermi Resonance by the Method of Solvent Variation. *Spectrochim. Acta Part Mol. Spectrosc.* **1968**, *24* (11), 1765–1776. https://doi.org/10.1016/0584-8539(68)80232-6.

(19) Zhang, J.; Wang, L.; Zhang, J.; Zhu, J.; Pan, X.; Cui, Z.; Wang, J.; Fang, W.; Li, Y. Identifying and Modulating Accidental Fermi Resonance: 2D IR and DFT Study of 4-Azido-l-Phenylalanine. *J. Phys. Chem. B* **2018**, *122* (34), 8122–8133. https://doi.org/10.1021/acs.jpcb.8b03887.

(20) Park, J. Y.; Mondal, S.; Kwon, H.-J.; Sahu, P. K.; Han, H.; Kwak, K.; Cho, M. Effect of Isotope Substitution on the Fermi Resonance and Vibrational Lifetime of Unnatural Amino Acids Modified with IR Probe: A 2D-IR and Pump-Probe Study of 4-

Azido-L-Phenyl Alanine. *J. Chem. Phys.* **2020**, *153* (16), 164309. https://doi.org/10.1063/5.0025289.

(21) Heyne, K.; Huse, N.; Dreyer, J.; Nibbering, E. T. J.; Elsaesser, T.; Mukamel, S. Coherent Low-Frequency Motions of Hydrogen Bonded Acetic Acid Dimers in the Liquid Phase. *J. Chem. Phys.* **2004**, *121* (2), 902–913. https://doi.org/10.1063/1.1762873.

(22) Gündoğdu, K.; Bandaria, J.; Nydegger, M.; Rock, W.; Cheatum, C. M. Relaxation and Anharmonic Couplings of the O–H Stretching Vibration of Asymmetric Strongly Hydrogen-Bonded Complexes. *J. Chem. Phys.* **2007**, *127* (4), 044501. https://doi.org/10.1063/1.2753840.

(23) Baiz, C. R.; Kubarych, K. J.; Geva, E. Molecular Theory and Simulation of Coherence Transfer in Metal Carbonyls and Its Signature on Multidimensional Infrared Spectra. *J. Phys. Chem. B* **2011**, *115* (18), 5322–5339. https://doi.org/10.1021/jp109357d.

(24) Eckert, P. A.; Kubarych, K. J. Vibrational Coherence Transfer Illuminates Dark Modes in Models of the FeFe Hydrogenase Active Site. *J. Chem. Phys.* **2019**, *151* (5), 054307. https://doi.org/10.1063/1.5111016.

(25) Marroux, H. J. B.; Orr-Ewing, A. J. Distinguishing Population and Coherence Transfer Pathways in a Metal Dicarbonyl Complex Using Pulse-Shaped Two-Dimensional Infrared Spectroscopy. *J. Phys. Chem. B* **2016**, *120* (17), 4125–4130. https://doi.org/10.1021/acs.jpcb.6b02979.

(26) Khalil, M.; Demirdöven, N.; Tokmakoff, A. Vibrational Coherence Transfer Characterized with Fourier-Transform 2D IR Spectroscopy. *J. Chem. Phys.* **2004**, *121* (1), 362–373. https://doi.org/10.1063/1.1756870.

(27) Redfield, A. G. The Theory of Relaxation Processes*. In *Advances in Magnetic and Optical Resonance*; Waugh, J. S., Ed.; Advances in Magnetic Resonance; Academic Press, 1965; Vol. 1, pp 1–32. https://doi.org/10.1016/B978-1-4832-3114-3.50007-6.

(28) Chang, T.-M.; Skinner, J. L. Non-Markovian Population and Phase Relaxation and Absorption Lineshape for a Two-Level System Strongly Coupled to a Harmonic Quantum Bath. *Phys. Stat. Mech. Its Appl.* **1993**, *193* (3), 483–539. https://doi.org/10.1016/0378-4371(93)90489-Q.

(29) Eastham, P. R.; Kirton, P.; Cammack, H. M.; Lovett, B. W.; Keeling, J. Bath-Induced Coherence and the Secular Approximation. *Phys. Rev. A* **2016**, *94* (1), 012110. https://doi.org/10.1103/PhysRevA.94.012110.

(30) Jeske, J.; Ing, D. J.; Plenio, M. B.; Huelga, S. F.; Cole, J. H. Bloch-Redfield Equations for Modeling Light-Harvesting Complexes. *J. Chem. Phys.* **2015**, *142* (6), 064104. https://doi.org/10.1063/1.4907370.

(31) Balzer, B.; Stock, G. Modeling of Decoherence and Dissipation in Nonadiabatic Photoreactions by an Effective-Scaling Nonsecular Redfield Algorithm. *Chem. Phys.* **2005**, *310* (1), 33–41. https://doi.org/10.1016/j.chemphys.2004.10.001.

(32) Ishizaki, A.; Fleming, G. R. On the Adequacy of the Redfield Equation and Related Approaches to the Study of Quantum Dynamics in Electronic Energy Transfer. *J. Chem. Phys.* **2009**, *130* (23), 234110. https://doi.org/10.1063/1.3155214.

(33) Engel, G. S.; Calhoun, T. R.; Read, E. L.; Ahn, T.-K.; Mančal, T.; Cheng, Y.-C.; Blankenship, R. E.; Fleming, G. R. Evidence for Wavelike Energy Transfer through Quantum Coherence in Photosynthetic Systems. *Nature* **2007**, *446* (7137), 782–786. https://doi.org/10.1038/nature05678.

(34) *Hidden vibronic and excitonic structure and vibronic coherence transfer in the bacterial reaction center*. https://doi.org/10.1126/sciadv.abk0953.

(35) Luther, B. M.; Tracy, K. M.; Gerrity, M.; Brown, S.; Krummel, A. T. 2D IR Spectroscopy at 100 kHz Utilizing a Mid-IR OPCPA Laser Source. *Opt. Express* **2016**, *24* (4), 4117–4127. https://doi.org/10.1364/OE.24.004117.

(36) Luther, B. M.; Tracy, K. M.; Krummel, A. T. Demonstrating 100 kHz 2D IR Spectroscopy Using a Mid-IR OPCPA Laser Source. In *International Conference on Ultrafast Phenomena (2016), paper UTu2A.5*; Optica Publishing Group, 2016; p UTu2A.5. https://doi.org/10.1364/UP.2016.UTu2A.5.

(37) Guchhait, B.; Tibbetts, C. A.; Tracy, K. M.; Luther, B. M.; Krummel, A. T. Ultrafast Vibrational Dynamics of a Trigonal Planar Anionic Probe in Ionic Liquids (ILs): A Two-Dimensional Infrared (2DIR) Spectroscopic Investigation. *J. Chem. Phys.* **2020**, *152* (16), 164501. https://doi.org/10.1063/1.5141751.

(38) Shim, S.-H.; Zanni, M. T. How to Turn Your Pump–Probe Instrument into a Multidimensional Spectrometer: 2D IR and Vis Spectroscopiesvia Pulse Shaping. *Phys. Chem. Chem. Phys.* **2009**, *11* (5), 748–761. https://doi.org/10.1039/B813817F.

(39) Hamm, P.; Zanni, M. *Concepts and Methods of 2D Infrared Spectroscopy*; Cambridge University Press: Cambridge, 2011. https://doi.org/10.1017/CBO9780511675935.

(40) Nishida, J.; Tamimi, A.; Fei, H.; Pullen, S.; Ott, S.; Cohen, S. M.; Fayer, M. D. Structural Dynamics inside a Functionalized Metal–Organic Framework Probed by Ultrafast 2D IR Spectroscopy. *Proc. Natl. Acad. Sci. U. S. A.* **2014**, *111* (52), 18442–18447. https://doi.org/10.1073/pnas.1422194112.

(41) Feng, Y.; Vinogradov, I.; Ge, N.-H. General Noise Suppression Scheme with Reference Detection in Heterodyne Nonlinear Spectroscopy. *Opt. Express* **2017**, *25* (21), 26262–26279. https://doi.org/10.1364/OE.25.026262.

(42) Feng, Y.; Vinogradov, I.; Ge, N.-H. Optimized Noise Reduction Scheme for Heterodyne Spectroscopy Using Array Detectors. *Opt. Express* **2019**, *27* (15), 20323–20346. https://doi.org/10.1364/OE.27.020323.

(43) Hochstrasser, R. M. Two-Dimensional IR-Spectroscopy: Polarization Anisotropy Effects. *Chem. Phys.* **2001**, *266* (2), 273–284. https://doi.org/10.1016/S0301-0104(01)00232-4.

(44) Zhang, Z.; Wells, K. L.; Hyland, E. W. J.; Tan, H.-S. Phase-Cycling Schemes for Pump–Probe Beam Geometry Two-Dimensional Electronic Spectroscopy. *Chem. Phys. Lett.* **2012**, *550*, 156–161. https://doi.org/10.1016/j.cplett.2012.08.037.

(45) Duan, R.; Mastron, J. N.; Song, Y.; Kubarych, K. J. Direct Comparison of Amplitude and Geometric Measures of Spectral Inhomogeneity Using Phase-Cycled 2D-IR Spectroscopy. *J. Chem. Phys.* **2021**, *154* (17), 174202. https://doi.org/10.1063/5.0043961.

(46) Nee, M. J.; Baiz, C. R.; Anna, J. M.; McCanne, R.; Kubarych, K. J. Multilevel Vibrational Coherence Transfer and Wavepacket Dynamics Probed with Multidimensional IR Spectroscopy. *J. Chem. Phys.* **2008**, *129* (8), 084503. https://doi.org/10.1063/1.2969900.

(47) Manzano, D. A Short Introduction to the Lindblad Master Equation. *AIP Adv.* **2020**, *10* (2), 025106. https://doi.org/10.1063/1.5115323.

(48) Montoya-Castillo, A.; Berkelbach, T. C.; Reichman, D. R. Extending the Applicability of Redfield Theories into Highly Non-Markovian Regimes. *J. Chem. Phys.* **2015**, *143* (19), 194108. https://doi.org/10.1063/1.4935443.

(49) Abramavicius, D.; Mukamel, S. Quantum Oscillatory Exciton Migration in Photosynthetic Reaction Centers. *J. Chem. Phys.* **2010**, *133* (6), 064510. https://doi.org/10.1063/1.3458824.

(50) Palmieri, B.; Abramavicius, D.; Mukamel, S. Lindblad Equations for Strongly Coupled Populations and Coherences in Photosynthetic Complexes. *J. Chem. Phys.* **2009**, *130* (20), 204512. https://doi.org/10.1063/1.3142485.

(51) Jang, S.; Cao, J.; Silbey, R. J. Fourth-Order Quantum Master Equation and Its Markovian Bath Limit. *J. Chem. Phys.* **2002**, *116* (7), 2705–2717. https://doi.org/10.1063/1.1445105.

(52) Kim, Y. S.; Hochstrasser, R. M. Comparison of Linear and 2D IR Spectra in the Presence of Fast Exchange. *J. Phys. Chem. B* **2006**, *110* (17), 8531–8534. https://doi.org/10.1021/jp060935n.

(53) Kim, Y. S.; Hochstrasser, R. M. The 2D IR Responses of Amide and Carbonyl Modes in Water Cannot Be Described by Gaussian Frequency Fluctuations. *J. Phys. Chem. B* **2007**, *111* (33), 9697–9701. https://doi.org/10.1021/jp074267x.

(54) Abramavicius, D.; Mukamel, S. Exciton Dynamics in Chromophore Aggregates with Correlated Environment Fluctuations. *J. Chem. Phys.* **2011**, *134* (17), 174504. https://doi.org/10.1063/1.3579455.

(55) Dahlbom, M.; Minami, T.; Chernyak, V.; Pullerits, T.; Sundström, V.; Mukamel, S. Exciton-Wave Packet Dynamics in Molecular Aggregates Studied with Pump−Probe Spectroscopy. *J. Phys. Chem. B* **2000**, *104* (16), 3976–3983. https://doi.org/10.1021/jp994172y.

(56) Chuntonov, L.; Kuroda, D. G.; Ghosh, A.; Ma, J.; Hochstrasser, R. M. Quantum Beats and Coherence Decay in Degenerate States Split by Solvation. *J. Phys. Chem. Lett.* **2013**, *4* (11), 1866–1871. https://doi.org/10.1021/jz400826a.

(57) Piryatinski, A.; Chernyak, V.; Mukamel, S. Vibrational-Exciton Relaxation Probed by Three-Pulse Echoes in Polypeptides. *Chem. Phys.* **2001**, *266* (2), 285–294. https://doi.org/10.1016/S0301-0104(01)00231-2.

(58) Chuntonov, L.; Ma, J. Quantum Process Tomography Quantifies Coherence Transfer Dynamics in Vibrational Exciton. *J. Phys. Chem. B* **2013**, *117* (43), 13631–13638. https://doi.org/10.1021/jp4075493.

(59) Edler, J.; Hamm, P. Two-Dimensional Vibrational Spectroscopy of the Amide I Band of Crystalline Acetanilide: Fermi Resonance, Conformational Substates, or Vibrational Self-Trapping? *J. Chem. Phys.* **2003**, *119* (5), 2709–2715. https://doi.org/10.1063/1.1586694.

(60) Chisler, E. V.; Davydov, V. Yu.; Goncharuk, I. N.; Ivanova, E. A. On Fermi Resonance Theory. *Phys. Status Solidi B* **1976**, *78* (1), 359–370. https://doi.org/10.1002/pssb.2220780137.

(61) Seo, D. M.; Reininger, S.; Kutcher, M.; Redmond, K.; Euler, W. B.; Lucht, B. L. Role of Mixed Solvation and Ion Pairing in the Solution Structure of Lithium Ion Battery Electrolytes. *J. Phys. Chem. C* **2015**, *119* (25), 14038–14046. https://doi.org/10.1021/acs.jpcc.5b03694.

(62) Rubtsova, N. I.; Rubtsov, I. V. Vibrational Energy Transport in Molecules Studied by Relaxation-Assisted Two-Dimensional Infrared Spectroscopy. *Annu. Rev. Phys. Chem.* **2015**, *66* (1), 717–738. https://doi.org/10.1146/annurev-physchem-040214-121337.

(63) Thielges, M. C.; Fayer, M. D. Time-Dependent Fifth-Order Bands in Nominally Third-Order 2D IR Vibrational Echo Spectra. *J. Phys. Chem. A* **2011**, *115* (34), 9714–9723. https://doi.org/10.1021/jp201516s.

(64) Strasfeld, D. B.; Shim, S.-H.; Zanni, M. T. Controlling Vibrational Excitation with Shaped Mid-IR Pulses. *Phys. Rev. Lett.* **2007**, *99* (3), 038102. https://doi.org/10.1103/PhysRevLett.99.038102.

(65) Rector, K. D.; Kwok, A. S.; Ferrante, C.; Tokmakoff, A.; Rella, C. W.; Fayer, M. D. Vibrational Anharmonicity and Multilevel Vibrational Dephasing from Vibrational Echo Beats. *J. Chem. Phys.* **1997**, *106* (24), 10027–10036. https://doi.org/10.1063/1.474060.

(66) Roberts, S. T.; Loparo, J. J.; Tokmakoff, A. Characterization of Spectral Diffusion from Two-Dimensional Line Shapes. *J. Chem. Phys.* **2006**, *125* (8), 084502. https://doi.org/10.1063/1.2232271.

(67) Stenger, J.; Madsen, D.; Dreyer, J.; Nibbering, E. T. J.; Hamm, P.; Elsaesser, T. Coherent Response of Hydrogen Bonds in Liquids Probed by Ultrafast Vibrational Spectroscopy. *J. Phys. Chem. A* **2001**, *105* (13), 2929–2932. https://doi.org/10.1021/jp003153h.

(68) Corcelli, S. A.; Lawrence, C. P.; Asbury, J. B.; Steinel, T.; Fayer, M. D.; Skinner, J. L. Spectral Diffusion in a Fluctuating Charge Model of Water. *J. Chem. Phys.* **2004**, *121* (18), 8897–8900. https://doi.org/10.1063/1.1803532.

(69) Asbury, J. B.; Steinel, T.; Kwak, K.; Corcelli, S. A.; Lawrence, C. P.; Skinner, J. L.; Fayer, M. D. Dynamics of Water Probed with Vibrational Echo Correlation Spectroscopy. *J. Chem. Phys.* **2004**, *121* (24), 12431–12446. https://doi.org/10.1063/1.1818107.

(70) Cadioli, B.; Gallinella, E.; Coulombeau, C.; Jobic, H.; Berthier, G. Geometric Structure and Vibrational Spectrum of Tetrahydrofuran. *J. Phys. Chem.* **1993**, *97* (30), 7844–7856. https://doi.org/10.1021/j100132a010.

(71) Kubo, R. A Stochastic Theory of Line Shape. In *Advances in Chemical Physics*; John Wiley & Sons, Ltd, 1969; pp 101–127. https://doi.org/10.1002/9780470143605.ch6.

Chapter 4
Manipulating Coherent Vibrational Relaxation in Ethylene Carbonate with Isotope Substitution[3]

4.1 Overview

Two-dimensional infrared spectroscopy (2DIR) and linear IR spectroscopy investigate the behavior of coherent vibrational energy transfer between Fermi coupled vibrations in a series of ethylene carbonate (EC) ^{13}C isotopologues. Analysis of the linear IR spectrum and the vibrational lifetimes of the Fermi doublet modes indicate that isotopic substitution strengthens the Fermi resonance condition while simultaneously suppressing population relaxation pathways involving a manifold of experimental dark states. The effects of this decoupling on the intrasystem relaxation of vibrational coherence states is investigated by Fourier analysis of 2DIR cross peaks and comparisons of the intensity of forbidden cross peaks in pump-selective 2DIR experiments. It is found that isotopic substitution also suppresses coherent relaxation pathways, indicating that coherent relaxation rates are governed by the effective coupling to the dark state manifold in a manner similar to population relaxation.

4.2 Introduction

Two-dimensional infrared spectroscopy (2DIR) is a time-resolved multi-dimensional technique that serves as a premier tool for studying vibrational energy

[3] This chapter has been submitted to the Journal of Physical Chemistry for review. It has been reprinted with permission from the authors; Luke Guerrieri, Sarah Hall, Carsten Mueller, Bradley M. Luther, and Amber T. Krummel.

transfer pathways on ultrafast timescales. 2DIR utilizes a three-pulse excitation scheme in which resonant interactions with the first and third pulses generate coherent superpositions of vibrational states which oscillate over the t_1 and t_3 experimental time delays. Fourier transforms of the 2DIR signal over the t_1 and t_3 coherence periods label the initial and final states of the vibrational relaxation pathway. Under ideal conditions for studying the dynamics of vibrational populations, the second pulse converts the t_1 coherence into an incoherent population state that evolves over the t_2 waiting period. In this picture, the t_2 dependence of diagonal peaks describes the dissipation of energy out of vibrational populations, while cross peak dynamics encode information on population transfer between optically bright vibrational modes.[1–4] In both cases the rates of population relaxation or population transfer report on the system-bath coupling parameters which drive the flow of vibrational energy.[5–7]

Complications to this picture arise when additional response pathways spectrally overlap with population relaxation pathways. For instance, quantum beating (QB) pathways appear frequently in broadband 2DIR experiments. QB pathways pass through coherence states during the experimental waiting time, leading to t_2 oscillations at the frequency difference of the vibrational modes making up the combination state. QB pathways are indicative of dipolar coupling between vibrational transitions, and their oscillations mask population relaxation rates in fits of 2DIR peak amplitudes.[8,9] A more challenging class of pathways that obscure population dynamics arise when the coherent superpositions, generated over any of the experimental waiting periods, are themselves subject to intrasystem relaxation processes. Such pathways reflect a failure of the secular

approximation to theories of relaxation in open quantum systems[10–14] and manifest as both anomalous peaks[9,15,16] and additional t_2 oscillations in the 2DIR spectrum.[17–19]

Non-secular relaxation processes can be broadly separated into coherence transfer and population-coherence transfer processes.[20] Coherence transfer represents a quantum analog of population transfer, in which one coherent superposition of system eigenstates converts into another due to interactions with bath modes.[21,22] Population-coherence transfer is closely related to quantum transport in excitonic systems,[23] although more generally describes correlated changes in population amplitudes and the phase relationships of coherent superpositions. For convenience, we refer to both processes as coherent relaxation or coherent dynamics. Coherent vibrational relaxation processes have been invoked to describe anomalous behavior in the 2DIR spectra of several organometallic compounds[15,17,18] as well as in mixtures of organic nitriles.[16] However, there is limited intuition about which chemical systems will display signatures of coherent relaxation, and it is not clear how quantitative information about coherent relaxation rates can be obtained directly from 2DIR experiments. While developing phenomenological models for accurately extracting molecular information from the observation of coherent relaxation remains an open theoretical challenge, previous investigations offer some insight into the parameter space governing coherent vibrational dynamics.

Previous investigations into non-secular relaxation in 2DIR spectroscopy indicate an apparent relationship between coherent dynamics and energy transfer processes involving both IR-active vibrations and experimentally hidden dark states.[16–19,24] In a theoretical investigation of coherent relaxation in dimanganese decacarboynl, Baiz et al.

found that coherent relaxation rates increased with the number of IR-inactive modes included in the system density matrix.[19] In that model, increasing the number of dark states effectively increases the local density of “bath” states strongly coupled to the optically bright transitions. In another theoretical investigation, Villaeys and Liang found that anomalous cross peaks in the 2DIR spectrum of benzonitrile and acetonitrile-d_3 mixtures could be modeled from intermolecular coherence transfer processes involving specific dark states which become populated by the dissipation of energy out of optically excited transitions.[16] Those results, which explicitly consider bright-dark anharmonic couplings known to influence population relaxation rates,[7] indicate a direct relationship between relaxation pathways involving dark states and the observation of coherent dynamics. The role of dark states in enabling the observation of coherent dynamics in 2DIR spectra was experimentally investigated by Eckert and Kubarych in a study of three diiron hexacarbonyl systems.[17] The authors found coherent oscillations in 2DIR cross peaks whose beating frequency corresponded to the energy gap between bright and dark vibrational modes, which could only be attributed to coherence transfer processes involving IR-inactive vibrations. Further, they found that chemical substitution of the bridging dithiolate group led to observation of unique coherent relaxation pathways in each compound. Their results prove interesting, as they indicate the possibility of manipulating coherent dynamics via straightforward chemical modifications. Modifying coherent dynamics in a predictable manner would mark an important step towards developing chemically insightful models of coherent relaxation in 2DIR. Further, control over coherent vibrational dynamics could be used to leverage the efficiency of quantum relaxation processes[25,26] in electron transfer pathways[27,28] or improve the quality of IR

probes in studies of population dynamics.[29] As such, a direct investigation of the ability to tune coherent dynamics by manipulating anharmonic couplings between bright and dark vibrations seems warranted.

Fortunately, the ability to control vibrational population relaxation via dark state coupling has been the focus of significant research,[3,4,7,29–32] and we presume those results apply similarly to the intrasystem relaxation of vibrational coherences. Fermi coupled vibrations, in which fundamental transitions couple to quasi-degenerate combination bands or overtones of lower energy vibrations,[33,34] often serve as model systems for investigating the influence of dark states on population relaxation. In the simplest picture, the fundamental transition and Fermi active two-quanta states mix directly through third-order anharmonic terms in the potential energy surface, and Fermi's Golden rule describes direct relaxation between the two modes.[35,36] However, experimental and theoretical studies of real chemical systems show that Fermi doublets often couple nonlinearly to additional manifolds of weakly Fermi active modes and IR-inactive vibrations.[7,31,36–39] As such, the observation of Fermi coupling between optically bright states suggests the presence of a more complex coupling network involving IR-active transitions and a dark state manifold. A study by Schmitz et al. showed that the vibrational energy transfer pathway between the cyano and azido modes of *para*-azidobenzonitrile could be directed through multiple dark states by using chemical substitution to weaken the Fermi resonance between the azido fundamental and combination bands of the benzene ring.[3] A subsequent investigation by Hassani et al. achieved suppression of dark state mediated relaxation pathways through heavy atom and isotopic substitutions for a similar benzonitrile scaffolding. [4] As isotopic substitution

should minimally impact the vibrational potential and interactions between a system and a thermal bath, it seems attractive for investigating the possibility of controlling coherent relaxation mechanisms by tuning anharmonic coupling.

As such, the work described here combines previously developed methods for suppressing dark state contributions to vibrational relaxation in Fermi coupled systems with spectroscopic investigations of coherent vibrational dynamics. This will provide evidence on the tunability of coherent relaxation pathways and provide mechanistic insight into the role of dark states in enabling coherent vibrational dynamics. Recently, we identified[40] signatures of coherent relaxation involving the Fermi coupled carbonyl fundamental and two-quanta ring modes of ethylene carbonate (EC). [41–44] Building on our previous results, this investigation compares the vibrational dynamics of the three EC isotopologues depicted in figure 4.2-1.

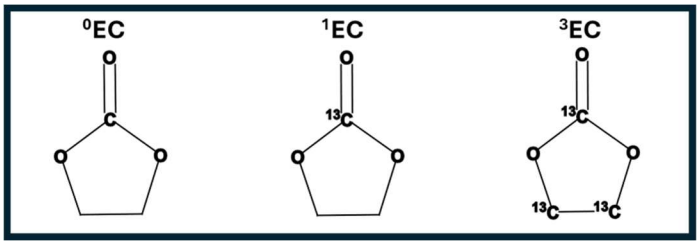

Figure 4.2-1: Isotopic series for unsubstituted ethylene carbonate (^{0}EC), ^{13}C substitution of the carbonyl carbon (^{1}EC), and fully ^{13}C substituted ethylene carbonate (^{3}EC).

We denote each isotopologue by the number of ^{13}C substitutions in the ring. ^{0}EC denotes the unsubstituted molecule. In ^{1}EC only the carbonyl carbon is isotopically substituted, while all three carbons in ^{3}EC are replaced by ^{13}C isotopes. We use similar notation to differentiate spectroscopic observables for each isotopologue throughout this text. Linear

IR spectroscopy quantifies the third-order anharmonic Fermi coupling constant and resonance parameter of the Fermi doublet for each isotopologue. The resonance parameter predicts the rate of direct (bright to bright) relaxation pathways, while the experimentally determined Fermi coupling constant provides some insights into the dark state contributions of the anharmonic coupling. As we cannot unambiguously quantify dark state contributions to the Fermi constant from the linear spectra, the coupling constants and resonance parameters are compared to the isotopic trend in vibrational lifetime measurements acquired from broadband 2DIR experiments to determine whether population relaxation pathways in EC proceed through direct or indirect (dark state mediated) mechanisms. We then assess signatures of coherence transfer in each isotopologue using Fourier analysis of waiting time dependent cross peaks[18,19] and an investigation of bandwidth forbidden peaks in pump-selective 2DIR experiments.[9,40]

4.3 Materials and Methods

4.3.1 Sample Preparation and Linear IR

Ethylene carbonate (EC) and its isotopologues were purchased from Sigma-Aldrich and tetrahydrofuran (THF) was purchased from Oakwood Chemical. Both were used without further purification. Samples were stored in a vacuum desiccator to avoid contamination from water. Samples for linear IR and 2DIR experiments consisted of 75 mM solutions of the respective EC isotopologue dissolved in THF. The solutions were sandwiched between a pair of 1 mm calcium fluoride (CaF_2) plates (Crystran) with a diameter of 25.4 mm. A 56 μm path length for each sample was set by Teflon spacers

(Harrick). We collected linear IR measurements with a Bruker Optics Vertex 70 spectrometer set to 64 scans and a resolution of 2 cm^{-1}.

4.3.2 100 kHz 2DIR spectrometer

A home built OPCPA ultrafast laser system produced the 100 kHz mid-IR pulse train used in 2DIR experiments. The operating principles of the system have been described previously.[45–47] These experiments utilized mid-IR pulses centered at 1750 cm^{-1} with an approximate FWHM of 200 cm^{-1}. A half waveplate and mid-IR thin film polarizer split the OPCPA output into pump and probe lines with tunable energy. Pulse energies at the sample were evenly divided between the two pump pulses and a single probe pulse, with an average energy of 70 nJ per pulse.

2DIR Data Collection

All 2DIR measurements took place in a partly collinear heterodyned pump-probe geometry[6,48] using a mid-IR pulse shaper (QuickShape+, PhaseTech Spectroscopy). Data collection utilized a 1x4 (2x2) phase cycling scheme[8] with a rotating frame of 1400 cm^{-1}. The time delay between the first two pump pulses (t_1) was scanned from 0 ps to 8 ps in 20 fs steps. Fourier transform of the heterodyned 2DIR signal took place on a monochromator, and the frequency resolved signal was measured using a 64-element mercury cadmium telluride (MCT) array detector at 100 kHz (Infrared Systems). A mechanically controlled delay stage on the probe line yielded 150 fs delay times between the second pump pulse and the probe pulse (t_2) which spanned 15 ps for broadband 2DIR experiments and 6 ps for pump-selective experiments. We employ a reference pixel noise reduction scheme[49,50] to limit the impact of probe noise on our spectra. Pump-

selective 2DIR experiments were performed to assess the significance of coherence transfer for each isotopologue. We take advantage of the diffraction gratings in our pulse shaper to limit pump bandwidth, in line with previous experiments.[8,9] Data collection utilized magic angle polarization conditions to produce isotropic data sets free of orientational relaxation contributions to the dynamics.[51]

2DIR Data Processing

The free induction decay at each pixel was treated with an exponential window function for the final 1 ps of each scan, zero padded with an additional 401 steps, and normalized to the laser power. A Fourier transform along t_1 generated the excitation axis ω_1. All 2D spectra and kinetic traces presented in this work consist of the real Fourier transform of the purely absorptive signal. 2DIR spectra presented in this work were interpolated in both frequency directions to give a virtual resolution of 0.5 cm^{-1}. Kinetic traces of 2DIR peaks were acquired by taking the mean intensity of an approximately circular region of each 2DIR spectrum with a radius of ~ 3 cm^{-1} at each t_2 step. The same procedure was performed in the low frequency region of the spectrum to quantify the detector noise of each virtual pixel along the ω_3 axis. Each kinetic trace was splined to a virtual resolution of 50 fs before being fit or Fourier transformed along t_2.

4.4 Results and Discussion

4.4.1 Isotopic Trends in Anharmonic Coupling and Resonance Strength from Linear IR

In this section we analyze the linear IR spectra (figure 4.4.1-1) of the carbonyl stretching region of ^{0}EC (black), ^{1}EC (red), and ^{3}EC (blue, dotted) dissolved in THF. We briefly compare the absorption profile of each isotopologue, before moving to quantitative assessment of the Fermi coupling constants (W) and resonance parameters (φ) of each.

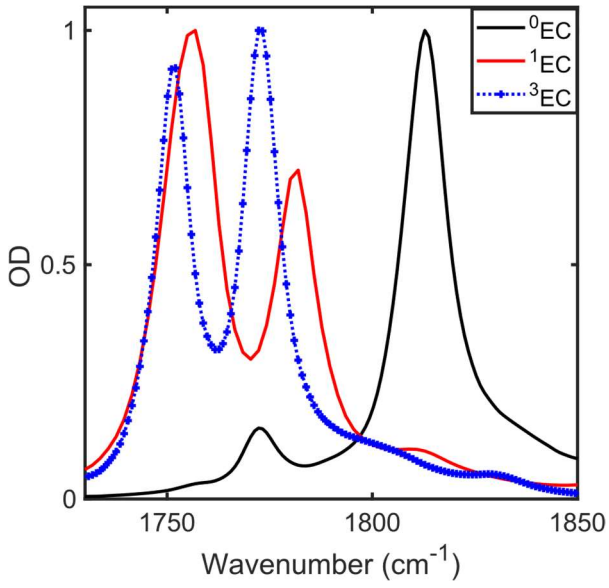

Figure 4.4.1-1: Normalized linear IR spectra of the carbonyl region of ^{0}EC (black), ^{1}EC (red), and ^{3}EC (blue, dotted) dissolved in THF.

To calculate the Fermi coupling constants from the linear spectra, we employ a two-state model derived from the assumption that only a single fundamental and two-quanta transition contribute to the anharmonic coupling.[52,53] When the anharmonic coupling involves additional vibrations, the experimentally derived values of W reflect the

cumulative influence of the additional states.[54–56] As such, this parameter provides an indication of how isotopic substitution modifies anharmonic coupling to additional dark states, and we expect to observe an inverse relationship between W and the vibrational lifetimes of the Fermi doublet modes, if dark states play a key role in the redistribution of vibrational energy. The resonance parameter (φ), defined by the ratio of the Fermi coupling constant and the frequency splitting of the Fermi doublet, is predictive of direct vibrational energy transfer rates pathways between the Fermi coupled modes.[3,4] Comparing the trends in these two parameters to the vibrational lifetimes of the carbonyl and ring modes will serve to identify the direct or indirect nature of the dominant relaxation mechanisms in EC isotopologues and further inform analysis of the role of dark states in facilitating coherent relaxation.

We define the Fermi doublet for each isotopologue as consisting of the two most intense peaks in each spectrum shown in figure 4.4.1-1. The more intense peak is assigned to the fundamental transition of the C=O carbonyl stretch (centered at ω_C) , and is the only fundamental transition expected to contribute in this region.[41,42,44] The weaker peak in each doublet is associated with a two-quanta transition of the ring modes (centered at ω_R). Other weaker peaks are attributable to isotopic residues or weakly Fermi active bands and are not explicitly considered in the present analysis. Lorentzian fits were used to characterize the Fermi doublet of each isotopologue, and the results of those fits are summarized in table 4.4.1-1.

Table 4.4.1-1: Results of Lorentzian fits to the linear IR spectrum and calculations of the third order resonance parameter.

		Center Frequency (ω)	Peak Splitting ($\Delta\omega_{C,R}$)	Intensity Ratio (R)	Fermi Constant (W)	Resonance Parameter (φ)
^{0}EC	$^0\omega_C$	1814 cm^{-1}	41 cm^{-1}	11.7	14.3 cm^{-1}	0.35
	$^0\omega_R$	1773 cm^{-1}				
^{1}EC	$^1\omega_C$	1757 cm^{-1}	-24 cm^{-1}	2.1	11.8 cm^{-1}	0.49
	$^1\omega_R$	1781 cm^{-1}				
^{3}EC	$^3\omega_C$	1773 cm^{-1}	21 cm^{-1}	1.2	11 cm^{-1}	0.52
	$^3\omega_R$	1752 cm^{-1}				

Both the spectra presented in figure 4.4.1-1 and the corresponding Lorentzian fit parameters reveal significant differences in the IR absorption profile of each isotopologue. Fitting the center frequencies of the Fermi doublets, denoted by the coordinate pair (ω_C, ω_R), yields (1814 cm^{-1}, 1773 cm^{-1}) for ^{0}EC, (1757 cm^{-1}, 1781 cm^{-1}) for ^{1}EC, and (1773 cm^{-1}, 1752 cm^{-1}) for ^{3}EC. The level inversion ($\omega_C < \omega_R$) in ^{1}EC is consistent with previous isotopic studies of ethylene carbonate.[42] This inversion reflects a redshift in the carbonyl fundamental band which is made more pronounced by the Fermi resonance coupling. Substitution of the remaining ring carbons leads to a redshift in the Fermi active ring modes of ^{3}EC, causing the more intense carbonyl band to again appear at a higher frequency than the two-quanta ring mode. A previous comparison of ^{0}EC and ^{1}EC by Al-Jallo and Al-Azawi attributes the two-quanta state to the first overtone of the CH_2 rocking mode.[42] To examine whether this assignment holds for ^{3}EC, we examined anharmonic frequency calculations for each isotopologue. We find that substitution of the remaining ring carbons in ^{3}EC produces a redshift in the calculated frequency of the rocking overtone and a slight blueshift in the frequency of the carbonyl fundamental relative to

^{1}EC. These results are consistent with the observed trend in the linear IR spectra, supporting an assignment of the lower frequency band of ^{3}EC to the first overtone of the CH_2 rocking mode.

Further changes in the absorption spectrum can be seen in the relative intensities of the Fermi doublet peak pairs. The ratio of integrated peak intensities, defined as $R = \frac{I_C}{I_R}$, for each isotopologue decreases from ^{0}R = 11.7 to ^{1}R = 2.1 to ^{3}R = 1.2. As the two-quanta ring modes possess negligible oscillator strength in the absence of coupling,[41] the equalization in the linear intensities with increasing ^{13}C substitution reflects an enhancement of the dipolar coupling between the carbonyl and ring modes, although further analysis is needed to clarify if this enhancement arises due to improved degeneracy between the modes or an increase in the Fermi coupling constant. To both assess the nature of the resonance enhancement and gain predictive insight on the vibrational dynamics of our isotopic series, we first calculate the Fermi constant according to: [41,52,53,55]

(4-1) $$R = \left\{ \frac{\left[\Delta+\left(\Delta^2-4W^2\right)^{1/2}\right]^{1/2} {R_0}^{1/2} \mp \left[\Delta-\left(\Delta^2-4W^2\right)^{1/2}\right]^{1/2}}{\pm\left[\Delta+(\Delta^2-4W^2)^{1/2}\right]^{1/2}+\left[\Delta-(\Delta^2-4W^2)^{1/2}\right]^{1/2} {R_0}^{1/2}} \right\}^2 .$$

Here R gives the ratio of the integrated intensity of the Lorentzian fits, R_0 gives the intensity ratio under the harmonic approximation which we set to 100 in accordance with previous calculations,[41] and $\Delta = \Delta\omega_{C,R}$ corresponds to the frequency separation between the Fermi doublet peaks in the linear spectrum. From these calculations we obtain anharmonic coupling strengths of ^{0}W = 14.3 cm $^{-1}$, ^{1}W = 11.8 cm $^{-1}$, and ^{3}W = 11.0 cm $^{-1}$.

These results show that isotopic substitution progressively reduces the effective anharmonic coupling between the carbonyl and ring modes of the Fermi doublet. Working under the assumption that the changes in the effective anharmonic coupling reflect changes in dark state contributions to the anharmonicity, the 2.5 cm $^{-1}$ decrease in the Fermi constant of ^{1}EC compared to ^{0}EC reflects a decoupling of the carbonyl stretch from the motion of the ring. We interpret the further 0.8 cm $^{-1}$ reduction in the Fermi constant of ^{3}EC as the decoupling of the Fermi active ring mode from additional IR-inactive states. As such, if indirect coupling mechanisms dominate vibrational relaxation in ethylene carbonate, we expect slower relaxation in the isotopically substituted molecules. From the Fermi constants we additionally see that the increase in the linear intensity ratios of ^{1}EC and ^{3}EC arises due to enhanced degeneracy[57] rather than increased anharmonic coupling strengths. To predict trends in the vibrational relaxation rates for direct transfer between the carbonyl and ring modes, we calculate the resonance parameter $\varphi = \left|\frac{W}{\Delta\omega_{C,R}}\right|$. For each of the isotopologues we obtain the values of $^{0}\varphi = 0.35$, $^{1}\varphi = 0.49$, and $^{3}\varphi = 0.52$. Although the experimentally obtained values of W likely reflect weak contributions from additional states, the dependence of φ on the frequency separation of the Fermi doublet makes it unlikely that those contributions introduce significant error in this result. Given that φ reflects vibrational energy transfer rates between the Fermi coupled modes, this trend predicts that direct relaxation pathways will proceed more efficiently in ^{1}EC and ^{3}EC. This directly contradicts predictions of vibrational relaxation rates based on the W. As such, resolving this contradiction by comparing trends in both parameters to the vibrational lifetimes of the Fermi doublet modes will serve as a basis for uncovering the direct or indirect nature of vibrational relaxation in EC.

4.4.2 Determining Population Relaxation Mechanisms in EC Isotopologues

Broadband 2DIR

In this section we investigate the broadband 2DIR spectra of the isotopic series, with a focus on the decay of the diagonal carbonyl bleach (S_{CC}) and the diagonal ring bleach (S_{RR}) for each isotopologue. Representative purely absorptive 2DIR spectra are presented in figure 4.4.2-1 for ^{0}EC (**a**), ^{1}EC (**b**) and ^{3}EC (**c**).

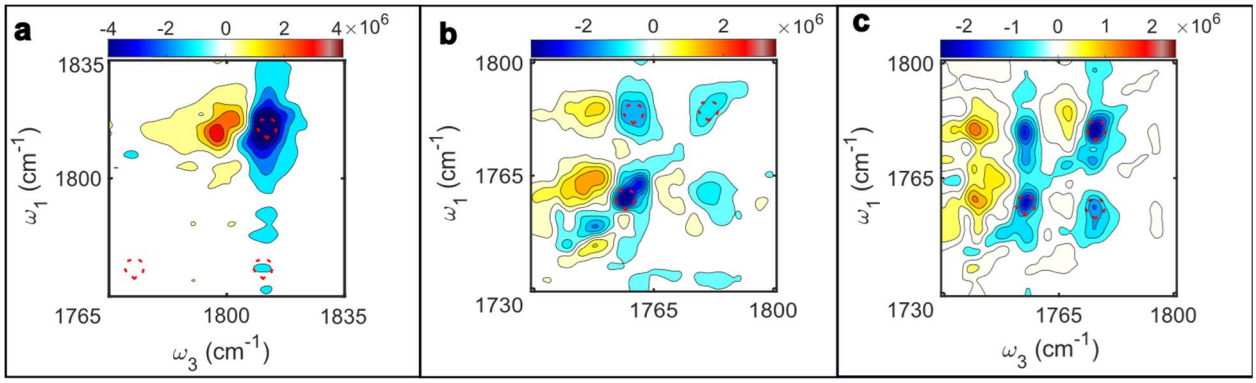

Figure 4.4.2-1: Purely absorptive broadband 2DIR spectra for ^{0}EC (**a**), ^{1}EC (**b**), and ^{3}EC (**c**). All spectra shown here were collected at t_2 = 1.5 ps and plotted with eleven equally spaced contours. Bleach features correspond to negative intensities (blue) and absorptive features are denoted by positive intensities (red). Spectral regions investigated to produce kinetic traces for time dependent analysis of the peak amplitudes are indicated by red dashed circles.

Negative going peaks for emission and bleach pathways are colored in blue and absorption peaks are shaded in red. All spectra in figure 4.4.2-1 are plotted at a waiting time of t_2 = 1.5 ps. The spectral regions used to generate kinetic traces for S_{CC}, S_{RR}, and the S_{RC} cross peak [centered at $(\omega_1, \omega_3) = (\omega_R, \omega_C)$] are marked with red dashed circles.

General features of the 2DIR spectra behave as expected from the linear IR spectra. In ^{0}EC (4.4.2-1**a**) the only on-diagonal spectral feature that appears at the level of detail shown in figure 4.4.2-1. is the $^{0}S_{CC}$ carbonyl bleach. The poor resolution of $^{0}S_{RR}$ reflects the weak resonance condition of the Fermi doublet which prohibits transition dipole mixing of the carbonyl fundamental and two-quanta ring mode. However, evidence of coupling between the carbonyl and a weakly Fermi active manifold in ^{0}EC appears as an elongated network of cross peaks in the spectral region of $\omega_3 = \omega_C$. The larger resonance parameters of ^{1}EC and ^{3}EC allow for clear observation of the diagonal ring modes and Fermi doublet cross peaks in both ^{13}C substituted compounds. This improvement in resolving the ring modes of the Fermi doublet comes at the penalty of increased spectral congestion. The small frequency spacing between the doublets of ^{1}EC and ^{3}EC as well as potential contributions from isotopic residues and weakly Fermi active modes produces the rather complicated spectra shown in figure 4.4.2-1**b**-**c**. Unfortunately this congestion simply marks a limitation of our analysis.

Vibrational Lifetimes of EC Fermi Doublets

Assuming solvent contributions to the relaxation of the carbonyl band remain roughly constant across the isotopic series, the vibrational lifetimes of the carbonyl fundamental and ring mode characterize the local density of states coupled to each.[7,38] We assess both by examining the t_2 kinetic traces of $S_{C,C}$ (figure 4.4.2-2**a**) and $S_{R,R}$ (figure 4.4.2-2**b**) diagonal bleach peaks.

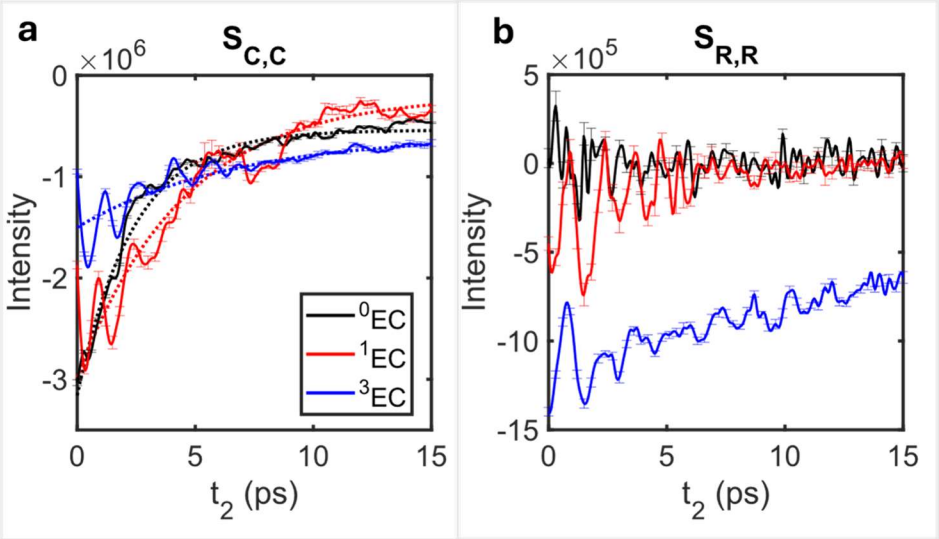

Figure 4.4.2-2: Kinetic traces of the S_{CC} and S_{RR} peaks for ^{0}EC (black), ^{1}EC (red), and ^{3}EC (blue). **(a)** Kinetic traces (solid) and single exponential fits (dashed) for the carbonyl diagonal bleach of each isotopologue. The intensity of the ^{0}EC trace is scaled by a factor of one third. Error bars give the average detector noise for the interpolated pixels used to generate the kinetic trace. **(b)** Same as **a** for the kinetic traces of the S_{RR} diagonal bleach.

For the carbonyl mode, we fit kinetic traces of $S_{C,C}$ to a single exponential function of the form $ae^{\frac{-t_2}{T_1}} + C$, where T_1 reports on the vibrational lifetime of the carbonyl stretch. Both kinetic traces (solid) and exponential fits (dashed) are given in figure 4.4.2-2**a**. We note that the intensity of $^0S_{C,C}$ is scaled by a factor of one third to facilitate comparison. The resulting fits return values of $^0T_1$ = 2.38 ± 0.06 ps, $^1T_1$ = 4.46 ± 0.08 ps, and $^3T_1$ = 6.59 ± 0.07 ps. The progressive extension of vibrational lifetimes upon isotopic substitution matches the predictions based on the effective anharmonic coupling parameter W rather than the resonance condition φ, indicating that the relaxation of the carbonyl mode depends on the anharmonic coupling to a dark state manifold rather than the strength of the Fermi resonance.

For $S_{R,R}$ we assess the influence of dark states qualitatively, due the poor signal to noise ratio of ${}^{0}S_{R,R}$ and highly oscillatory nature of all three kinetic traces shown in figure 4.4.2-2**b**. Consistent with our previous findings,[40] ${}^{0}S_{R,R}$ oscillates about zero intensity at early waiting times and quickly falls to the noise level of the experiment. This indicates that, if ${}^{0}S_{R,R}$ reports on population relaxation at all, relaxation occurs rapidly. Similar dynamics appear more clearly in ${}^{1}S_{R,R}$, due to the enhanced resonance condition of the Fermi doublet. Interestingly, ${}^{1}S_{R,R}$ oscillates about an offset at early waiting times rather than zero intensity. This could indicate slower population relaxation due to decoupling between the bright Fermi active mode and a dark state manifold, although the low intensity of ${}^{0}S_{R,R}$ makes direct comparisons between the two somewhat dubious. Rather, the effect of isotopic substitution in extending the vibrational lifetime of the ring becomes significantly more pronounced in ${}^{3}S_{R,R}$. Although strong oscillations appear in the kinetic trace of ${}^{3}S_{R,R}$, an almost linear decay indicates that the population relaxation pathways underlying the peak are largely decoupled from any potential dark state manifold. From the kinetic traces of figure 4.4.2-2**b**, we observe an isotopic trend that indicates a minor decoupling of the ring and dark state manifold upon ^{13}C substitution of the carbonyl carbon in ^{1}EC, and significant decoupling upon ^{13}C substitution of the other ring carbons in ^{3}EC.

In terms of predicting the behavior of coherent relaxation in each isotopologue, the correlated trends in the effective anharmonic coupling and the vibrational lifetimes of the ring and carbonyl modes indicate that dark states play an important role in the vibrational dynamics of EC. The extension of the vibrational lifetimes of $S_{C,C}$ and $S_{R,R}$ upon isotopic

substitution indicates a progressive reduction in the ability of the Fermi doublet to dissipate energy into a reservoir of dark states. This is important for descriptions of coherent relaxation that require bath modes to mutually couple coherent superpositions to other elements of the system density matrix.[5,10,14,19] If the overall density of states around each bright state in the Fermi doublet decreases, so does the likelihood that their coherences couple strongly to the same dark degrees of freedom. Decoupling one or both states from the bath (which contains all experimentally dark degrees of freedom) should produce a decrease in the coherent relaxation rate and fewer signatures of coherent relaxation in the 2DIR spectrum.

4.4.3 Identifying Signatures of Coherent Vibrational Relaxation

We investigate the signatures of coherent relaxation pathways in the EC isotopic series in two ways. The first involves Fourier analysis of the $S_{R,C}$ cross peak kinetic trace for the broadband 2DIR experiments (integration regions shown in figure 4.4.2-1). Under secular conditions, QB contributions to $S_{R,C}$ are expected to oscillate along t_2 at a frequency of $\Delta\omega_{C,R}$. However, coherent relaxation processes can lead to additional oscillations in $S_{R,C}$, and so multiple peaks in the Fourier spectrum of the $S_{R,C}$ kinetic trace (denoted $F_{R,C}$) serve as evidence of coherent relaxation.[17,18] Our second method relies on pump-selective 2DIR experiments in which the ring transition lies outside the excitation bandwidth of the first two mid-IR pulses. In this experimental configuration, coherent relaxation manifests as a bandwidth forbidden cross peak in the unpumped region of the 2DIR spectrum.[9] Specifically, we examine the bandwidth forbidden kinetic trace of the $S_{R,C}$ cross peak (denoted $S^{F}{}_{R,C}$). We choose the $S_{R,C}$ cross peak for this analysis based on previous pump-selective 2DIR experiments which indicated that this cross peak had

strong contributions from coherence transfer pathways in ^{0}EC, and so is expected to have a greater sensitivity to changes in coherent relaxation rates due to changes in system-bath coupling parameters.[40]

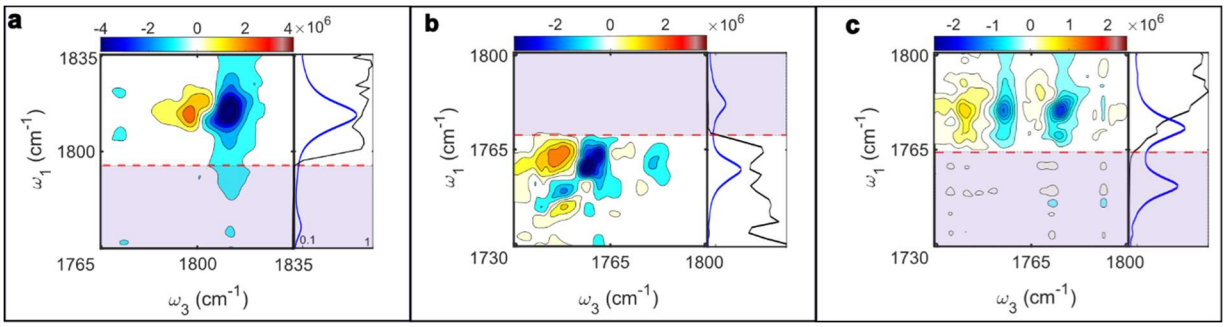

Figure 4.4.3-1: Pump-selective 2DIR spectra for : ^{0}EC **(a)**, ^{1}EC **(b)**, and ^{3}EC **(c)** plotted at t_2 = 1.5 ps. Normalized pump spectrum (black) and linear IR spectrum (blue) for each isotopologue are plotted to the right of each 2DIR spectrum. Red dashed line indicates cutoff where pump intensity drops below 10% of the maximum. Purple shaded regions indicate the unpumped region of each spectrum.

The 2DIR spectra plotted in figure 4.4.3-1 correspond to the set of pump selective experiments in which the Fermi active ring transition lies outside the pump bandwidth. We include the normalized pump spectra and linear IR spectra for each experiment to the right of each 2DIR spectrum in figure 4.4.3-1. The red dashed line indicates the frequency cutoff where pump intensity drops below 10% of the maximum, and the unpumped region is shaded purple. All spectra shown here were taken at t_2 = 1.5 ps. Under these experimental conditions, the bandwidth of the first two mid-IR pulses is limited such that the ring transition of the Fermi doublet cannot be directly excited. This eliminates secular response pathways which occupy the coherent superposition $|0\rangle\langle R|$ or its complex conjugate after interacting with the first pump pulse.[9,40] As such no intensity should be observed if $S_{R,C}$ is well described by secular dynamics. However, if coherence transfer of the type $|0\rangle\langle C| \rightarrow |0\rangle\langle R|$ redistributes vibrational energy from the excited carbonyl

fundamental to the ring during the t_1 interval, the now populated $|0\rangle\langle R|$ coherence appears as a bandwidth forbidden cross peak in the Fourier transformed signal. As such the observation of bandwidth forbidden peaks in pump-selective experiments serves as an additional check for the presence of coherence transfer pathways. While it is tempting to interpret the bandwidth forbidden regions of the spectra in figure 4.4.3-1 qualitatively, we find that it is often misleading due to experimental noise. We find it less ambiguous to identify evidence of coherence transfer pathways by comparing the intensity of the bandwidth forbidden features to the experimental noise over multiple t_2 steps.

Figure 4.4.3-2 gives the t_2 Fourier transform of the broadband $S_{R,C}$ cross peak kinetic trace ($F_{R,C}$) in (4.4.3-2**a**) and the bandwidth forbidden kinetic trace ($S^F{}_{R,C}$) in (4.4.3-2**b**).

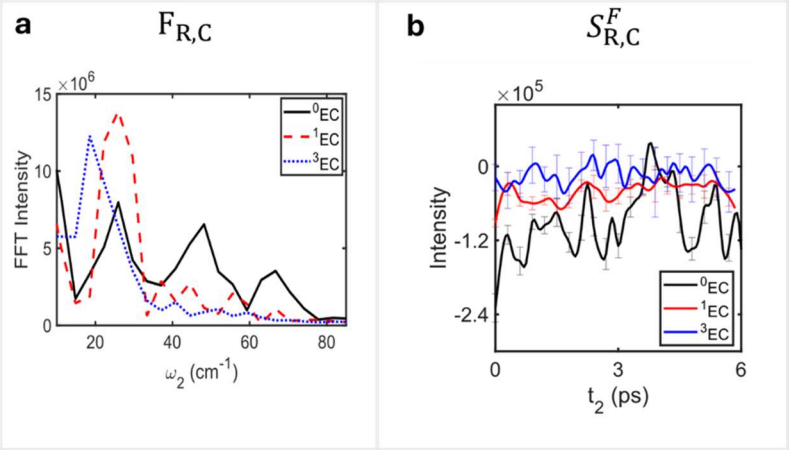

Figure 4.4.3-2. **(a)** Absolute value Fourier transform spectrum of the broadband 2DIR $S_{R,C}$ cross peak for ^{0}EC (black), ^{1}EC (red), and ^{3}EC (blue). **(b)** Kinetic trace for the bandwidth forbidden $S^F{}_{R,C}$ cross peaks. Error bars give the average detector noise for the pixels used to generate the kinetic trace. Integration regions for bandwidth forbidden peak are the same as for the broadband experiments shown in figure 3.

From figure 4.4.3-2**a** we see that the power spectrum ${}^{0}F_{R,C}$ contains at least three peaks centered near 26 cm^{-1}, 48 cm^{-1}, and 67 cm^{-1}. The 48 cm^{-1} peak agrees reasonably well with the frequency separation of the Fermi doublet, but the peaks at 26 cm^{-1} and 67 cm^{-1} serve as a positive test for the presence of coherent relaxation pathways. The spectrum of ${}^{1}F_{R,C}$ displays its most prominent peak at 26 cm^{-1}, which corresponds to the expected frequency separation of the doublet. Weak features in ${}^{1}F_{R,C}$ appear near 40 cm^{-1} and 60 cm^{-1}, although the low amplitude and potential influence of noise makes it difficult to take them as an unambiguous confirmation of coherent relaxation. If they truly reflect coherence transfer pathways, it seems they contribute only weakly relative to the main QB pathway. In the Fourier spectrum of ${}^{3}F_{R,C}$, significant intensity is only observed near the expected frequency difference of the Fermi doublet, indicating that no coherent relaxation pathways contribute to the cross peak. Thus, our first test indicates that inhibiting coupling to dark state manifolds, as evidenced by isotopic trends in vibrational lifetimes, suppresses the observation of coherent relaxation. However, it is not clear if our ability to resolve signatures of coherent relaxation from the spectra of figure 4.4.3-2**a** ends with ^{1}EC or ^{3}EC. For that, we gain some additional insight from the bandwidth forbidden kinetic traces of figure 4.4.3-2**b**.

The amplitude of the ${}^{0}S^{F}{}_{R,C}$ kinetic trace persists well above the noise level for the duration of the experimental time window, indicating non-trivial contributions from coherence transfer pathways. ${}^{1}S^{F}{}_{R,C}$ also shows non-negligible intensity to at least a few picoseconds, indicating that coherent relaxation pathways do contribute to the cross peak. As such, the 40 cm^{-1} and 60 cm^{-1} oscillations in ${}^{1}F_{R,C}$ should reflect the frequency spacing of the additional vibrational modes accessed by the non-secular pathway

contributing to the cross peak. In comparison, the bandwidth forbidden cross peak of ${}^{3}S^{F}{}_{R,C}$ fluctuates about the noise floor of the experiment, indicating no appreciable contributions from coherence transfer. Although analysis of such weak signals is necessarily qualitative, the agreement between the trends observed in $S^{F}{}_{R,C}$ and $F_{R,C}$ is reassuring. Under both methods for identifying coherent relaxation pathways, we observe weaker signatures of coherent relaxation upon increasing ^{13}C substitution. This strongly indicates that isotopic substitution provides an effective means for tuning coherent vibrational relaxation. Furthermore, we can reasonably attribute the suppression of coherent relaxation to the same mechanism responsible for slowing population relaxation in ^{1}EC and ^{3}EC, namely the decoupling of the Fermi doublet from a dark state manifold.

4.5 Conclusion

In this work we use 2DIR to compare the signatures of coherent vibrational relaxation for Fermi coupled vibrations across a series of EC isotopologues. We find that even though the resonance condition of the EC Fermi doublet increases upon isotopic substitution, the apparent rate of coherent relaxation is diminished. This isotopic trend is mirrored by an extension of the vibrational lifetimes of the Fermi doublet modes with increasing ^{13}C substitution. The suppression of both coherent and incoherent relaxation pathways indicates that they are similarly governed by manifold of dark states that become decoupled in the isotope substituted molecules. This is significant, as the dynamic information coherent relaxation processes encode in 2DIR spectra remains somewhat mysterious. Theoretical investigations comparing anharmonic couplings and coherent relaxation rates across isotopic series such as the EC series studied in this work may identify specific dark states or delocalized coupling networks that facilitate coherent

relaxation between IR-active transitions. Identifying the modes responsible for enabling coherent dynamics in closely related molecules would serve as an important step towards developing practical models for characterizing coherent relaxation pathways directly from 2DIR experiments.

References

(1) Cho, M. Molecular Photothermal Effects on Time-Resolved IR Spectroscopy. *The Journal of Chemical Physics* **2022**, *157* (12), 124201. https://doi.org/10.1063/5.0108826.

(2) Rubtsova, N. I.; Rubtsov, I. V. Vibrational Energy Transport in Molecules Studied by Relaxation-Assisted Two-Dimensional Infrared Spectroscopy. *Annual Review of Physical Chemistry* **2015**, *66* (Volume 66, 2015), 717–738. https://doi.org/10.1146/annurev-physchem-040214-121337.

(3) Schmitz, A. J.; Pandey, H. D.; Chalyavi, F.; Shi, T.; Fenlon, E. E.; Brewer, S. H.; Leitner, D. M.; Tucker, M. J. Tuning Molecular Vibrational Energy Flow within an Aromatic Scaffold via Anharmonic Coupling. *J. Phys. Chem. A* **2019**, *123* (49), 10571–10581. https://doi.org/10.1021/acs.jpca.9b08010.

(4) Hassani, M.; Mallon, C. J.; Monzy, J. N.; Schmitz, A. J.; Brewer, S. H.; Fenlon, E. E.; Tucker, M. J. Inhibition of Vibrational Energy Flow within an Aromatic Scaffold via Heavy Atom Effect. *The Journal of Chemical Physics* **2023**, *158* (22), 224201. https://doi.org/10.1063/5.0153760.

(5) Redfield, A. G. The Theory of Relaxation Processes*. In *Advances in Magnetic and Optical Resonance*; Waugh, J. S., Ed.; Advances in Magnetic Resonance; Academic Press, 1965; Vol. 1, pp 1–32. https://doi.org/10.1016/B978-1-4832-3114-3.50007-6.

(6) Hamm, P.; Zanni, M. *Concepts and Methods of 2D Infrared Spectroscopy*; Cambridge University Press: Cambridge, 2011. https://doi.org/10.1017/CBO9780511675935.

(7) *Vibrational States and Nitrile Lifetimes of Cyanophenylalanine Isotopomers in Solution | The Journal of Physical Chemistry A*. https://pubs.acs.org/doi/full/10.1021/acs.jpca.8b06300 (accessed 2024-10-18).

(8) Nishida, J.; Tamimi, A.; Fei, H.; Pullen, S.; Ott, S.; Cohen, S. M.; Fayer, M. D. Structural Dynamics inside a Functionalized Metal–Organic Framework Probed by Ultrafast 2D IR Spectroscopy. *Proc Natl Acad Sci U S A* **2014**, *111* (52), 18442–18447. https://doi.org/10.1073/pnas.1422194112.

(9) Marroux, H. J. B.; Orr-Ewing, A. J. Distinguishing Population and Coherence Transfer Pathways in a Metal Dicarbonyl Complex Using Pulse-Shaped Two-Dimensional Infrared Spectroscopy. *J. Phys. Chem. B* **2016**, *120* (17), 4125–4130. https://doi.org/10.1021/acs.jpcb.6b02979.

(10) Balzer, B.; Stock, G. Modeling of Decoherence and Dissipation in Nonadiabatic Photoreactions by an Effective-Scaling Nonsecular Redfield Algorithm. *Chemical Physics* **2005**, *310* (1), 33–41. https://doi.org/10.1016/j.chemphys.2004.10.001.

(11) Manzano, D. A Short Introduction to the Lindblad Master Equation. *AIP Advances* **2020**, *10* (2), 025106. https://doi.org/10.1063/1.5115323.

(12) Rose, P. A.; Krich, J. J. Efficient Numerical Method for Predicting Nonlinear Optical Spectroscopies of Open Systems. *The Journal of Chemical Physics* **2021**, *154* (3), 034108. https://doi.org/10.1063/5.0024104.

(13) Ishizaki, A.; Fleming, G. R. On the Adequacy of the Redfield Equation and Related Approaches to the Study of Quantum Dynamics in Electronic Energy Transfer. *The Journal of Chemical Physics* **2009**, *130* (23), 234110. https://doi.org/10.1063/1.3155214.

(14) Campaioli, F.; Cole, J. H.; Hapuarachchi, H. A Tutorial on Quantum Master Equations: Tips and Tricks for Quantum Optics, Quantum Computing and Beyond. arXiv March 29, 2023. https://doi.org/10.48550/arXiv.2303.16449.

(15) Khalil, M.; Demirdöven, N.; Tokmakoff, A. Vibrational Coherence Transfer Characterized with Fourier-Transform 2D IR Spectroscopy. *The Journal of Chemical Physics* **2004**, *121* (1), 362–373. https://doi.org/10.1063/1.1756870.

(16) Villaeys, A. A.; Liang, K. K. Description of Cross-Peaks Induced by Intermolecular Vibrational Energy Transfer in Two-Dimensional Infrared Spectroscopy. *Chemical Physics* **2015**, *450–451*, 12–20. https://doi.org/10.1016/j.chemphys.2015.01.010.

(17) Eckert, P. A.; Kubarych, K. J. Vibrational Coherence Transfer Illuminates Dark Modes in Models of the FeFe Hydrogenase Active Site. *The Journal of Chemical Physics* **2019**, *151* (5), 054307. https://doi.org/10.1063/1.5111016.

(18) Nee, M. J.; Baiz, C. R.; Anna, J. M.; McCanne, R.; Kubarych, K. J. Multilevel Vibrational Coherence Transfer and Wavepacket Dynamics Probed with Multidimensional IR Spectroscopy. *The Journal of Chemical Physics* **2008**, *129* (8), 084503. https://doi.org/10.1063/1.2969900.

(19) Baiz, C. R.; Kubarych, K. J.; Geva, E. Molecular Theory and Simulation of Coherence Transfer in Metal Carbonyls and Its Signature on Multidimensional Infrared Spectra. *J. Phys. Chem. B* **2011**, *115* (18), 5322–5339. https://doi.org/10.1021/jp109357d.

(20) Collini, E. Spectroscopic Signatures of Quantum-Coherent Energy Transfer. *Chemical Society Reviews* **2013**, *42* (12), 4932–4947. https://doi.org/10.1039/C3CS35444J.

(21) Pakoulev, A. V.; Rickard, M. A.; Mathew, N. A.; Kornau, K. M.; Wright, J. C. Frequency-Domain Time-Resolved Four Wave Mixing Spectroscopy of Vibrational Coherence Transfer with Single-Color Excitation. *J. Phys. Chem. A* **2008**, *112* (28), 6320–6329. https://doi.org/10.1021/jp711014h.

(22) Rickard, M. A.; Pakoulev, A. V.; Kornau, K.; Mathew, N. A.; Wright, J. C. Interferometric Coherence Transfer Modulations in Triply Vibrationally Enhanced Four-Wave Mixing. *J. Phys. Chem. A* **2006**, *110* (40), 11384–11387. https://doi.org/10.1021/jp063917e.

(23) Panitchayangkoon, G.; Voronine, D. V.; Abramavicius, D.; Caram, J. R.; Lewis, N. H. C.; Mukamel, S.; Engel, G. S. Direct Evidence of Quantum Transport in Photosynthetic Light-Harvesting Complexes. *Proceedings of the National Academy of Sciences* **2011**, *108* (52), 20908–20912. https://doi.org/10.1073/pnas.1105234108.

(24) Stenger, J.; Madsen, D.; Dreyer, J.; Nibbering, E. T. J.; Hamm, P.; Elsaesser, T. Coherent Response of Hydrogen Bonds in Liquids Probed by Ultrafast Vibrational Spectroscopy. *J. Phys. Chem. A* **2001**, *105* (13), 2929–2932. https://doi.org/10.1021/jp003153h.

(25) Scholes, G. D.; Fleming, G. R.; Chen, L. X.; Aspuru-Guzik, A.; Buchleitner, A.; Coker, D. F.; Engel, G. S.; van Grondelle, R.; Ishizaki, A.; Jonas, D. M.; Lundeen, J. S.; McCusker, J. K.; Mukamel, S.; Ogilvie, J. P.; Olaya-Castro, A.; Ratner, M. A.; Spano, F. C.; Whaley, K. B.; Zhu, X. Using Coherence to Enhance Function in Chemical and Biophysical Systems. *Nature* **2017**, *543* (7647), 647–656. https://doi.org/10.1038/nature21425.

(26) Engel, G. S.; Calhoun, T. R.; Read, E. L.; Ahn, T.-K.; Mančal, T.; Cheng, Y.-C.; Blankenship, R. E.; Fleming, G. R. Evidence for Wavelike Energy Transfer through Quantum Coherence in Photosynthetic Systems. *Nature* **2007**, *446* (7137), 782–786. https://doi.org/10.1038/nature05678.

(27) Rather, S. R.; Scholes, G. D. From Fundamental Theories to Quantum Coherences in Electron Transfer. *J. Am. Chem. Soc.* **2019**, *141* (2), 708–722. https://doi.org/10.1021/jacs.8b09059.

(28) Rather, S. R.; Bezdek, M. J.; Chirik, P. J.; Scholes, G. D. Dinitrogen Coupling to a Terpyridine-Molybdenum Chromophore Is Switched on by Fermi Resonance. *Chem* **2024**, *10* (3), 1028. https://doi.org/10.1016/j.chempr.2024.01.021.

(29) Chalyavi, F.; Schmitz, A. J.; Fetto, N. R.; Tucker, M. J.; Brewer, S. H.; Fenlon, E. E. Extending the Vibrational Lifetime of Azides with Heavy Atoms. *Phys. Chem. Chem. Phys.* **2020**, *22* (32), 18007–18013. https://doi.org/10.1039/D0CP02814B.

(30) Stuchebrukhov, A. A.; Marcus, R. A. Theoretical Study of Intramolecular Vibrational Relaxation of Acetylenic CH Vibration for V=1 and 2 in Large Polyatomic Molecules (CX3)3YCCH, Where X=H or D and Y=C or Si. *The Journal of Chemical Physics* **1993**, *98* (8), 6044–6061. https://doi.org/10.1063/1.464843.

(31) Sibert, E. L., III; Hynes, J. T.; Reinhardt, W. P. Classical Dynamics of Highly Excited CH and CD Overtones in Benzene and Perdeuterobenzene. *The Journal of Chemical Physics* **1984**, *81* (3), 1135–1144. https://doi.org/10.1063/1.447806.

(32) Ramos, S.; Scott, K. J.; Horness, R. E.; Sueur, A. L. L.; Thielges, M. C. Extended Timescale 2D IR Probes of Proteins: P-Cyanoselenophenylalanine. *Phys. Chem. Chem. Phys.* **2017**, *19* (15), 10081–10086. https://doi.org/10.1039/C7CP00403F.

(33) Prants, S. V. Quantum Dynamical Theory of a Fermi Resonance and Subpicosecond Spectroscopy of Coupled Vibrational Modes. *J. Phys. B: At. Mol. Opt. Phys.* **1988**, *21* (3), 397. https://doi.org/10.1088/0953-4075/21/3/008.

(34) Chisler, E. V.; Davydov, V. Yu.; Goncharuk, I. N.; Ivanova, E. A. On Fermi Resonance Theory. *physica status solidi (b)* **1976**, *78* (1), 359–370. https://doi.org/10.1002/pssb.2220780137.

(35) Gruebele, M.; Bigwood, R. Molecular Vibrational Energy Flow: Beyond the Golden Rule. *International Reviews in Physical Chemistry* **1998**, *17* (2), 91–145. https://doi.org/10.1080/014423598230117.

(36) Fujisaki, H.; Yagi, K.; Kikuchi, H.; Takami, T.; Stock, G. Vibrational Energy Transport in Acetylbenzonitrile Described by an *Ab Initio*-Based Quantum Tier Model. *Chemical Physics* **2017**, *482*, 86–92. https://doi.org/10.1016/j.chemphys.2016.09.010.

(37) Sibert, E. L., III; Reinhardt, W. P.; Hynes, J. T. Intramolecular Vibrational Relaxation and Spectra of CH and CD Overtones in Benzene and Perdeuterobenzene. *The Journal of Chemical Physics* **1984**, *81* (3), 1115–1134. https://doi.org/10.1063/1.447805.

(38) Bigwood, R.; Gruebele, M.; Leitner, D. M.; Wolynes, P. G. The Vibrational Energy Flow Transition in Organic Molecules: Theory Meets Experiment. *Proceedings of the National Academy of Sciences* **1998**, *95* (11), 5960–5964. https://doi.org/10.1073/pnas.95.11.5960.

(39) Zhang, J.; Wang, L.; Zhang, J.; Zhu, J.; Pan, X.; Cui, Z.; Wang, J.; Fang, W.; Li, Y. Identifying and Modulating Accidental Fermi Resonance: 2D IR and DFT Study of 4-Azido-l-Phenylalanine. *J. Phys. Chem. B* **2018**, *122* (34), 8122–8133. https://doi.org/10.1021/acs.jpcb.8b03887.

(40) Guerrieri, L.; Hall, S.; Luther, B. M.; Krummel, A. T. Signatures of Coherent Vibrational Dynamics in Ethylene Carbonate. *The Journal of Chemical Physics* **2024**, *161* (16), 164504. https://doi.org/10.1063/5.0216515.

(41) Bertran, J. F.; Ballester, L.; Dobrihalova, L.; Sánchez, N.; Arrieta, R. Study of Fermi Resonance by the Method of Solvent Variation. *Spectrochimica Acta Part A: Molecular Spectroscopy* **1968**, *24* (11), 1765–1776. https://doi.org/10.1016/0584-8539(68)80232-6.

(42) Al-Jallo, H. N.; Al-Azawi, F. N. Study of Fermi Resonance in Ethylene Carbonate by the Method of Isotopic Substitution. *Spectrochimica Acta Part A: Molecular Spectroscopy* **1978**, *34* (7), 819–823. https://doi.org/10.1016/0584-8539(78)80036-1.

(43) Schindler, W.; Zerda, T. W.; Jonas, J. High Pressure Raman Study of Intermolecular Interactions and Fermi Resonance in Liquid Ethylene Carbonate. *The Journal of Chemical Physics* **1984**, *81* (10), 4306–4313. https://doi.org/10.1063/1.447440.

(44) Fortunato, B.; Mirone, P.; Fini, G. Infrared and Raman Spectra and Vibrational Assignment of Ethylene Carbonate. *Spectrochimica Acta Part A: Molecular Spectroscopy* **1971**, *27* (9), 1917–1927. https://doi.org/10.1016/0584-8539(71)80245-3.

(45) Luther, B. M.; Tracy, K. M.; Gerrity, M.; Brown, S.; Krummel, A. T. 2D IR Spectroscopy at 100 kHz Utilizing a Mid-IR OPCPA Laser Source. *Opt. Express, OE* **2016**, *24* (4), 4117–4127. https://doi.org/10.1364/OE.24.004117.

(46) Luther, B. M.; Tracy, K. M.; Krummel, A. T. Demonstrating 100 kHz 2D IR Spectroscopy Using a Mid-IR OPCPA Laser Source. In *International Conference on Ultrafast Phenomena (2016), paper UTu2A.5*; Optica Publishing Group, 2016; p UTu2A.5. https://doi.org/10.1364/UP.2016.UTu2A.5.

(47) Guchhait, B.; Tibbetts, C. A.; Tracy, K. M.; Luther, B. M.; Krummel, A. T. Ultrafast Vibrational Dynamics of a Trigonal Planar Anionic Probe in Ionic Liquids (ILs): A Two-Dimensional Infrared (2DIR) Spectroscopic Investigation. *The Journal of Chemical Physics* **2020**, *152* (16), 164501. https://doi.org/10.1063/1.5141751.

(48) Shim, S.-H.; Zanni, M. T. How to Turn Your Pump–Probe Instrument into a Multidimensional Spectrometer: 2D IR and Vis Spectroscopiesvia Pulse Shaping. *Phys. Chem. Chem. Phys.* **2009**, *11* (5), 748–761. https://doi.org/10.1039/B813817F.

(49) Feng, Y.; Vinogradov, I.; Ge, N.-H. General Noise Suppression Scheme with Reference Detection in Heterodyne Nonlinear Spectroscopy. *Opt. Express, OE* **2017**, *25* (21), 26262–26279. https://doi.org/10.1364/OE.25.026262.

(50) Feng, Y.; Vinogradov, I.; Ge, N.-H. Optimized Noise Reduction Scheme for Heterodyne Spectroscopy Using Array Detectors. *Opt. Express, OE* **2019**, *27* (15), 20323–20346. https://doi.org/10.1364/OE.27.020323.

(51) Hochstrasser, R. M. Two-Dimensional IR-Spectroscopy: Polarization Anisotropy Effects. *Chemical Physics* **2001**, *266* (2), 273–284. https://doi.org/10.1016/S0301-0104(01)00232-4.

(52) Kondratyuk, P. Analytical Formulas for Fermi Resonance Interactions in Continuous Distributions of States. *Spectrochimica Acta Part A: Molecular and Biomolecular Spectroscopy* **2005**, *61* (4), 589–593. https://doi.org/10.1016/j.saa.2004.05.010.

(53) Devendorf, G. S.; Hu, M.-H. A.; Ben-Amotz, D. Pressure Dependent Vibrational Fermi Resonance in Liquid CH3OH and CH2Cl2. *J. Phys. Chem. A* **1998**, *102* (52), 10614–10619. https://doi.org/10.1021/jp983068y.

(54) Nejad, A.; A. Suhm, M.; E. Meyer, K. A. Increasing the Weights in the Molecular Work-out of Cis - and Trans -Formic Acid: Extension of the Vibrational Database via Deuteration. *Physical Chemistry Chemical Physics* **2020**, *22* (44), 25492–25501. https://doi.org/10.1039/D0CP04451B.

(55) Curnow, O. J.; Crittenden, D. L. Are “Bright-State” Models Appropriate for Analyzing Fermi-Coupled Bands in Molecular Vibrational Spectra? *J. Phys. Chem. A* **2021**, *125* (6), 1355–1358. https://doi.org/10.1021/acs.jpca.0c10404.

(56) Albert, S.; Hollenstein, H.; Quack, M.; Willeke, M. Rovibrational Analysis of the v 4,2v 6 Fermi Resonance Band of CH35ClF2 by Means of a Polyad Hamiltonian Involving the Vibrational Levels v 4, 2v 6,v 6+v 9 and 2v 9, and Comparison with Ab Initio Calculations. *Molecular Physics* **2006**, *104* (16–17), 2719–2735. https://doi.org/10.1080/00268970600828991.

(57) A. Tan, J.; Li, J.-W.; Chiu, C.; Liao, H.-Y.; Thi Huynh, H.; Kuo, J.-L. Tuning the Vibrational Coupling of H 3 O + by Changing Its Solvation Environment. *Physical Chemistry Chemical Physics* **2016**, *18* (44), 30721–30732. https://doi.org/10.1039/C6CP06326H.

Chapter 5
Conclusion and Future Work

5.1 Conclusions

The work presented in the previous chapters details efforts to identify coherent vibrational relaxation processes in ethylene carbonate (EC), explore the role of vibrational couplings in enabling coherent relaxation pathways, and assess the potential of isotopic substitution as a method for tuning coherent vibrational relaxation pathways. Chapter 3 primarily details the discovery of coherent relaxation processes in EC. The Feynman diagram representation of nonsecular response pathways was used to guide the identification of coherent relaxation using a combination of phase-matching dependent analysis of the 2DIR signal, Fourier-analysis of 2DIR peak amplitudes, and pump selective 2DIR experiments. Signatures of coherent relaxation appeared ubiquitously in the 2DIR spectrum, signaling EC's potential as a model system for studying coherent dynamics in small molecular systems. Interestingly, pump selective experiments indicated a possible link between the strength of resonance coupling and the significance of coherent relaxation. This observation partially motivated the work done in chapter 4, which examined the relationship between vibrational coupling and coherent dynamics explicitly. The study presented in chapter 4 explores the relationship between Fermi resonance coupling, dark state mediated vibrational energy redistribution, and the observation of coherent vibrational relaxation pathways in 2DIR spectra. Analysis of linear FTIR spectra quantified the resonance coupling parameters of the most intense Fermi doublet of EC and its ^{13}C isotopologues, with isotopic substitution leading to a

higher predicted rate of direct relaxation between the Fermi active modes. 2DIR analysis of population relaxation rates for the Fermi coupled modes revealed a competing trend, with isotopic substitution weakening vibrational coupling to intermediate states and extending the vibrational lifetimes of the Fermi coupled vibrations. The relative strengths of the direct and indirect relaxation mechanisms across the isotopic series were then compared to observed signatures of coherent relaxation in the 2DIR spectra of each isotopologue. Those results indicate a suppression of coherent dynamics upon increasing isotopic substitution, suggesting that the delocalization of vibrational relaxation pathways over intermediate states plays a more significant role than Fermi resonance coupling in enabling coherent vibrational energy transfer in EC. Notably, the 2DIR spectrum of triply ^{13}C substituted EC contained no discernable evidence of coherent relaxation processes, indicating that isotopic substitution could serve as a chemically accessible method for suppressing coherent relaxation in experimental investigations. Importantly, the ability to alter coherent vibrational relaxation using isotopic substitution could simplify identifying model compounds for the refinement of theoretical descriptions of coherent dynamics.

5.2 Future work: 2DIR Investigation of Carbonate Mixtures Containing EC

While the work presented in the previous chapters focuses on studying the vibrational dynamics of EC, the motivation for studying EC at all came from the desire to use the carbonyl stretch of organic carbonate molecules as probes in 2DIR investigations of the structure and dynamics of the organic electrolytes in energy storage devices. Developing a molecular level picture of the interactions between species within carbonate mixtures in bulk solutions would provide a foundation for understanding how components such as chemical additives, ionic species, or applied potentials restructure the solvent

and affect charge transport within and across electrochemical cells. However, 2DIR investigations of organic carbonate systems have been challenged by the degree of spectral complexity in multicomponent systems. The similarity in the frequencies of carbonyl transitions between different carbonates or between free and ion-coordinated species leads to 2DIR spectra with overlapping peaks whose t_2 evolution reports on multiple dynamical processes. For instance, 2DIR cross peaks between ion-coordinated and free carbonate molecules may receive amplitude from various phenomena such as chemical exchange,[1,2] vibrational coupling between solvent coordinated carbonates,[3] and vibrational energy transfer between molecules in different solvation shells.[4] Accurately extracting information from such complex spectra requires either detailed knowledge of the underlying physical processes contributing to each peak or the ability to isolate contributions from specific pathways.

One method which will likely prove useful in 2DIR investigations of bulk carbonate mixtures is isotopic substitution. This will be particularly true for investigations of mixtures containing EC. The discovery of coherent dynamics in EC, detailed in chapter 3, presents additional challenges. Coherent dynamics will distort[8–10] measurements of structural information in polarization selective 2DIR experiments[5–7] and complicate the interpretation of dynamical 2DIR observables. Chapter 4 demonstrated that isotopic substitution could suppress coherent relaxation in EC, making isotopologues such as ^{3}EC more attractive vibrational probes for the study of bulk carbonate mixtures. Additionally, investigations of bulk carbonate mixtures would benefit from the reduction in spectral congestion offered by isotopic substitution of different carbonate molecules. Preliminary FTIR and 2DIR experiments meant to assess the simplification of IR investigations of bulk

carbonate mixtures using isotopic substitution and a reduction in the number of components are presented in the remainder of this section. Preliminary data for three solutions of carbonate mixtures are described. The “1:1:1” solution consists of a mass equivalent mixture of EC, diethyl carbonate (DEC), and dimethyl carbonate (DMC). The second solution is a 1:1 by mass mixture of EC and DEC. The final solution is a 1:1 mixture of EC and a DEC isotopologue in which the carbonyl carbon was replaced by a ^{13}C molecule, which is denoted as ^{13}DEC in the following section.

5.2.1 Experimental Methods

Sample Preparation

All chemical samples were obtained from Sigma Aldrich, stored in a vacuum desiccator, and used without further purification. The three organic carbonate mixtures were prepared using equivalent mass ratios of the different carbonates. The first solution, denoted as the 1:1:1 mixture, comprised of EC, DEC, and DMC. The second solution contained only EC and DEC. The third solution was prepared by mixing equal masses of EC and a DEC isotopologue in which the carbonyl carbon was replaced by a ^{13}C molecule, which is denoted as ^{13}DEC in the following section. Samples were prepared using the same cells described in chapters 3 and 4; however, the samples presented in this chapter were prepared without using a Teflon spacer. Instead, spacer-free samples were prepared by pipetting approximately 1-3 μL of solution directly onto the (calcium fluoride) window. The volume of solution dispensed was used to control the absorption intensity of the samples.[11] Linear IR absorption spectra were collected using the same instrument described in chapters 3 and 4.

2DIR Data Collection

The 2DIR spectra presented in section 5.2.2 were collected using a 1 kHz 2DIR spectrometer[12] previously employed by the Krummel group. 2DIR measurements utilized a partly collinear heterodyned pump-probe geometry[13] and a home-built mid-IR pulse shaper. The mid-IR pulses used had a center frequency of 1760 cm^{-1} with a Gaussian FWHM bandwidth of 270 cm^{-1}. Because of the lower repetition rate, t_2 scan times were limited to approximately 1 ps. The t_1 scans ran from 0 ps to 6 ps in 15 fs steps. A four-frame phase cycling scheme[14] was employed alongside a 1400 cm^{-1} rotating frame. Fourier transform of the signal was done manually on a monochromator. A monochromator grating with groove density of 150 lines/mm was used to collect spectra for the 1:1:1 and EC:DEC solutions, while a 75 line/mm grating was used to collect spectra for the EC:^{13}DEC solution. The Fourier transformed signal was measured using a 64-element mercury cadmium telluride (MCT) array detector at 1 kHz (Infrared Systems). All phase cycled data sets were zero padded along t_1 to 802 points before being Fourier transformed into the frequency domain. Data were collected in both XXXX and XXYY polarization schemes in order to perform polarization dependent measurements, although the data presented here have been recombined to yield isotropic data sets.[15]

5.2.2 Linear IR and 2DIR Spectra of Organic Carbonate Mixtures

The linear IR spectra for the 1:1:1 (black), EC:DEC (cyan), and EC:^{13}DEC (magenta) mixtures are plotted in figure 5.2.2-1.

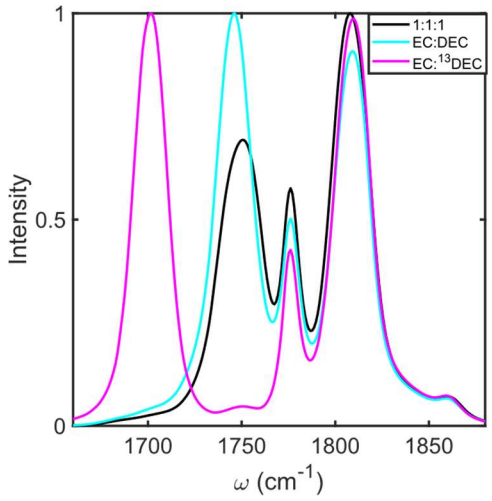

Figure 5.2.2-1: Normalized FTIR absorption spectra for the 1:1:1 (black), EC:DEC (cyan), and EC and EC:^{13}DEC (magenta) mixtures.

The linear spectra of the three carbonate mixtures demonstrate how reducing the number of components in the system and using isotopic substitution can reduce peak overlap in the carbonyl region. In all three mixtures, the EC ring mode and carbonyl transition are centered at 1776 cm^{-1} and 1808 cm^{-1}, respectively. In the 1:1:1 solution (black), the overlap between the DEC and DMC carbonyl stretching bands leads to a broad peak centered near 1750 cm^{-1}. The higher frequency side of the DEC+DMC peak appears to overlap with the EC peak at 1776 cm^{-1}, distorting its intensity. The DEC carbonyl transition appears as a single band at 1745 cm^{-1} in the EC:DEC mixture. Although the removal of DMC slightly alleviates overlap between the DEC peak and the EC peak at 1776 cm^{-1}, the overlap is not entirely removed. Isotopic substitution of the DEC carbonyl

shifts the center frequency of the DEC carbonyl stretch to 1701 cm^{-1}, significantly reducing the overlap between the DEC carbonyl and EC ring transitions. As such, isotopic substitution of the linear carbonates, DEC and DMC, will be necessary to fully resolve the EC doublet. This will be especially relevant for experiments utilizing EC isotopologues, such as those whose linear IR spectra are shown in chapter 4.

2DIR spectra contain additional excited state absorption peaks and cross peaks which increase spectral congestion compared to linear IR absorption spectra. Figure 5.2.2-2 shows the degree of spectral overlap in the 2DIR spectra, plotted for t_2 = 800 fs, of the 1:1:1 (**a**), EC:DEC (**b**), and EC:^{13}DEC (**c**) solutions.

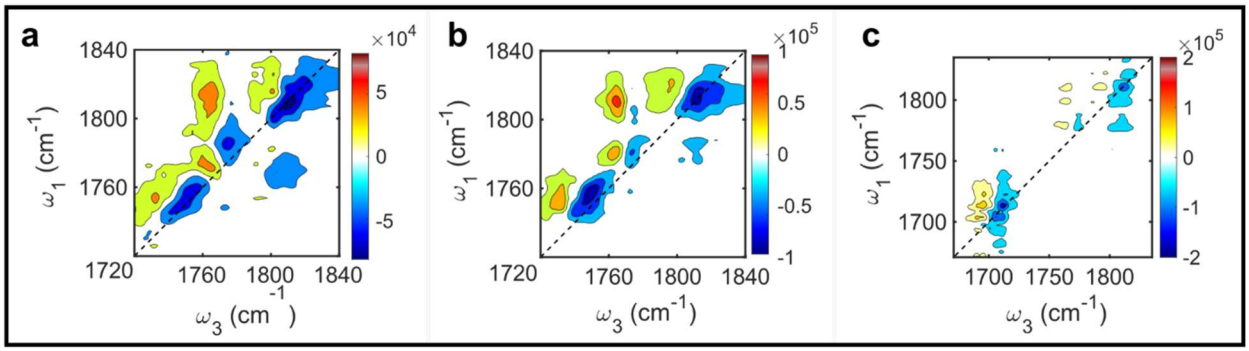

Figure 5.2.2-2: 2DIR spectra collected at t_2 = 800 fs for the **(a)** 1:1:1, (**b**) EC:DEC , and **(c)** EC:^{13}DEC solutions.

In the 1:1:1 solution (5.2.2-2**a**), the overlapping DEC and DMC band appears as an elongated pair of diagonal bleach and absorption features which appear to “blend” with the excited state absorption peak of the EC ring mode and nearby cross peak absorption. This leads to the distortion of the diagonal features in the lower frequency portion of the 1:1:1 spectrum. Furthermore, any cross peaks between the DEC and DMC carbonyl modes will be difficult to analyze due to overlapping with the broad diagonal feature. A

weak cross peak bleach appears near (ω_1, ω_3) = (1748 cm^{-1}, 1776 cm^{-1}) after 500 fs, indicating possible energy transfer pathways between the EC ring mode and the linear carbonates. However, the congested nature of the DEC and DMC band makes it difficult to assess whether one or both linear carbonates are involved in the relaxation pathway.

In comparison, the EC:DEC 2DIR spectrum (5.2.2-2**b**), shows less congestion on the lower frequency side of the spectrum, although the elongated diagonal bleach of the DEC carbonyl transition still extends to the diagonal peak pair of the EC ring mode, consistent with the overlap seen in the linear spectrum. The reduction in spectral congestion suggests it may be useful to use isotopic substitution of DMC to maximize the peak separation in future investigations of the 1:1:1 mixture, as DMC contributes to the higher frequency side of the DEC + DMC peak. It appears that a small cross peak between the EC ring and DEC carbonyl grows in by approximately 800 fs. 2DIR experiments with longer t_2 scan times could likely confirm the cross peak growth and extract rates of vibrational energy transfer between the two modes. Such measurements could then be used to assess possible chemical structures of the EC:DEC mixture, based on the fact that DEC exchanges energy with the EC ring rather than the carbonyl.

Isotopic substitution of DEC leads to the 2DIR spectrum shown in figure 5.2.2-2**c**. In this system, the overlap between the EC and DEC bands is removed. No cross peaks are observed between DEC and EC over the 1.4 ps time interval of the experiment. This indicates that vibrational energy transfer could be inhibited due to the frequency detuning of the DEC carbonyl mode from the EC ring. The downshifting of the DEC peak could prove useful not only for studying mixtures of three or more carbonates, but also for assessing the interactions between DEC and DMC. Isotopic substitution of either DMC or

DEC may resolve cross peaks between DEC and DMC. Such cross peaks could be used to extract the transition dipole angle between the carbonyl stretches of the two linear carbonates. Comparing that angle with and without the addition of EC would serve to identify whether EC perturbs the chemical structure of the linear carbonate systems.

The preliminary data in this section demonstrates how the complex 1:1:1 mixture can be broken down, either piecewise or through isotopic substitution, to remove spectral congestion and isolate peaks in the 2DIR spectrum. The discovery of coherent relaxation processes in EC solvated by THF suggests that isotopic substitution of EC could further simplify analysis of polarization selective 2DIR experiments for organic carbonate solutions. Notably, fully deuterated EC has been found to lack a Fermi resonance in the carbonyl region,[16] which would reduce congestion and potentially eliminate coherent relaxation pathways. Ultimately, combinations of carbonate isotopologues may be needed to remove both spectral congestion and coherent relaxation pathways from the 2DIR spectra of organic carbonate mixtures.

References

(1) Lee, K.-K.; Park, K.; Lee, H.; Noh, Y.; Kossowska, D.; Kwak, K.; Cho, M. Ultrafast Fluxional Exchange Dynamics in Electrolyte Solvation Sheath of Lithium Ion Battery. *Nat Commun* **2017**, *8* (1), 14658. https://doi.org/10.1038/ncomms14658.

(2) Dereka, B.; Lewis, N. H. C.; Zhang, Y.; Hahn, N. T.; Keim, J. H.; Snyder, S. A.; Maginn, E. J.; Tokmakoff, A. Exchange-Mediated Transport in Battery Electrolytes: Ultrafast or Ultraslow? *J. Am. Chem. Soc.* **2022**, *144* (19), 8591–8604. https://doi.org/10.1021/jacs.2c00154.

(3) Fulfer, K. D.; Galle Kankanamge, S. R.; Chen, X.; Woodard, K. T.; Kuroda, D. G. Elucidating the Mechanism behind the Infrared Spectral Features and Dynamics Observed in the Carbonyl Stretch Region of Organic Carbonates Interacting with Lithium Ions. *The Journal of Chemical Physics* **2021**, *154* (23), 234504. https://doi.org/10.1063/5.0049742.

(4) Lim, C.; Jeon, J.; Park, K.; Liang, C.; Chae, Y.; Kwak, K.; Cho, M. Revisiting Ultrafast Dynamics in Carbonate-Based Electrolytes for Li-Ion Batteries: Clarifying 2D-IR Cross-Peak Interpretation. *J. Phys. Chem. B* **2023**, *127* (44), 9566–9574. https://doi.org/10.1021/acs.jpcb.3c05480.

(5) Krummel, A. T.; Zanni, M. T. DNA Vibrational Coupling Revealed with Two-Dimensional Infrared Spectroscopy: Insight into Why Vibrational Spectroscopy Is Sensitive to DNA Structure. *J. Phys. Chem. B* **2006**, *110* (28), 13991–14000. https://doi.org/10.1021/jp062597w.

(6) Kramer, P. L.; Nishida, J.; Giammanco, C. H.; Tamimi, A.; Fayer, M. D. Observation and Theory of Reorientation-Induced Spectral Diffusion in Polarization-Selective 2D IR Spectroscopy. *The Journal of Chemical Physics* **2015**, *142* (18), 184505. https://doi.org/10.1063/1.4920949.

(7) Hochstrasser, R. M. Two-Dimensional IR-Spectroscopy: Polarization Anisotropy Effects. *Chemical Physics* **2001**, *266* (2), 273–284. https://doi.org/10.1016/S0301-0104(01)00232-4.

(8) Khalil, M.; Demirdöven, N.; Tokmakoff, A. Vibrational Coherence Transfer Characterized with Fourier-Transform 2D IR Spectroscopy. *The Journal of Chemical Physics* **2004**, *121* (1), 362–373. https://doi.org/10.1063/1.1756870.

(9) Villaeys, A. A.; Liang, K. K. Description of Cross-Peaks Induced by Intermolecular Vibrational Energy Transfer in Two-Dimensional Infrared Spectroscopy. *Chemical Physics* **2015**, *450–451*, 12–20. https://doi.org/10.1016/j.chemphys.2015.01.010.

(10) Chuntonov, L.; Ma, J. Quantum Process Tomography Quantifies Coherence Transfer Dynamics in Vibrational Exciton. *J. Phys. Chem. B* **2013**, *117* (43), 13631–13638. https://doi.org/10.1021/jp4075493.

(11) Lim, C.; Kim, J. H.; Chae, Y.; Lee, K.-K.; Kwak, K.; Cho, M. Solvation Structure around Li+ Ions in Organic Carbonate Electrolytes: Spacer-Free Thin Cell IR Spectroscopy. *Anal. Chem.* **2021**, *93* (37), 12594–12601. https://doi.org/10.1021/acs.analchem.1c02127.

(12) Christopher Thomas Kuhs. INVESTIGATING MOLECULAR INTERACTIONS CONTRIBUTING TO SELF-ASSEMBLY ON ULTRAFAST TIME SCALES WITH TWO-DIMENSIONAL INFRARED SPECTROSCOPY. PhD, Colorado State University, Fort Collins, Colorado, 2019. https://api.mountainscholar.org/server/api/core/bitstreams/8d0262fb-33f6-4048-a1f5-4a01a2e4c705/content.

(13) Shim, S.-H.; Zanni, M. T. How to Turn Your Pump–Probe Instrument into a Multidimensional Spectrometer: 2D IR and Vis Spectroscopiesvia Pulse Shaping. *Phys. Chem. Chem. Phys.* **2009**, *11* (5), 748–761. https://doi.org/10.1039/B813817F.

(14) Nishida, J.; Tamimi, A.; Fei, H.; Pullen, S.; Ott, S.; Cohen, S. M.; Fayer, M. D. Structural Dynamics inside a Functionalized Metal–Organic Framework Probed by Ultrafast 2D IR Spectroscopy. *Proc Natl Acad Sci U S A* **2014**, *111* (52), 18442–18447. https://doi.org/10.1073/pnas.1422194112.

(15) Park, J. Y.; Mondal, S.; Kwon, H.-J.; Sahu, P. K.; Han, H.; Kwak, K.; Cho, M. Effect of Isotope Substitution on the Fermi Resonance and Vibrational Lifetime of Unnatural Amino Acids Modified with IR Probe: A 2D-IR and Pump-Probe Study of 4-Azido-L-Phenyl Alanine. *The Journal of Chemical Physics* **2020**, *153* (16), 164309. https://doi.org/10.1063/5.0025289.

(16) Al-Jallo, H. N.; Al-Azawi, F. N. Study of Fermi Resonance in Ethylene Carbonate by the Method of Isotopic Substitution. *Spectrochimica Acta Part A: Molecular Spectroscopy* **1978**, *34* (7), 819–823. https://doi.org/10.1016/0584-8539(78)80036-1.

Appendix A

Supplementary Material for Chapter 3: Signatures of Coherent Vibrational in Ethylene Carbonate

A.1 Gaussian Fit to Linear Spectrum

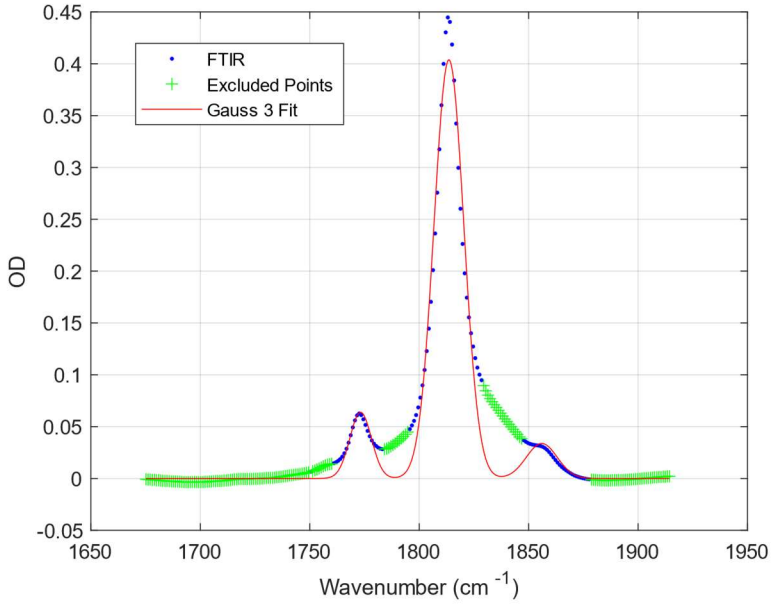

Figure. A1: Gaussian fits to the linear spectrum of EC in THF (blue) for three modes. Broad background was excluded (green +) from the Gaussian fit (red).

To approximate the linewidth of the three bands at 1773 cm^{-1}, 1813 cm^{-1} and 1858 cm^{-1}, we fit the linear spectrum to three gaussians and excluded the broad baseline from the fit. Fitting was performed with the MATLAB 2023b Curve Fitting Toolbox. The results of our fit returns FWHM parameters of 11.7 cm^{-1}, 16.0 cm^{-1}, and 16.6 cm^{-1} respectively. Fitting this way is highly sensitive to the exclusion parameters, and the

results give only approximate linewidth values. Still, it provides an estimate of peak widths and their relative intensities. Integrating the fits for each peak gives a ν_2: $2\nu_7$ ratio of 8.7:1 and 11.5:1 for ν_2: $\nu_7 + \nu_6$.

A.2 Quantifying the Noise Floor for 2DIR Experiments

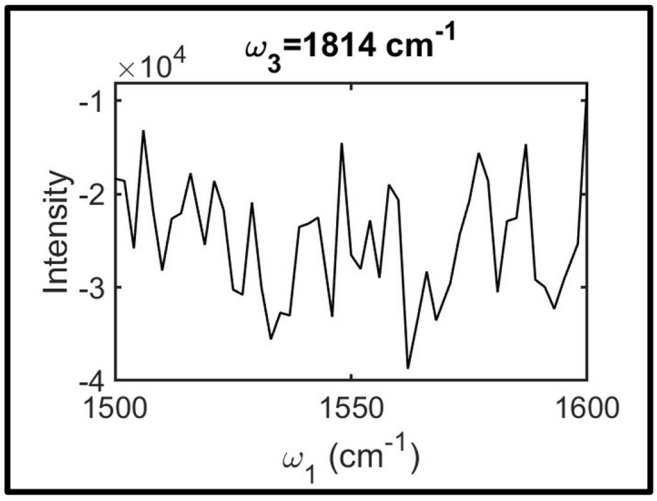

Figure A2: Raw noise intensity along the ω_1 axis for the pixel of maximum signal. Corresponds to data set with $t_1$scan 0:8 ps and full pump bandwidth.

To quantify the impact of noise on a given t_2 waiting step, we take the mean of the absolute value of the spectrum for the maximum signal (ω_3=1814 cm^{-1}) pixel over the range of ω_1=1500-1600 cm^{-1}. This serves as the noise floor for each experiment. An example plot of the raw noise is given in figure A2. The noise floor for each experiment presented in the main text is given in table A1.

Table A1: Pump bandwidth, t_1 scan parameters, and calculated noise floor of the maximum signal pixel for each experiment presented in the main text.

t_1 scan time	0:3 ps	0:10 ps			0:8 ps		
Pump bandwidth	Full	>1795 cm^{-1}	Full	<1831 cm^{-1}	<1815 cm^{-1}	Full	>1816 cm^{-1}
Mean noise	2.50E+05	1.20E+05	1.70E+05	8.40E+04	7.80E+03	2.5E+04	1.80E+04

We use this metric to test the impact of noise on our interpretation of fluctuations in the amplitudes of peaks in the 2DIR spectrum. To separate the oscillations from vibrational lifetime decay, we rearrange equation 3 of the main text, yielding

(A-1) $$\langle \delta\omega(t_2)^2 \rangle = \frac{(A_R + A_{NR})\sqrt{1-\bar{C}(t_2)^2}}{\pi e^{\frac{-t_2}{T_1}}}.$$

For convenience we redefine this quantity as $\phi = \langle \delta\omega(t_2)^2 \rangle$. We then remove the constant offset and normalize the fluctuation amplitude according to

(A-2) $$\bar{\phi}(t_2) = \frac{\phi(t_2) - \langle \phi(t_2) \rangle}{\max(\phi(t_2))}.$$

This value is plotted in figure A3 for the ν_2 diagonal bleach. The error bars in figure A3 give the pixel noise for each t_2 waiting step, normalized to the maximum intensity of the feature in the 2DIR spectrum. From this we see that the oscillations in peak intensity persist well above the noise floor of the experiment. The lack of a clear dampening in figure A3 prevents us from fitting the oscillatory components to damped exponentials.

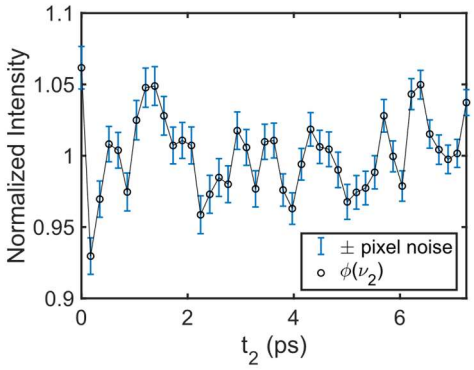

Figure A3: Fluctuations of the ν_2 diagonal bleach compared to the pixel noise at each t_2 point. The noise intensity was normalized to the maximum intensity of the signal. Data shown in this figure corresponds to the data set presented in figure 3.5.2-1 of the main text.

A.3 Diagonal Peak Sensitivity to Pump Selective Experiments

Here we test the effects of pump selective experiments on the kinetic traces of features totally within the pump bandwidth. We focus on the measured vibrational lifetimes of the ν_2 diagonal bleach and absorption under three pump selective conditions. The kinetic traces from 0 to 3 ps are plotted in figure A4, and the time constants of the fits are given in table A2. Traces out to 6 ps were fit to biexponential decays of the form $a_1 e^{\frac{-t_2}{\tau_{fast}}} + a_2 e^{\frac{-t_2}{\tau_{slow}}}$. For the diagonal bleach [figure A4(**a**)] the fit results are unaffected by the pump bandwidth.

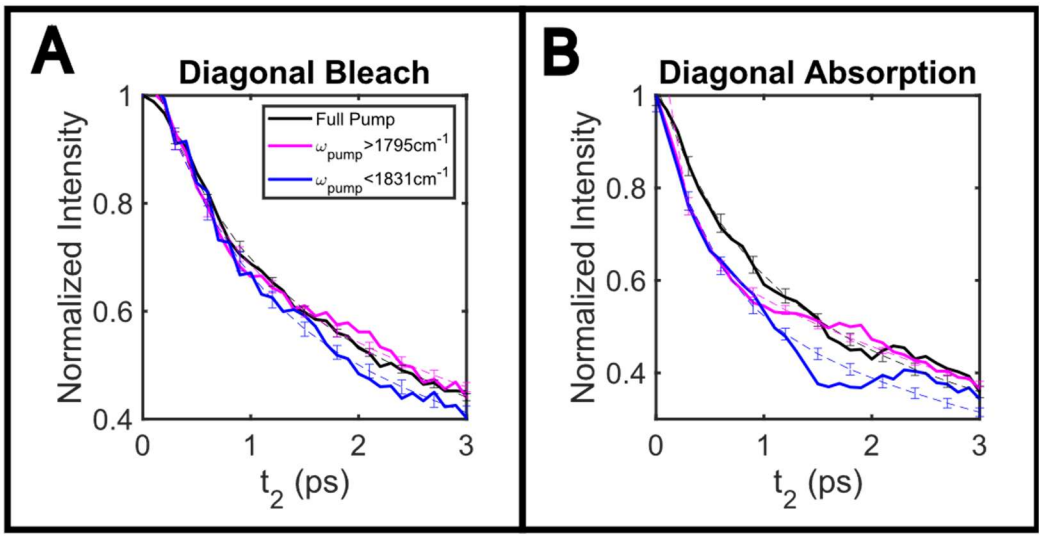

Figure A4: Normalized integrated intensities (solid) and fits (dashed) of the diagonal bleach (**a**) and absorption (**b**) of the ν_2 fundamental transition under ordinary (black), $\omega_{pump} > 1795$ cm^{-1} (magenta), and $\omega_{pump} < 1831$ cm^{-1} (blue) conditions. Error bars give the 95% confidence interval of the fit out to 6 ps.

Qualitatively we see small deviations in the beating pattern after approximately 1.8 ps, but they do not alter the fit. As the kinetic trace for the diagonal bleach remains insensitive to pump selective conditions, we do not ascribe the changes in dynamics to changes in the temporal profile of the pump pulses.

Table A2: Time constants for the biexponential fits to the kinetic traces of the ν_2 diagonal bleach and absorption under different pump selective conditions.

	Bleach		**Absorption**	
Pump Condition	τ_{fast}	τ_{slow}	τ_{fast}	τ_{slow}
Full	0.5±0.1 ps	7.1±0.8 ps	0.5±0.2 ps	7.2±2.0 ps
ω_{pump}>1795 cm^{-1}	0.4±0.1 ps	8.3±0.9 ps	0.2±0.0 ps	6.9±0.7 ps
ω_{pump}<1831 cm^{-1}	0.4ps±0.1ps	7.7±1.13 ps	0.4±.2 ps	7.1±2.2 ps

For the diagonal absorption, we see a significant reduction in the short time constant when the pump bandwidth is limited to: ω_{pump}>1795 cm^{-1}. This is apparently due to a positive going oscillation which appears earlier compared to the other two kinetic traces in figure A4(**b**). The variation in the oscillatory character of the peaks under different pump selective experiments reflect the complicated nature of systems which may exhibit both CVET and ordinary quantum beating. The long-time constants for both the bleach and absorption under all conditions are within error, indicating that CVET most significantly impacts dynamical measurements at early waiting times. It also suggests that in systems with a broad network of CVET pathways, early time dynamical measurements are sensitive to pump bandwidth. Care should be taken to account for oscillatory contributions or to maintain consistent pump bandwidths when comparing data sets for highly coupled systems that display wave-packet like dynamics.

A.4 Comparing Ordinary and Forbidden Cross Peaks as a Function of t_1 Scan Length

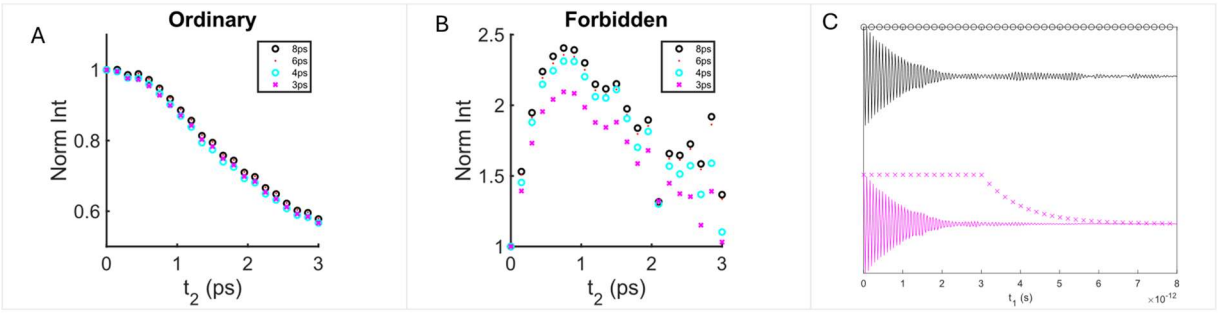

Figure A5: Comparing the integrated intensity of the cross peak at (ω_1, ω_3)=(1831 cm^{-1},1814 cm^{-1}) using different window functions (exponential decay with a step function) applied to raw data along t_1. Dotted lines correspond to the time (ps) at which an exponential window was applied to the t_1 data. Kinetic traces in (**a**) and (**b**) were normalized to their initial intensity. **(a)** Normalized intensity of the ordinary cross peak. **(b)** Normalized intensity of the bandwidth forbidden cross peak. **(c)** Data on signal pixel along t_1 (seconds) (solid) and applied window functions for no window (black) and the exponential decay applied after 3ps (magenta). Raw data presented for ordinary pump bandwidth.

To test the t_1 scan sensitivity of forbidden cross peaks, we compare the integrated intensities of the (ω_1, ω_3)=(1831 cm^{-1},1814 cm^{-1}) ordinary (figure A5(**a**)) and forbidden (figure A5(**b**)) cross peak using different window functions. We apply an exponential decay with different cutoffs to the time domain data, mimicking the effect of varying t_1 scan time. Figure A5(**c**) gives examples of the time domain data (solid) for an 8 ps (black) and 3 ps (magenta) window cutoff as well as the corresponding window function (dots). The 8 ps cutoff represents data with no applied window function. The time domain data with no window in figure A5(**c**) shows an initial decrease in intensity followed by the appearance of new features at approximately 4 ps. As seen in figure A5(**a**), the window function minimally impacts the relative intensity of the ordinary cross peak at each t_2 step. The normalized intensities diverge by less than 3% over the first 3 ps of waiting time. The same cross peak, when bandwidth forbidden, shows a much greater sensitivity to the

effective t_1 scan time. In this case the normalized intensities diverge by up to 11%. This demonstrates not only that the features seen after approximately 4 ps in figure A5(**c**) are a signature of CVET, but also that the observation of CVET in 2DIR spectra is sensitive to t_1 scan time.

A.5 Biexponential Time Constants for Diagonal and Cross Peak Kinetic Traces

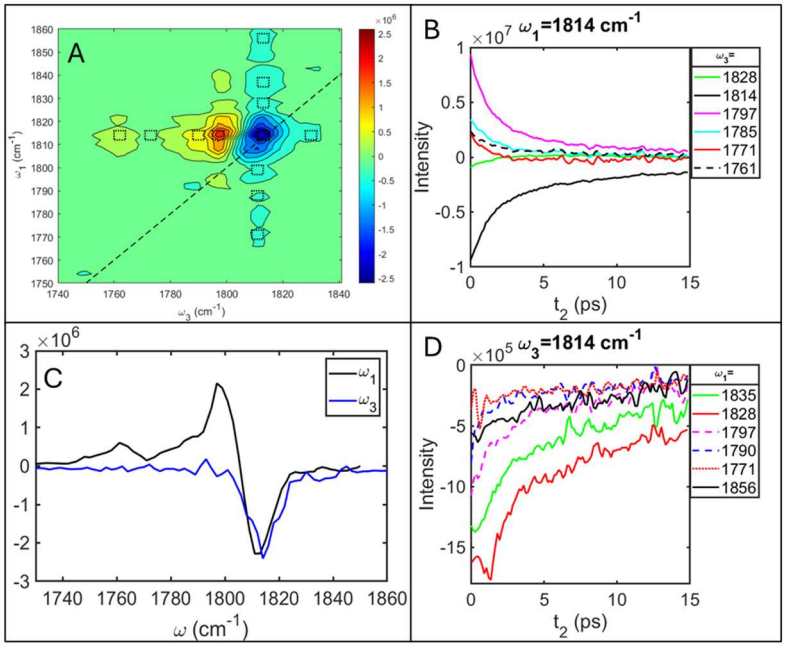

Figure A6: **(a)** 2DIR spectrum plotted with integration regions (dotted black) for the diagonal and cross peaks fit to biexponential decays. **(b)** Integrated intensities of peaks along the ω_3 axis. **(c)** Slices taken along the ω_1 (black) and ω_3 (blue) axes. Slices were taken at ω=1814 cm^{-1}. **(d)** Integrated intensities of cross peaks along the ω_1 axis.

We present the integration regions [figure A6(**a**)], slices along frequency axes [figure A6(**c**)], and kinetic traces [figure A6(**b**,**d**)] to a selection of cross peaks in the 2DIR spectrum of EC in THF. Tables A3 and A4 provide time constants for

fitted biexponential decays to the kinetic traces in figure A6. At present we do not engage in further analysis of the diagonal and cross peak dynamics but include them as references for future 2DIR studies of ethylene carbonate.

Table A3: Time constants of biexponential fits for cross peaks centered near ω_3=1814 cm^{-1}. The 95% confidence interval of the fit is given in parentheses.

ω_1 Cross Peak Biexponential Decay Time Constants		
ω_1	**τ_1 (ps)**	**τ_2 (ps)**
1856 cm^{-1}	1.2 (-0.66, 3.16)	14.7 (11.1, 18.3)
1835 cm^{-1}	1.8 (1.3, 2.4)	16.7 (12.8, 20.6)
1828 cm^{-1}	3.3 (2.6, 4.0)	28.7 (18.3, 39.0)
1797 cm^{-1}	1.5 (1.0, 2.0)	13.8 (10.4, 17.2)
1790 cm^{-1}	0.8 (0.5, 1.1)	14.8 (11.8, 17.8)

1771 cm^{-1}	0.7 (0.3, 1.1)	25.6 (18.1, 33.1)

Table A4: Time constant of biexponential fits for cross peaks centered near ω_1=1814 cm^{-1}. The 95% confidence interval of the fit is given in parentheses.

ω_3 Cross Peak Biexponential Decay Time Constants		
$\boldsymbol{\omega_3}$	τ_1 (ps)	τ_2 (ps)
1828 cm^{-1}	1.9 (1.4, 2.3)	6.3 (3.5,9.0)
1814 cm^{-1}	1.35 (1.3, 1.4)	14.9 (14.2, 15.6)
1797 cm^{-1}	1.3 (1.2, 1.4)	9.9 (9.0, 10.9)
1785 cm^{-1}	1.4 (1.2, 1.7)	9.1 (5.2, 13.0)
1771 cm^{-1}	1.3 (1.0, 1.6)	13.9 (2.0, 25.7)
1761 cm^{-1}	1.2 (0.8, 1.5)	12.2 (7.5, 16.9)

A.6 Single Coherence Transfer Feynman Diagrams

In this section we provide additional Feynman diagrams generated by incorporating single coherence transfer steps in secular response pathways. These pathways follow the same conventions as those described in the main text. We use these pathways to assess the possible (ω_1, ω_3) positions of coherence transfer contributions to pump selective 2DIR spectra. The heading of each set of diagrams corresponds to the secular pathways.

Stimulated Emission (SE)

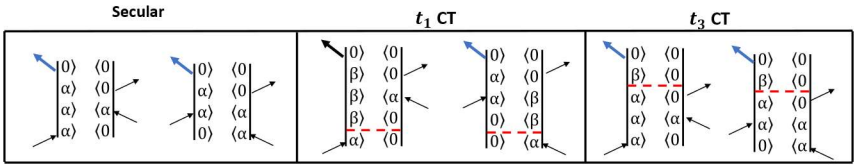

Ground State Bleach

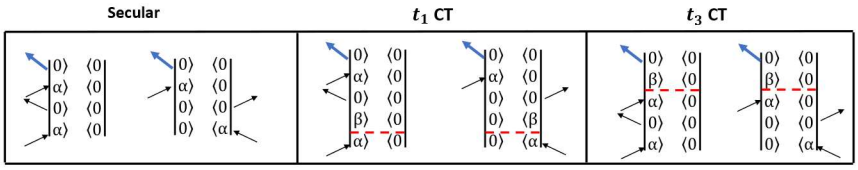

Excited State Absorption (ESA)

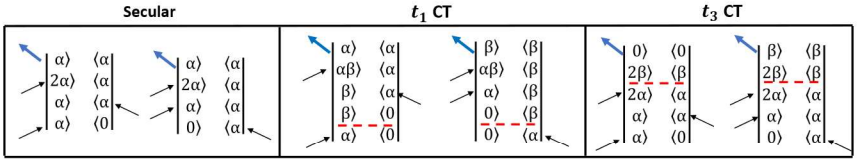

Population Transfer SE

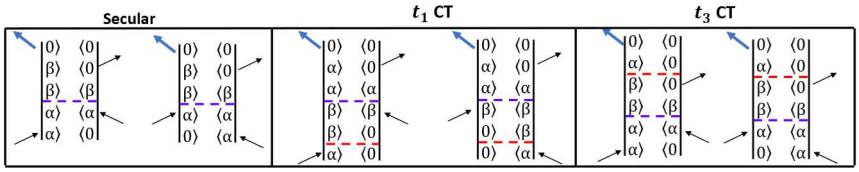

Population Transfer ESA

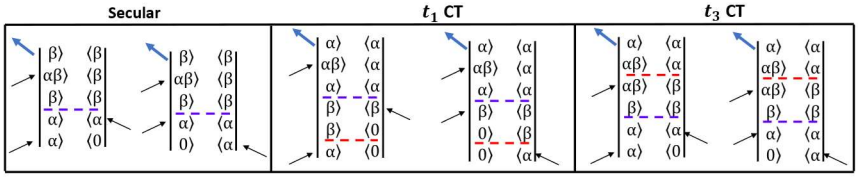

Cross Peak Bleach

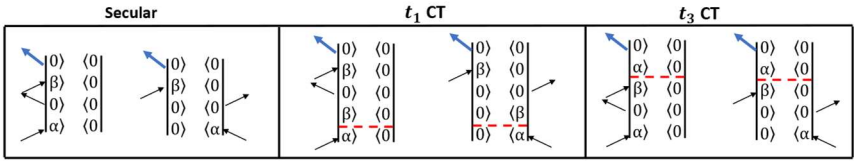

Cross Peak ESA

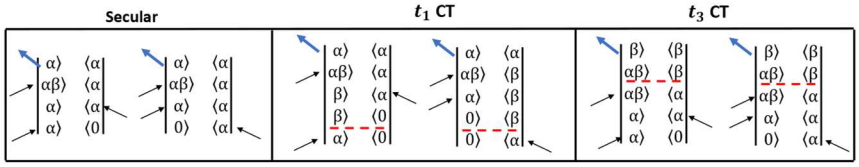

Quantum Beat SE

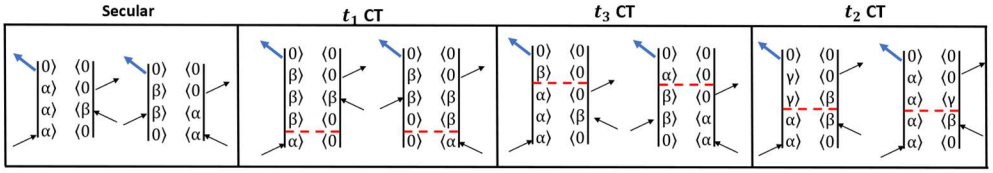

Quantum Beat ESA

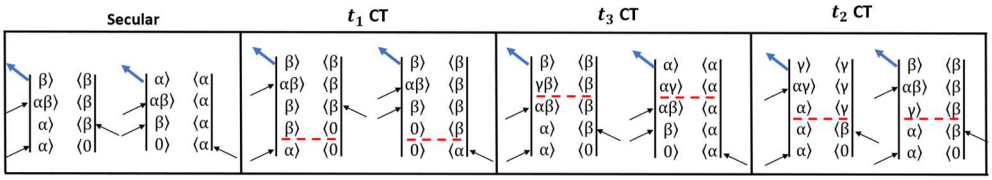

A 7. Excitation Energy Dependence of EC Spectral Features

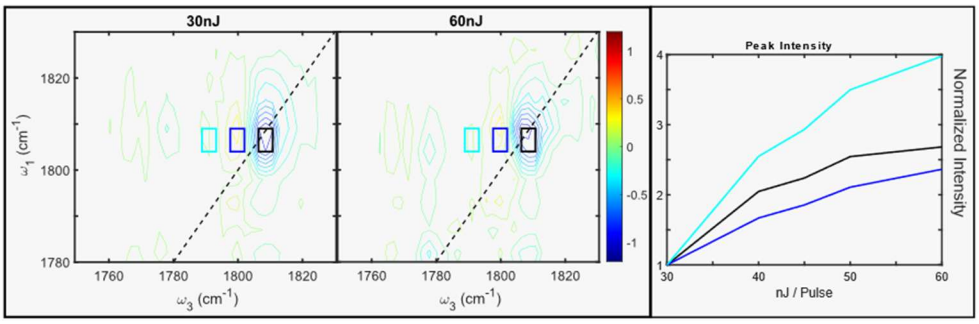

Figure A7. Purely absorptive 2DIR of EC: dimethyl carbonate mixture diluted in acetonitrile taken with excitation energy of (**left**) 30 nJ/ pulse and (**middle**) 60 nJ/pulse. Colored rectangles indicate regions of integration. (**right.)** Peak intensity vs. excitation energy (nJ/pulse) for the highlighted regions of the 2DIR spectrum.

To assess whether vibrational ladder climbing pathways contributed to the observation of anomalous peaks and oscillations in peak intensities in the 2DIR spectrum of EC, we performed a series of excitation pulse energy dependent measurements on of a 1:1 molar mixture of EC and dimethyl carbonate diluted in acetonitrile. In these experiments, we held the energy per probe pulse to 35 nJ and varied the excitation pulse energy from 30-60 nJ / pulse. All spectra were collected at zero waiting time. In figure A7 we plot the 2DIR spectra for the 30 (left) and 60 (middle) nJ / pulse experiments, as well as the integrated intensities (right) of the diagonal bleach (black), the diagonal absorption (dark blue), and the additional absorption band (light blue) appearing as a shoulder in both the EC: dimethyl carbonate mixture and in EC dissolved in THF. If vibrational ladder climbing pathways contribute to features of the EC spectra, we expect the intensities of the features to scale quadratically scaling of the 2DIR signal intensity with the excitation

energy. Over the range of excitation energies tested, we do not observe a quadratic relationship between excitation pulse energy and 2DIR signal intensity for any of the measured peaks. As such, we cannot ascribe the additional ESA peak or oscillations in the 2DIR peak intensities to contamination by higher order signals. Although this system is not identical to that described in the main text, we do not believe that EC dissolved in THF will show a greater proclivity for vibrational ladder climbing.

A.8 Real Rephasing Coherence Map for ω_2 = 41 cm^{-1}

To ensure that accidental overlap between diagonal and cross peaks is not responsible for the oscillations observed in 3.5.2-2(**e**) of the main text, we examine the coherence map for the data plotted in 3.5.2-2 of the main text. The coherence map given in figure A8 was generated by subtracting an exponential fit to each (ω_1, ω_3) position in the real rephasing spectrum. The residual was then Fourier transformed about t_2 to generate a coherence map. In figure A8 we plot the self-normalized coherence map for ω_2 = 41 cm^{-1} which is the difference frequency between the fundamental and Fermi resonance band. If the 41 cm^{-1} oscillation observed in 3.5.2-2 (**e**-**f**) of the main text arose due to accidental overlap between broad peaks, we would expect the oscillation to appear delocalized in figure A8; however, that is not the case. Even in the real rephasing signal, where QB pathways are only expected to contribute to cross peaks, the 41 cm^{-1} oscillation appears localized on the diagonal peaks. The lack of a broad background feature in figure A8 indicates that accidental overlap is not responsible for the oscillations of the 2DIR peak

intensities examined in the main text. Rather, it appears that oscillations at this frequency involve a select subset of peaks in the 2DIR spectrum.

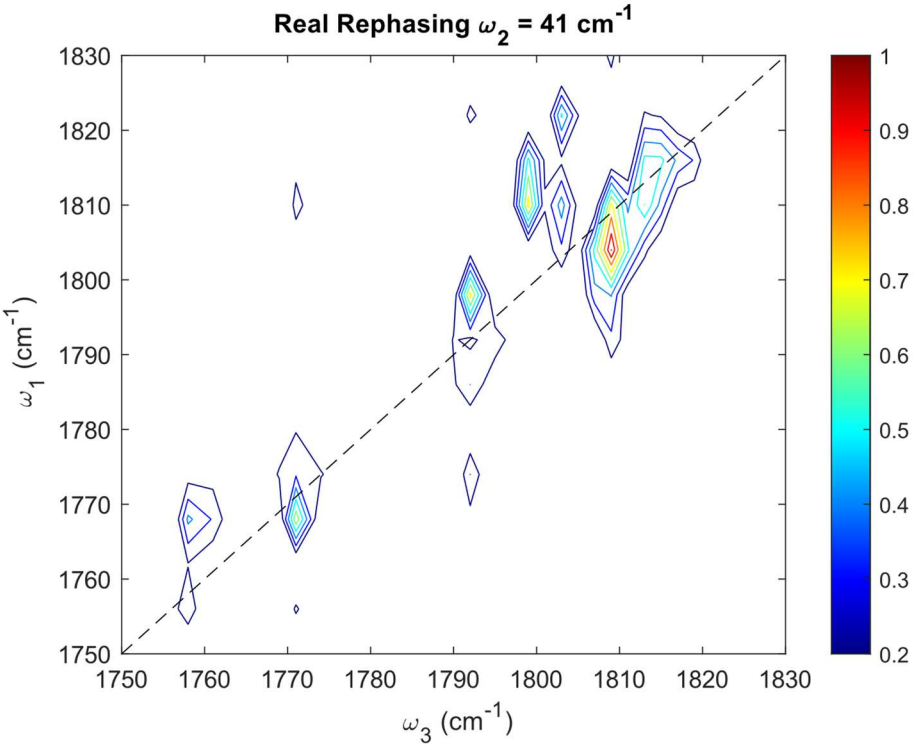

Figure A8: Self-normalized coherence map for the real rephasing spectrum, taken at ω_2 = 41 cm^{-1}

Appendix B

MATLAB code for extracting rephasing and nonrephasing signals from 2DIR data

```
clear all, hold off, close all
```

Input parameters

```
%Time domain (tau) axis parameters. Delaynum is called while importing data.
Generating pump axis from these variables comes in later section.
delaynum=401; % Number of tau steps in a single frame
Dt=20E-15; % Tau step size
RF=1400; %Rotating frame frequency (cm^-1)

%Tw parameters

%Define Tw step sizes in picoseconds
Tw=0.15; % First Tw step Size
Twl=0; % Second Tw step size if applicable


N1=101;% Number of Tw steps for first step size
N2=0; % Number of Tw steps for second step size


%Give matlab your file name for 2DIR data pulled from LabView
Fname1=['EC_F_1501012500_ '];
Fname2=['_20_ _0X_ _0Y_ 0'];


%Parameters for importing 2D data
Fname=[Fname1,'*',Fname2]; %String matlab searches for and counts * position
files = dir(Fname); %Count number of files in current directory with given name
N=numel(files); %Create variable to track number of Tw steps


%Initialize empty arrays to be populated in loops.
DT=zeros(128,delaynum,N);  %Raw data
Aframe=zeros(64,N); % first non-phase cycled A frame
RFT=zeros(2*delaynum,64,N); %2D data
```

```
R=RFT; %Rephasing spectrum
NR=R; %Non-rephasing spectrum

%Normalized data
RFTn=R;
Rn=R;
NRn=R;

%Arrays for fourier transforming data
tpc=zeros(delaynum,64,N);
zp=RFT;
```

Import raw data

```
%Give matlab your file name
%Loop imports data for each Tw step and stacks them in a 3D array with indices
(pixel #, tau, Tw)

for i = 1:N; %looping though numberof Tw steps.
    name = [Fname1, num2str(i) Fname2]; % Create a string with your file name
    data=importdata(name); %Import data from single Tw step
    DT(:,:,i)=data; %3D array of raw data. Indices are (pixel #, tau, Tw)
    %Note: the first dimension contains 128 positions. positions 1:64 contain
phase cycled data. Positions 65:128 contain the first frame of
    % data before phase cycling.
end
```

Make axes

```
% Generate pump axis, Tw axis, and import/generate probe axis

% Make time domain axis
pta1=linspace(0,delaynum*Dt,delaynum); %Time array for FID without zero padding


%Time domain axis for zero padded data
Lt=2*delaynum; %Length in time, 1202 if there are 601 time steps (with zero
padding to double # steps)
pta=linspace(0,Lt*Dt,2*delaynum); %Time array for zero padded data

Dv=1/(Dt*Lt); %change in frequency space, delta v (Hz)
Dw=(1/(299792458/Dv))./100;  %delta w in wavenumbers
```

```
%Convert zero padded tau axis to frequency axis in cm^-1
 for k = 1:Lt; %loop through length of tau
     V(k)=Dv*((Lt/2)*(-1)+(k-1)); %Freqeuncy axis (Hz)
     V_axis(k)=(1/(299792458/(V(k))./100); %conversion to cm-1
 end

PumpAxis=round(V_axis)+RF; %adding rotating frame
```

Tw Axis

```
time1=linspace(0,(N1-1)*Tw,N1); %Tw for short time constant
time2=linspace((N1-1)*Tw,(N2-1)*Twl+(N1-1)*Tw,N2); %Tw for long time constant
time=horzcat(time1,time2); %Full Tw axis
```

Import probe axis

```
WL= importdata('Cal_64_5560_3'); %Import calibrated probe axis for a given
grating and center wavelength (nm)
WN=round(10000000./WL); %Converting axis to Wavenumbers

% WN=[1:64]; %Generic pixel axis if calibrated axis is not available
```

Process Raw Time Domain Data

```
%The following sections manipulate raw data before fourier transforming into
frequency domain. They should be
%commented out if you do not want to include additional data processing.
```

Remove FID offset

```
%Loop to subtract average value of FID from time domain data

for t=1:N
    for p=1:64
        NT(p,:,t)=DT(p,:,t)-mean(DT(p,:,t)); %subtract any offset in FID
(should integrate to near zero if there isn't an offset)
    end
end


%If this section is omitted, uncomment next line. NT is called later in the
program and needs to be given a value.
```

```
% NT=DT;
```

Include exponential window function on FID

```
%This block applies an exponential decay to the FID of each pixel in the phase
cycled data
taulim=find(pta>=7E-12,1,'first'); %Time step after which exponential window is
applied.

%Building window function
We(1:taulim-1)=1; % window = 1 for all tau<taulim
We(taulim:delaynum)=exp(-1e+12.*(pta1(taulim:delaynum)-pta(taulim))); %Apply
exponential decay for tau>taulim

%plot window function and example FID
 plot(pta1,We)
 hold on
 plot(pta1,Selfnorm(NT(41,:,1)))
 hold off
```

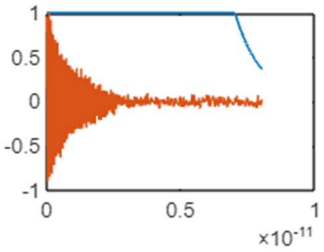


```
 for w=1:64
     NTw(w,:,:)=We.*NT(w,:,:); %Multiply window by exponential decay for each
pixel and each Tw step.
 end
 NT=NTw;
```

Fourier transform time domain data

```
for i = 1:N; %looping though number of Tw steps
    Tpc(:,:,i)=NT(1:64,:,i)'; %transpose for plotting with pump on y and 64
probe array on x. No idea why we do it this way but we do.
    % Zero Pad with number equal to tau steps (Second index in DT)
```

```
     zp(:,:,i)=padarray(Tpc(:,:,i),delaynum,0,'post'); %zeropadding data (2*
delaynum is the number of steps in tau). Adds delaynum zeros to the end of each
FID
     FT(:,:,i)=fftshift(fft(zp(:,:,i)),1); %Fourier transformm zeropadded data
     RFT(:,:,i)=real(FT(:,:,i))*-1; %real portion of the fourier transform. This
yields an absorbitive 2D IR spectrum.
 end
```

Generate rephasing and non-rephasing spectra

```
 % IFFT and imposing causality
 iDT=(ifft(NT(1:64,:,:),64,1)); %Inverse fourier transform time domain data
along probe axis. (iFFT into t3)

 for k=1:32
     iDT(k,:,:)=0; %Force all t3<0 positions to zero (can't have negative t3
data)
 end

 DTf3=(fft(iDT,64,1)); %Fourier transfrom from t3 back to probe axis

 %Repeat fourier transform over tau for DTf3
 for i = 1:N; %looping though number of Tw steps
     Tpc(:,:,i)=DTf3(1:64,:,i)'; %transpose for plotting with pump on y and 64
probe array on x.
     zp(:,:,i)=padarray(Tpc(:,:,i),delaynum,0,'post'); %zeropadding data (2*
delaynum is the number of steps in tau). Adds delaynum zeros to the end of each
FID
     FT(:,:,i)=fftshift(fft(zp(:,:,i)),1); %Fourier transform zeropadded data.
     RC(:,:,i)=(FT(:,:,i))*-1; %Change amplitude to match convention.
 end

 %Seperate rephasing and non-rephasing spectra

 NR=RC; %Non-rephasing appears at positive pump axis values. Can be treated the
same way as RFT. You can see an upside down rephasing spectrum if you look at
negative pump frequencies.

 %Rephasing spectrum needs to have its pump axis positions adjusted to remove
extra index position.
 R(delaynum+1:2*delaynum,:,:)=flip(RC(2:delaynum+1,:,:),1); %Flip rephasing
spectrum from negative pump axis values to positive.
```

Data processing in frequency domain

```
%Normalize to laser power and probe spectrum
```

Normalize to laser power

```
%Generate array of average intensity in for each pixel at each Tw step

for t=1:N
    for p=1:64
        Aframe(p,t)=mean(DT(64+p,round(delaynum/2):delaynum,t)); %mean
intesnsity of 0-0 frame tracks laser power for each tw step
    end
end


% Self normalize Tw intesnity for each pixel. We only need relative differences
for each pixel.
    for p=1:64
        Laserpower(p,:)=Selfnorm(abs(Aframe(p,:)));
    end

    plot(time,Laserpower)
```

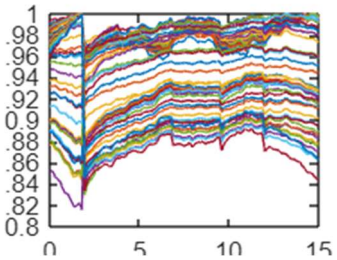


```
%Import probe spectrum
load("probe5560")
py=Selfnorm(probe5560(:,2));
py=smooth(py);
% py=ones(1,64); %uncomment if you don't want probe spectrum.



%Normalize 2D spectrum to laser power and probe spectrum.
for t=1:N
    for p=1:64
        RFTn(:,p,t)=RFT(:,p,t)./Laserpower(p,t)./py(p);
        Rn(:,p,t)=R(:,p,t)./Laserpower(p,t)./py(p);
        NRn(:,p,t)=NR(:,p,t)./Laserpower(p,t)./py(p);
    end
end
```

Save data for Calling to other scripts

```
 % Data is saved in a cell array that can be imported into other programs
 filename = ['EC_T5_Full.mat']; %Name your file
 Dataset={PumpAxis,WN,RFTn,time,NT,Rn,NRn,pta1}; %Array of variables for
analysis by trial
 save(filename, 'Dataset');  %Should give .mat file with cell array 'Dataset'
```